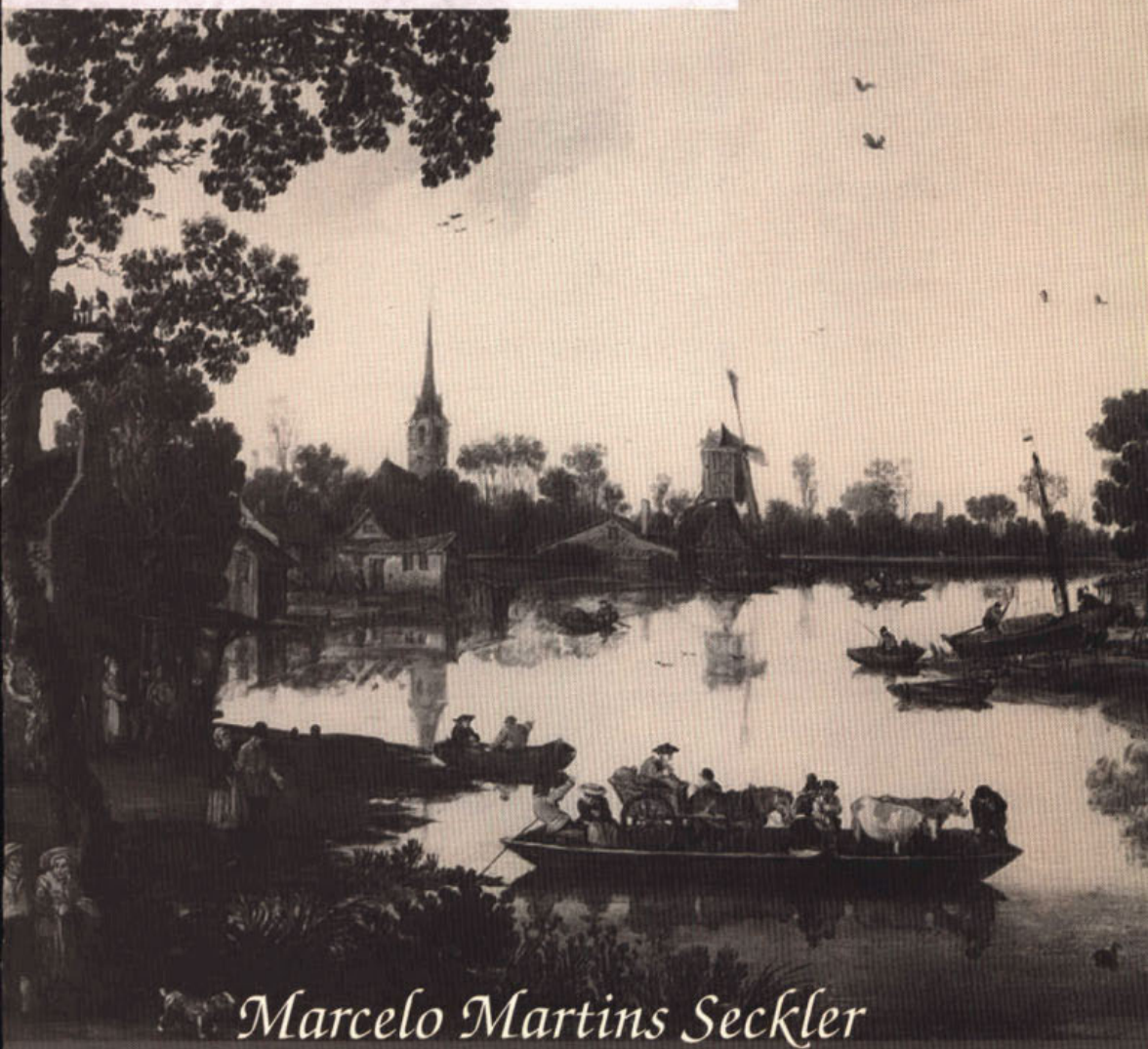


Calcium phosphate precipitation in a fluidized bed

1994-20_calcium-phosphate-precipitation



Marcelo Martins Seckler

1994

STOWA

Stichting Toegepast Onderzoek Waterbeheer
Postbus 8090

3503 RB Utrecht

tel. 030-321199

fax 030-321766

Publikaties en het publikatieoverzicht
kunt u uitsluitend bestellen bij:

Hageman Verpakkers BV

Postbus 281

2700 AC Zoetermeer

tel. 079-611188

fax 079-613927

o.v.v. ISBN- of bestelnummer en
een duidelijk afleveradres.

STELLINGEN

behorend bij het proefschrift

Calcium Phosphate Precipitation in a Fluidized Bed

M.M. Seckler

1. Een fundamenteel verschil tussen korrelreactoren voor defosfatering en ontharding ligt in het mechanisme volgens welke de vaste-stof (resp. calciumfosfaat en calciumcarbonaat) wordt afgezet op de zandkorrels: bij defosfatering speelt aggregatie de belangrijkste rol terwijl bij ontharding voornamelijk moleculaire groei plaatsvindt. van Dijk, J.C. & Wilms, D.A., *J. Water SRT* (40) 5, p.263-280, 1991 en dit proefschrift.
2. De eigenschappen van kleine, snel gevormde deeltjes worden grotendeels bepaald door de processen die zich afspelen tijdens de beginfase van het precipitatieproces. Het is gewenst om basiskennis op het gebied van fysische chemie van oppervlakken toe te passen om de kinetiek van die processen te beschrijven. Het is daarbij essentieel om methoden voor het bepalen van submicron deeltjesgrootteverdelingen bij zeer korte precipitatie-tijden te ontwikkelen.
3. Het aggregatie-breuk proces kan experimenteel van nucleatie en groei gescheiden en daardoor beter bestudeerd worden.
R. David, J. Villiermaux, P. Marchal & J.P. Klein *Chem. Eng. Sci.* (46) 4, p.1129-1136, 1991 en dit proefschrift.
4. De volume-gebaseerde geboorte- en sterffuncties ($B(v)$ en $D(v)$, $\# \cdot m^{-4}$) voor het "tweedeel gelijk-volume breukproces" zijn aan elkaar gekoppeld via $B(v) = 4 D(2v)$ en niet via de in Randolph & Larson voorgestelde vergelijking.
Randolph, A.D. & Larson, M.A. *Theory of particulate processes*, 2nd Ed., Academic Press, N.Y., page 72, eq. (3.7.1-13), 1988.

5. Het ontwikkelen van methoden om lokale deeltjesgrootteverdelingen in precipitatoren te bepalen is nodig om de interacties tussen menging en precipitatie beter te kunnen begrijpen.
6. Inductietijdmetingen bij calciumfosfaat precipitatie ($\sim 100-1000$ s) zijn reproduceerbaar en gevoelig voor de gebruikte procedure om de reactanten te mengen (< 1 s). Inductietijdmetingen kunnen dus gebruikt worden om mengprocessen te bestuderen. van Kemenade, M.J.J.M. & de Bruyn, P.L. *J. Colloid. Interf. Sci.* (118) 2, p.564-585, 1987.
7. Vaste-vloeistof grensvlakspanningen (σ) die door middel van inductietijdmetingen bepaald zijn, zijn alleen van waarde als de gebruikte definitie van de oververzadiging (β) vermeld wordt, omdat de σ^3/β^2 verhouding de direct bepaalde parameter is.
8. Als Brazilië Nederland was, lag het al onder water.
9. Regeren is vooruitziën, negeren is opzij kijken.
10. Je wordt niet gelukkiger als je weet wat je over een uur, dag, maand gaat doen.

*Calcium phosphate precipitation in a
fluidized bed*

**CALCIUM PHOSPHATE PRECIPITATION
IN A FLUIDIZED BED**

PROEFSCHRIFT

ter verkrijging van de graad van doctor aan de Technische Universiteit Delft,
op gezag van de Rector Magnificus, prof. ir. K.F. Wakker,
in het openbaar te verdedigen ten overstaan van
een commissie aangewezen door het College van Dekanen,
op maandag 17 januari 1994 te 14.00 uur

door

Marcelo Martins Seckler

geboren te Rio de Janeiro, Brazilië
chemical engineer

Universiteitsdrukkerij

Dit proefschrift is goedgekeurd door de promotor
Prof. dr. ir. G.M. van Rosmalen
en de toegevoegd promotor
Dr. ing. O.S.L. Bruinsma

When citing from this thesis the following reference should be used:

M.M. Seckler, 1994

Calcium phosphate precipitation in a fluidized bed

Ph.D. Thesis, Delft University of Technology, The Netherlands

Copyright © M.M. Seckler 1994

Laboratory for Process Equipment

Delft University of Technology

Leeghwaterstraat 44,

2628 CA, Delft, the Netherlands

Cover : Esaias van de Velde, *Het Pontveer*, 1622. Amsterdam, Rijksmuseum.

a meus pais,

a Thais

CONTENTS

CHAPTER 1

INTRODUCTION

<i>1.1 Phosphorus in the Netherlands</i>	- 13 -
<i>1.2 Wastewater treatment plants</i>	- 14 -
<i>1.3 Phosphorus in wastewater treatment plants</i>	- 15 -
<i>1.4 Phosphorus removal from wastewater</i>	- 17 -
<i>1.4.1 Technological routes</i>	- 17 -
<i>1.4.2 Current practice and perspectives in the Netherlands</i>	- 23 -
<i>1.5 Calcium phosphate precipitation in a fluidized bed</i>	- 23 -
<i>1.5.1 Description of the fluidized bed</i>	- 23 -
<i>1.5.2 Process configurations: water line versus sludge line</i>	- 24 -
<i>1.5.3 Technological bottle-necks</i>	- 25 -
<i>1.6 Objectives</i>	- 26 -
<i>1.7 Scope</i>	- 26 -
<i>References</i>	- 27 -

CHAPTER 2

CALCIUM PHOSPHATE PRECIPITATION IN A FLUIDIZED BED

IN RELATION TO PROCESS CONDITIONS: A BLACK BOX APPROACH

<i>Abstract</i>	- 31 -
<i>2.1 Introduction</i>	- 31 -
<i>2.2 Process description</i>	- 32 -
<i>2.3 Experimental procedure</i>	- 35 -
<i>2.4 Process characterization</i>	- 38 -
<i>2.4.1 Brief review on calcium phosphate modifications</i>	- 38 -
<i>2.4.2 Calcium phosphate precipitation in a fluidized bed</i>	- 40 -
<i>2.4.3 Characterization of the grains and fines</i>	- 40 -
<i>2.4.4 Conversion</i>	- 46 -
<i>2.4.5 Phosphate removal efficiency</i>	- 50 -

<i>2.5 Conclusions</i>	- 52 -
<i>2.6 Appendix: Mathematical model for the chemical equilibrium for the system Ca-PO₄-OH</i>	- 53 -
<i>List of symbols</i>	- 56 -
<i>References</i>	- 57 -

CHAPTER 3

IDENTIFICATION OF PHYSICAL PROCESSES IN A FLUIDIZED BED FOR PHOSPHATE REMOVAL

<i>Abstract</i>	- 61 -
<i>3.1 Introduction</i>	- 61 -
<i>3.2 Process description</i>	- 62 -
<i>3.3 Experimental procedure</i>	- 63 -
<i>3.4 Results</i>	- 65 -
<i>3.5 Discussion</i>	- 67 -
<i>3.5.1 Primary nucleation and molecular growth</i>	- 67 -
<i>3.5.2 Aggregation</i>	- 68 -
<i>3.5.3 Abrasion</i>	- 69 -
<i>3.6 Conclusions</i>	- 69 -
<i>References</i>	- 70 -

CHAPTER 4

KINETICS OF NUCLEATION, AGGREGATION AND BREAKAGE OF CALCIUM PHOSPHATE

<i>Abstract</i>	- 71 -
<i>4.1 Introduction</i>	- 71 -
<i>4.2 Mathematical model for aggregation and breakage in a plug flow reactor (PFR)</i>	- 72 -
<i>4.2.1 Population balance</i>	- 72 -
<i>4.2.2 Aggregation</i>	- 74 -

4.2.3 Breakage	- 75 -
4.2.4 Model summary	- 76 -
4.3 Experimental	- 77 -
4.3.1 Batch experiments	- 77 -
4.3.2 Continuous experiments	- 78 -
4.4 Definitions and preliminary calculations	- 80 -
4.4.1 Precipitation time	- 80 -
4.4.2 Supersaturation	- 81 -
4.4.3 Types of particles	- 82 -
4.4.4 Growth rate and average particle size	- 82 -
4.4.5 Conversion	- 82 -
4.4.6 Moments of the PSD	- 83 -
4.4.7 Energy dissipation rate	- 83 -
4.5 Results and discussion	- 84 -
4.5.1 Batch experiments	- 84 -
4.5.2 Continuous experiments	- 87 -
4.6 Implications for a fluidized bed for phosphate removal	- 96 -
4.7 Conclusions	- 98 -
List of symbols	- 99 -
References	- 100 -

CHAPTER 5

AXIAL DISTRIBUTION OF PARTICLES IN A FLUIDIZED BED FOR PHOSPHATE REMOVAL

Abstract	- 103 -
5.1 Introduction	- 103 -
5.2 Theory	- 105 -
5.2.1 Definitions and terminology	- 105 -
5.2.2 Fluidization of monocomponent suspensions	- 106 -
5.2.3 Fluidization of multicomponent suspensions	- 107 -
5.2.4 Mathematical model for the axial distribution of particles in a	

<i>fluidized bed for phosphate removal</i>	- 108 -
5.3 Experimental	- 112 -
5.3.1 <i>Equipment</i>	- 113 -
5.3.2 <i>Experimental procedure</i>	- 114 -
5.4 Results and discussion	- 116 -
5.4.1 <i>Accuracy of the predicted voidage</i>	- 116 -
5.4.2 <i>Fluidization of sand grains</i>	- 117 -
5.4.3 <i>Fluidization of sand grains covered with a phosphate shell: sand with a wide particle size distribution</i>	- 119 -
5.4.4 <i>Fluidization of sand grains covered with a phosphate shell: sand with a narrow particle size distribution.</i>	- 120 -
5.4.5 <i>Implications for a fluidized bed for phosphate removal</i>	- 121 -
5.5 Conclusions	- 126 -
<i>List of symbols</i>	- 128 -
<i>References</i>	- 128 -

CHAPTER 6

INFLUENCE OF HYDRODYNAMICS ON PRECIPITATION

<i>Abstract</i>	- 131 -
6.1 Introduction	- 131 -
6.2 Mathematical model	- 132 -
6.2.1 <i>General model description</i>	- 132 -
6.2.2 <i>Assumptions</i>	- 133 -
6.2.3 <i>Conservation of mass and momentum</i>	- 134 -
6.2.4 <i>Conservation of chemical species in solution</i>	- 135 -
6.2.5 <i>Moments of the particle size distribution</i>	- 136 -
6.2.6 <i>Precipitation kinetics</i>	- 138 -
6.3 Simulation conditions	- 140 -
6.4 Simulation results and discussion	- 141 -
6.4.1 <i>Introduction</i>	- 141 -
6.4.2 <i>Local properties</i>	- 142 -

6.4.3 Utilization of the reactor space	- 148 -
6.4.4 Conversion, product size and coefficient of variation.	- 150 -
6.5 Conclusions	- 152 -
List of symbols	- 154 -
References	- 155 -

CHAPTER 7

OPTIMIZATION OF THE PHOSPHATE REMOVAL EFFICIENCY DURING CALCIUM PHOSPHATE PRECIPITATION IN A FLUIDIZED BED

Abstract	- 157 -
7.1 Introduction	- 157 -
7.2 Model description	- 158 -
7.3 Experimental	- 162 -
7.3.1 Fluidized bed preceded by a pre-mixing reactor	- 162 -
7.3.2 Fluidized bed with a spread in base dosage	- 164 -
7.4 Results and discussion	- 165 -
7.4.1 Definition of terms and preliminary calculations	- 165 -
7.4.2 Fluidized bed preceded by a pre-mixing reactor	- 167 -
7.4.3 Fluidized bed with base dosage at the bottom	- 168 -
7.4.4 Fluidized bed with a spread in base dosage	- 170 -
7.5 Conclusions	- 172 -
List of symbols	- 174 -
References	- 174 -

SUMMARY

SAMENVATTING

ACKNOWLEDGEMENTS

CURRICULUM VITAE

CHAPTER 1

INTRODUCTION

This thesis is mainly concerned with a method for phosphorus removal from wastewater based on the precipitation of a mineral phosphate salt in a fluidized bed. In the first part of this introduction the importance of phosphorus removal from wastewater and its relation to eutrophication is described. Phosphorus removal units are added to existing wastewater treatment plants, so these installations and their phosphorus streams are described next. Thereafter, various technologies for phosphorus removal are presented, with special attention to the fluidized bed method. The bottle-necks of the fluidized bed technology are then highlighted, since they gave the motivation for this research. Finally the objectives and scope of the thesis are presented.

1.1 Phosphorus in the Netherlands

Eutrophication is commonly known as the state of a waterbody which is manifested by an intense proliferation of algae and higher aquatic plants and their accumulation in excessive quantities [22]. Eutrophication can cause the water quality and the biological populations in the water to change in a detrimental way, interfering with man's use of the water resource.

Eutrophication can be most efficiently fought by reducing the input of aquatic plant nutrients, mainly nitrogen and phosphorus, to surface waters. The main point sources of nutrients are municipal and industrial sewage. Diffuse nutrient sources are surface runoff from urban and agricultural areas, atmospheric precipitation as well as regeneration of sediments.

The contribution of the different sources of phosphorus to the total input to surface waters in the Netherlands can be visualized from the phosphorus balance shown in Table I [19]. There is an annual accumulation of $17.8 \cdot 10^6$ kg P. In order to reverse this picture, policies to reduce the phosphorus input from several sources have been implemented. Such policies have led to a drastic reduction in the use of phosphorus-containing fabric detergents. An extra reduction of 50% in the phosphorus emissions to the Rhine river for the period 1985-1995 was agreed by the countries through which the Rhine flows and those around the North Sea

[10,17]. Consequently, Dutch legislation requires that wastewater treatment plants will be removing 75% of their phosphorus load from 1995 on [16,18]. But even these measures may not be sufficient to reduce eutrophication to acceptable levels, so it is likely that stricter policies will be adopted in the future.

Table I. Phosphorus balance for surface waters in the Netherlands in 1990. Source [19].

⁽¹⁾ This emission takes place near the coast and does not contribute to the eutrophication of surface waters.

	Input kg P·10 ⁶		Output kg P·10 ⁶
domestic wastewater	4.3	output to sea	
industrial wastewater		indl. waste	13.5 ⁽¹⁾
close to sea	13.5 ⁽¹⁾	other	9.4
other	2.4	dredged material	4.9
rivers crossing borders	20.2	other	0.3
run-off (agriculture)	4.5		
other	1.0		
		<i>Accumulation</i>	17.8
Total	45.9		45.9

1.2 Wastewater treatment plants

Conventional treatment of domestic wastewater [6,7,24] usually consists of the so-called primary and secondary treatment, as illustrated in Figure 1. In the primary treatment a portion of the suspended solid and organic matter is removed from the wastewater through physical unit operations such as screening and sedimentation. Secondary treatment is directed mainly towards the removal of organic material and additional suspended solids through a combination of physical unit operations (e.g. sedimentation) and biological processes (e.g. activated sludge and the fixed-media filter processes). Microorganisms convert organic material in the water into gases that can escape to the atmosphere or into biological cell tissue that can be removed by sedimentation. Part of the biological solids are recycled, part removed. The biological solids from the primary as well as from the secondary treatment are further treated for reuse, disposal or incineration. The purified water may be disinfected with

chlorine prior to discharge to a receiving watercourse.

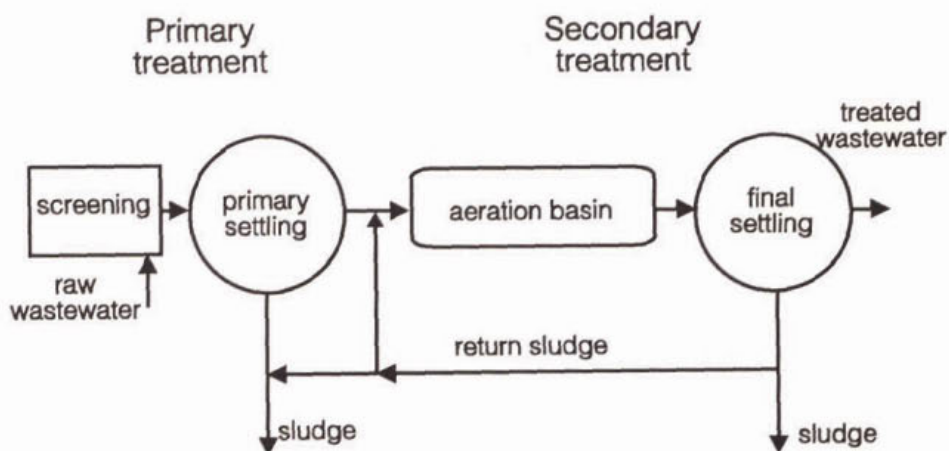


Figure 1. Flow diagram of a conventional wastewater treatment plant with primary and secondary treatment.

Tertiary treatment is applied when a more efficient removal of water constituents is required than is possible with conventional secondary treatment. The constituents to be removed may be nutrients (nitrogen, phosphorus), toxic compounds, organic material and suspended solids. Tertiary treatment methods for phosphorus removal will be discussed in section 1.4.

Small wastewater flows are often processed, without primary treatment, in completely mixed aeration basins followed by sedimentation (Figure 2).

Industrial wastewater is often treated by the same methods as domestic wastewater. Sometimes the domestic and industrial wastes are treated together in a single municipal treatment plant. In the Netherlands this is often the case for the food industry (specially dairy and potato processing) and for the manure processing industry.

1.3 Phosphorus in wastewater treatment plants

The input of phosphorus to municipal wastewater treatment plants in the Netherlands decreased 30 % (from 55.000 to 38.500 kg P per day) from 1986 to 1991 [2], as a result of

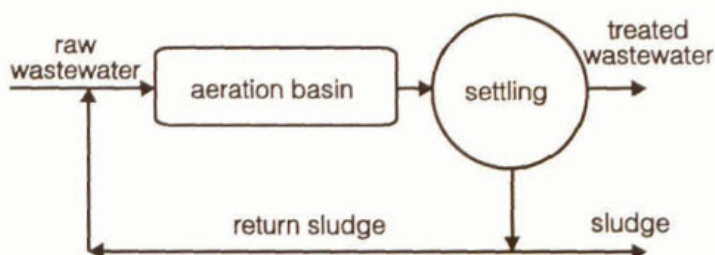


Figure 2. Flow diagram of a wastewater treatment plant for small flows: biological processing without primary treatment.

a drastic reduction in phosphorus-containing fabric detergents. In 1991 the average phosphorus concentration in raw domestic wastewater in this country was $8.9 \text{ mg P}\cdot\text{l}^{-1}$ [2]. In areas where industrial wastewater contributes to the total flow in municipal wastewater treatment plants, phosphorus concentrations within the range of 15 to $30 \text{ mg P}\cdot\text{l}^{-1}$ were encountered. Industrial wastes contribute with 25% of the total chemical oxygen demand in municipal wastewater treatment plants in the Netherlands [2] (no data are available on the corresponding phosphorus contribution).

About 10 to 30% of the phosphorus entering the treatment plant are removed naturally as part of the conventional biological step, even if no special measures for phosphorus removal are taken [1]. The averaged phosphorus removal in the Netherlands in 1991 was 59% [2], mainly due to the phosphorus removal already practiced, so that the average phosphorus concentration of the treated wastewater may be estimated to be $3.5 \text{ mg P}\cdot\text{l}^{-1}$. In areas where no phosphate removal measure is currently applied as well as in areas affected by industrial emissions, the phosphate concentration in the treated wastewater may be estimated to assume the values of 7 and $18 \text{ mg P}\cdot\text{l}^{-1}$, respectively.

In order to obtain a removal of 75% in the phosphorus load to surface waters, the present legislation in the Netherlands [18] establishes that before the year 1995 the phosphorus content in the effluent of wastewater treatment plants will be limited to $1 \text{ mg P}\cdot\text{l}^{-1}$ for installations with a capacity higher than 100.000 population equivalents, or to $2 \text{ mg P}\cdot\text{l}^{-1}$ for

those with a capacity between 100.000 and 20.000 p.e.¹. For installations with a capacity lower than 20.000 p.e., higher concentrations will be allowed, provided that 75% of the phosphorus load in the administrative region is removed. Since the current effluent concentrations are higher than the required values, additional phosphorus removal units will have to be implemented in wastewater treatment plants. The phosphorus removal method to be used largely depends on the raw water phosphorus concentration as well as on the required effluent concentration.

1.4 Phosphorus removal from wastewater

A number of processes have been developed to remove phosphorus from sewage and other effluents. In recent years special attention has been paid to methods that lead to the recovery of phosphorus in a concentrated form, suitable for re-use, contrary to methods that produce phosphorus-containing sludges, since handling and disposal of sludge in densely populated areas are becoming increasingly expensive. Besides, re-usable phosphorus implies a reduction in the total phosphorus input to the environment. Other developments aim at more efficient phosphorus removal to respond to expected stricter legislation in coming years.

The most important methods for phosphorus removal from conventional wastewater treatment plants are discussed next in terms of characteristics such as the form of the recovered phosphorus (as a sludge, concentrated solid, etc.), the degree of phosphorus removal, the sensitivity to water characteristics, etc.. The current phosphorus removal practice in the Netherlands as well as the future perspectives are also discussed.

1.4.1 Technological routes

Biological methods [1] are based on the so-called 'luxury uptake' of phosphorus by certain facultative microorganisms. Such uptake is stimulated by subjecting the microorganisms first

¹ the P concentrations mentioned should be determined from the progressive average over 10 daily samples taken consecutively. The P values determined in this way are generally 1 to 2.5 times higher than the yearly average. Therefore the limit adopted in the legislation is stricter than a limit based on the yearly average.

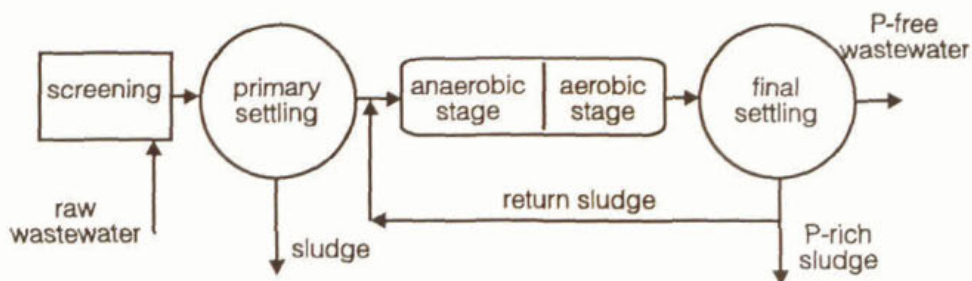


Figure 3. Flow diagram of the biological method for phosphate removal.

to anaerobic conditions, where they release phosphate to the liquid phase, and next to an aerobic environment, where phosphorus uptake occurs. The process diagram is sketched in Figure 3. The first section of the aeration basin is made anaerobic by simply shutting off the aerators. Multiple aerobic-anaerobic mixing periods are used when simultaneous nitrogen and phosphorus removal is required. The phosphorus incorporated into the cell mass is removed in the secondary clarifier. No additional sludge is produced in these processes compared to conventional activated sludge systems, but care must be taken to avoid phosphorus dissolution and return to the system during the sludge handling. Implementation of this method only requires minor changes in existing activated sludge plants. The method has been developed to full scale. The phosphorus concentration in the treated wastewater depends on the wastewater characteristics (mainly the ratio between the biological oxygen demand and the phosphorus concentration), but in general varies within the range of 1 to 2 mg P·l⁻¹. For low phosphorus concentrations in the raw wastewater, a higher phosphorus removal efficiency is expected [11].

Chemical addition methods [1] are based on the precipitation of sparingly soluble phosphates, achieved by the addition of aluminum salts, iron salts or lime to the wastewater. The chemicals may be added prior to the primary treatment in a conventional sewage treatment plant, at the secondary treatment or as an independent tertiary treatment. Separation of the phosphorus from the wastewater occurs respectively in the primary settler, secondary settler, or in an additional filtration step. Phosphorus is thus separated from the wastewater either incorporated in the biological sludge or as a separate phosphate slurry. The amount of chemicals needed to reach a given phosphorus concentration in the treated water is directly

related to the stoichiometry of the precipitation reaction. Therefore, the consumption of chemicals is proportional to the concentration of phosphorus in the raw water, making these methods attractive for wastewaters with low phosphorus concentration levels. Implementation of this method requires hardly any changes in existing sewage treatment plants, except in the case of chemical addition as a tertiary treatment. The process has been applied on an industrial scale in many countries for several years. The phosphorus concentration of the treated water is about $1 \text{ mg P} \cdot \text{l}^{-1}$ [1,3]. Chemical addition in two steps, at the secondary treatment and downstream of it, leads to effluents with a concentration of about $0.5 \text{ mg P} \cdot \text{l}^{-1}$ [20].

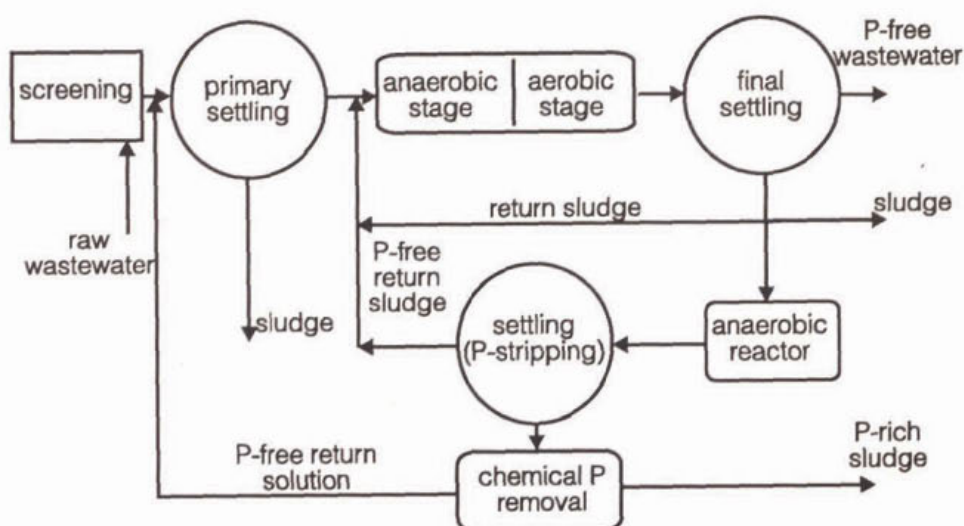


Figure 4. Flow diagram of a method for phosphate removal that combines a biological and a chemical addition step, also called biological phosphate removal in the sludge line.

Methods for phosphorus removal that combine biological and chemical addition steps [1,21] are schematically shown in Figure 4. These methods are also known as *biological phosphorus removal in the sludge line*. Part of the returned activated sludge is subjected to anaerobic conditions, leading to phosphorus release. This sludge is separated from the phosphorus rich liquid phase and returned to the secondary treatment, where 'luxury uptake' of phosphorus takes place. The phosphorus rich liquid phase is treated by addition of lime or by other technologies for phosphorus removal (presented below). Since this stream

represents only 20 to 30% of the total plant flow, its treatment is economically feasible. The method has been developed to full scale. This process, unlike other biological methods, is not sensitive to the wastewater composition (biological oxygen demand to phosphorus concentration ratio) and leads to effluent phosphorus concentrations of about $1 \text{ mg P}\cdot\text{l}^{-1}$.

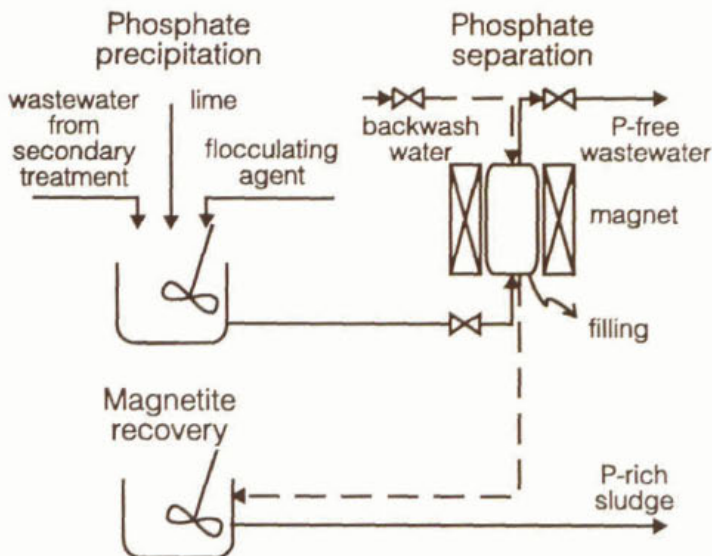


Figure 5. Flow diagram of the magnetic method for phosphate removal.

A simplified flowsheet of the *magnetic method* for phosphorus removal [27,28] is shown in Figure 5. The water to be treated is first conducted to a reactor where calcium phosphate is allowed to precipitate by chemical addition of lime or an iron salt. Magnetic grains (magnetite) and a flocculating agent are then added in the same equipment to promote the attachment of the phosphate precipitate to the magnetic grains. The suspension is then passed through a batchwise operated magnet where the phosphorus containing magnetic grains are captured. These grains are removed intermittently by backwashing and are fed to a vessel where, under intense mixing and ultrasonic treatment, the magnetite is separated from the phosphate precipitate and recycled. The phosphorus is recovered as a slurry which can be reused in the agriculture or as a raw material for the fertilizer industry. The method has been developed to full scale. The treated water contains about $0.5 \text{ mg P}\cdot\text{l}^{-1}$. The method can be applied either in combination with the biological process in the sludge line or as a quaternary

treatment. In the latter case, effluent concentrations of about $0.1 \text{ mg P}\cdot\text{l}^{-1}$ are obtained.

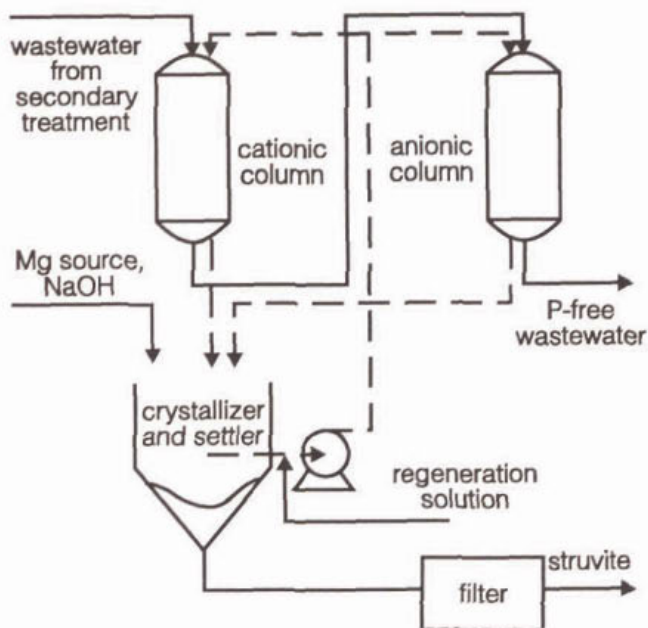


Figure 6. Flow diagram of the ion exchange method for phosphate removal.

An *ion exchange* method has been developed in Italy [15] which is based on the selective behavior of certain cationic and anionic resins that favor the removal of respectively NH_4^+ and HPO_4^{2-} ions from wastewater. A flowsheet of the process is shown in Figure 6. Both resins are regenerated with a neutral 0.6 M NaCl solution. The regeneration eluates from both resins are mixed and a magnesium salt is added so that an ammonium magnesium phosphate salt (struvite, $\text{NH}_4\text{MgPO}_4\cdot 6\text{H}_2\text{O}$) precipitates. The precipitate is separated from the water by sedimentation and the supernatant solution is reused for the following regeneration cycle. The method has been applied on the effluent of a pilot scale secondary wastewater treatment and led to a reduction in the phosphorus concentration from 4.0 to about $0.5 \text{ mg P}\cdot\text{l}^{-1}$. Phosphorus is removed as struvite crystals with potential value as ammonium-magnesium-phosphate containing fertilizers.

A method based on the *crystallization of hydroxyapatite in fixed beds* has been developed in Japan [8,12]. A flow diagram of the process is shown in Figure 7. The effluent of the

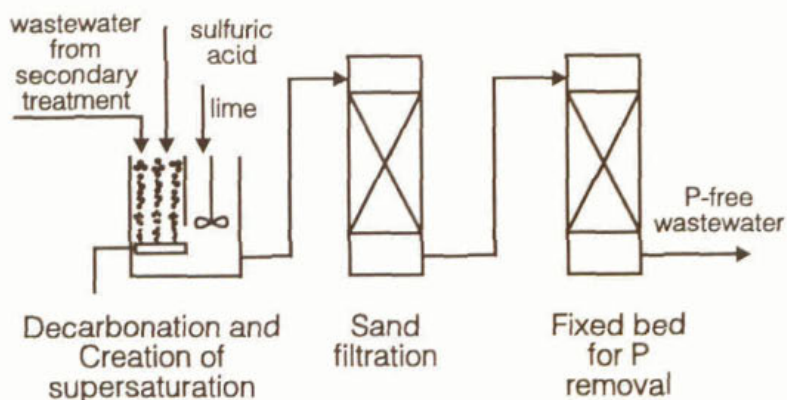


Figure 7. Flow diagram of the fixed bed process for phosphate removal.

secondary wastewater treatment is mixed with a base and eventually with a calcium source to create a supersaturated solution. Process conditions are chosen so that spontaneous precipitation of calcium phosphate is minimized. The supersaturated solution then passes through a fixed bed containing large apatite grains. Phosphorus removal is claimed to take place mainly by crystal growth on the apatite grains. A decarbonation unit is placed upstream the fixed bed to minimize calcium carbonate co-crystallization. A sand filter is also used to remove the spontaneously formed calcium phosphate. A process variant using magnesia clinker as the substrate for hydroxyapatite growth has been developed, which makes the process less sensitive to the water bicarbonate alkalinity [13]. In both process variants the outgrown grains may be used as a raw material for the fertilizer industry. The method has been applied on an industrial scale for wastewaters with phosphorus concentrations within the range of 1 to 3 mg P·l⁻¹ to reduce their concentration to about 0.1 mg P·l⁻¹.

A method based on *calcium phosphate precipitation in a fluidized bed* [9,23,25,26] leads to the recovery of phosphorus as calcium phosphate covered grains of 1 mm in diameter containing 7 wt % P. The single step phosphate removal efficiency is about 50%. Introduction of recirculation increases the efficiency to about 80%. Therefore, the phosphate content of the effluent depends on the inlet concentration. The method was applied on a full scale plant and led to effluent phosphorus concentrations of about 0.5 mg P·l⁻¹ by placing a filter downstream the process [23]. This method is the main subject of this thesis, so it will be described in more detail in section 1.5.

1.4.2 Current practice and perspectives in the Netherlands

In the Netherlands, the yearly costs (investment and operating costs) for phosphorus removal were 10 million american dollars in 1991. A progressive increase of these costs up to 100 million in 1995 is expected [4]. The most commonly used techniques are chemical addition and biological phosphorus removal in the water line. Research on the biological phosphorus removal in the sludge line, on the magnetic method as well as on the fluidized bed method has been done and is still in progress at universities, engineering companies and wastewater treatment associations. The main motivation for this research has been the possibility offered by these methods of recovering phosphorus in a re-usable form. Laboratory and pilot scale research with wastewater from several places in the Netherlands have been conducted during the last 10 years, and have already led to the implementation of a few industrial scale

installations. The fluidized bed method was applied in three locations, one with start-up in 1989 and two others in 1993. The latter two were combined with the biological phosphorus removal in the sludge line. Two large scale plants for phosphorus removal by the magnetic method were started up in 1991.

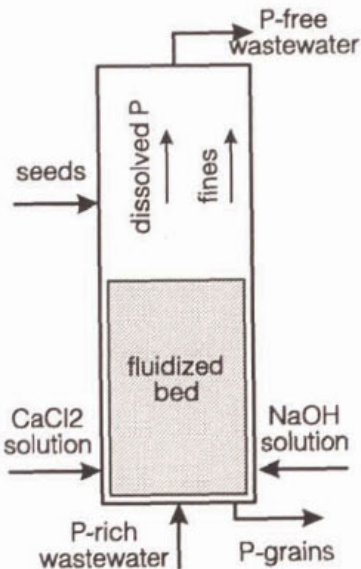


Figure 8. Schematic representation of a fluidized bed for phosphate removal.

1.5 Calcium phosphate precipitation in a fluidized bed

1.5.1 Description of the fluidized bed

The process is based on the precipitation of calcium phosphate upon seed grains in a fluidized bed (Figure 8). Precipitation is induced by the addition of a base to the water to bring the pH up to 8 - 9 and, for soft waters, by the addition of a calcium source.

The phosphate covered grains are removed from the bottom of the bed and replaced intermittently by fresh seed grains. The calcium phosphate which is not recovered leaves the bed at the top mainly as fine particles. A decarbonation unit is often placed upstream the

fluidized bed to avoid detrimental calcium carbonate co-crystallization. A recirculation stream is applied to increase the overall phosphorus removal efficiency. Economical considerations lead in practice to recirculation factors that allow for efficiencies around 80%. If higher efficiencies are required, a filtration step must be added downstream the reactor. Phosphorus is removed in the form of phosphate-covered sand grains of about 1 mm in diameter that can be reused as a raw material for the fertilizer industry.

1.5.2 Process configurations: water line versus sludge line

The base consumption in the fluidized bed process - an important component in the

process costs - is not very much sensitive to the phosphorus content in the raw wastewater. This makes this process attractive for wastewaters with a high phosphorus concentration. For concentrations lower than approximately $13 \text{ mg P} \cdot \text{l}^{-1}$ other methods such as chemical addition of aluminium or iron salts, with costs proportional to the phosphorus concentration, become more attractive. When considering the wastewaters normally found in the Netherlands, two configurations for the fluidized bed method are possible: in the 'water line' (Figure 9) or in the 'sludge line' (Figure 10).

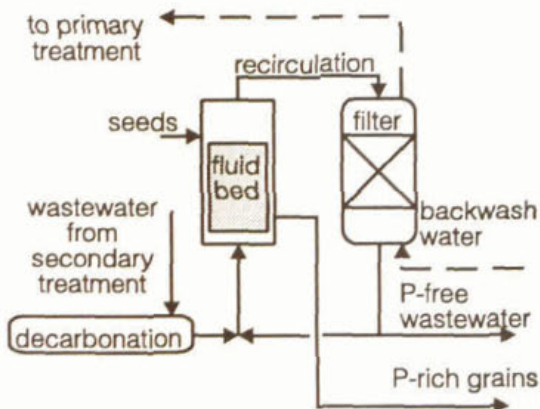


Figure 9. Phosphorus removal with a fluidized bed in the water line.

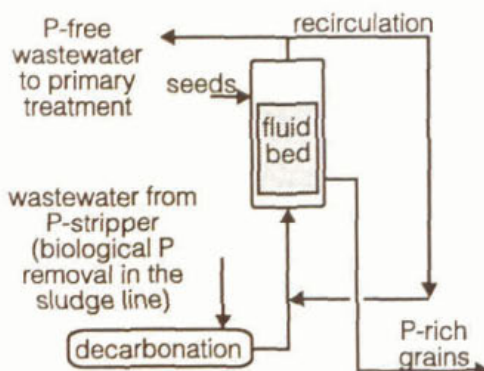


Figure 10. Phosphorus removal with a fluidized bed in the sludge line.

The fluidized bed in the 'water line', i.e. as a tertiary treatment, may be applied in areas where industrial emissions are important and high raw water concentrations are encountered. A filtration step is added to give an effluent concentration of $0.5 \text{ mg P}\cdot\text{l}^{-1}$ [23]. The backwashed water from the filter is recycled to the primary treatment, where the phosphate particles redissolve and reach the fluid bed again.

Combination of the fluidized bed with the biological method for phosphorus removal in the 'sludge line' can be applied for most Dutch domestic wastewaters, which concentrations are typically $7 \text{ mg P}\cdot\text{l}^{-1}$. Phosphorus is separated biologically from the wastewater, generating a small stream with a high phosphorus concentration of 20 to $100 \text{ mg P}\cdot\text{l}^{-1}$. This stream is treated in the fluidized bed. The effluent of the fluidized bed, which is depleted of phosphorus, is recirculated to the primary treatment. The flow treated in the fluidized bed is only 20 to 30% of the total raw wastewater flow, so the fluidized bed is considerably smaller than if it would be applied in the 'water line'. Since the liquid effluent of the fluidized bed is returned to the process, its phosphorus concentration is not bound to values fixed by legislation, so filtration is in principle not needed. However, the phosphorus removal efficiency in the fluidized bed still determines the phosphorus concentration level in the biological step and thus affects the overall system efficiency.

1.5.3 Technological bottle-necks

The main technological bottle-neck of the fluidized bed process is the low phosphorus removal efficiency, which makes it necessary to apply large recirculation rates to achieve acceptable overall efficiencies. As explained in section 1.5.1, the loss in efficiency is caused mainly by the development of fine calcium phosphate particles that leave the reactor with the liquid effluent. The elementary processes involved in their formation (primary nucleation, grains abrasion, etc.) as well as the interaction between fine particles with the grains in the fluidized bed (aggregation) were not known at the start of this study. Without this knowledge no further optimization of the phosphate removal efficiency could be achieved.

Besides, some impurities turned out to have a detrimental effect on the precipitation of calcium phosphate in the fluidized bed. Carbonate ions tend to co-crystallize as calcium

carbonate upon the grains. Such co-crystallization has been found to be associated with a reduction in the phosphorus removal efficiency [23]. Magnesium ions at low concentrations are also known to affect the precipitation of calcium phosphate [5,14]. Besides, some wastewaters even contain such a high level of magnesium ions that the precipitation of a magnesium salt instead of a calcium salt occurs. The ranges of liquid phase composition where these effects take place, the mechanisms involved (co-crystallization, isomorphic substitution, etc.) as well as the conditions for efficient phosphate removal for the precipitation of magnesium phosphate were also unknown.

Finally, when this research started, the fluidized bed process had been extensively studied merely for applications in the water line, at phosphorus concentrations in the raw wastewater within the range of 5 to 20 mg P·l⁻¹. The behavior of the fluidized bed process in the sludge line, with phosphorus concentrations within the range of 25 - 75 mg P·l⁻¹, concerning features such as phosphorus removal efficiency, mechanical stability of the phosphate grains, reactant consumption and sensitivity of the process to the presence of impurities had not yet been established.

1.6 Objectives

The objectives of this thesis are: (i) to gain insight into the fundamental processes occurring in a fluidized bed for phosphorus removal from wastewater; (ii) to optimize the phosphorus removal efficiency and (iii) to find ways of minimizing the detrimental effect of impurities normally present in wastewaters.

1.7 Scope

In *Chapter 2* a first screening study was done on the behavior of the fluidized bed process with high inlet phosphorus concentrations. The effect of magnesium and carbonate ions normally encountered in the water, which can interfere with the process, were studied as well. For waters containing a high magnesium ion concentration, the feasibility of a process where magnesium phosphate precipitates instead of calcium phosphate was tested. A model to predict the chemical equilibrium in the liquid phase was developed. Based on both

theoretical and experimental results, a method was presented which allowed the selection of process conditions where co-precipitation of unwanted phases can be avoided. In *Chapter 3* the main processes concerning the precipitation of calcium phosphate in a fluidized bed were identified and their time-scales were established. Some of these processes were further studied in succeeding chapters. In *Chapter 4* the fluidization characteristics of the grains, in particular the axial distribution of the grains according to their density and size, were studied. *Chapter 5* was devoted to the precipitation of calcium phosphate from clear solutions. The kinetics of nucleation, aggregation and breakage of amorphous calcium phosphate were estimated. Aggregation was found to be of paramount importance during calcium phosphate precipitation. In *Chapter 6* the influence of hydrodynamics on precipitation processes from solution was examined. A mathematical model which takes into account local mixing characteristics was developed. In *Chapter 7* the aggregation of calcium phosphate primary particles was further studied in the presence of the grains in a fluidized bed. Aggregation of primary particles with the grains in the bed was found to account for 60% of the phosphate removed by the fluidized bed. Therefore, experiments were performed to stimulate this process so as to optimize the phosphorus removal in the fluidized bed. An improvement of the phosphorus removal efficiency was obtained at low turbulence levels in the fluidized bed as well as by spreading the supersaturation more evenly throughout the bed. A simple model for the fluidized bed was developed which explained the experimental findings.

References

1. Bowker, R.P.G. and Stensel, H.D., *Phosphorus removal from wastewater*, Noyes Data Corp., New Jersey, 1990.
2. Centraal Bureau voor de Statistiek, Waterkwaliteits beheer, deel b, *Zuivering van afvalwater 1991*, cbs-publikaties, The Hague, 1993 (summary in English).
3. de Jong, P. and van Starkenburg, W., Defosfateren van huishoudelijk afvalwater, *H₂O* **22**(4), p.122-123, 1989.
4. de Vries, P.J.R. and Swaager-van den Berg, J.L., Fosfaatverwijdering uit afvalwater verder toegenomen, *Waterschapsbelangen* **76**(14), p.544-550, 1991.
5. Fergusson, J.F. et. al., Calcium phosphate precipitation at slightly alkaline pH values, *J.W.P.C.F.* **45** (4), p.621-631, 1973

6. Fresenius, W., Schneider, W., Bohnke, B. and Poppinghaus, *Waste water technology*, Springer-Verlag, Berlin, 1989
7. Hammer, M.J., *Water and wastewater technology*, John Wiley & Sons, New York, 1986.
8. Hirasawa, I. and Toya Y., Fluidized bed process for phosphate removal by calcium phosphate crystallization, *ACS Symp. Series* **438**, p.355-363, 1990.
9. Hirasawa, I. et al., Phosphorous removal process from wastewater by contact crystallization of calcium apatite, *Proc. Third Pacific Chem. Eng. Congr.*, Seoul, Korea, Volume IV, p. 259-264, 1983.
10. Internationale Commissie ter Bescherming van de Rijn tegen Verontreiniging, *Actieprogramma Rijn*, 1987.
11. Janssen, P.M.J. et al., Drastische fosfaatverlaging in afvalwater en de gevolgen voor biologische defosfatering, *H₂O* **23**(1), p.6-8, 1990
12. Joko, I., Sawada, S., Goto, C. and Toyokura, K., Phosphorus removal from wastewater by crystallization method: preparation and performance of artificial seed materials, *Industrial Crystallization* **84**, Jančić, S.J. and de Jong, E.J., Eds., Elsevier Sci. Pub., Amsterdam, p.431-434, 1984.
13. Kaneko, S. and Nakajima, K., Phosphorus removal by crystallization using a granular activated magnesia clinker, *Journal W.P.C.P.* **60**(7), p.1239-1244, 1988.
14. Kibalczyk et. al. The effect of magnesium ions on the precipitation of calcium phosphates, *J. Cryst. Growth* **106** (2-3), p.355-366, 1990
15. Liberti, L. et al., Field demonstrations of the rim-nut process for nutrients recovery from municipal wastewater, *Nucl. and Chem. Waste Management*, **8**, p.83-86, 1988.
16. Ministerie van Verkeer en Waterstaat, Derde Nota Waterhuishouding, *Water voor nu en later*, Tweede Kamer, 1988-1989, 21 250, nrs. 1 en 2.
17. Ministerie van Verkeer en Waterstaat, Noordzee Actieplan, Nationaal Uitvoeringsdocument Derde Noordzeeministersconferentie, *Tweede Kamer*, 1990-1991, 21 884, nrs.1 en 2.
18. Ministerie van Vrom, VW, Wet verontreiniging oppervlaktewateren. Ontwerp-besluit inzake grenswaarden fosfaat rioolwaterzuiveringsinrichtingen te lozen afvalwater, *Staatscourant* **143**, 26 july 1989.
19. Olsthoorn, C.S.M., Stikstof en fosfor in Nederland, 1990, *Kwartaalbericht Milieustatistiek* **10**(1), p.19-27, 1993.

20. Pelloni, L., Removal of residual phosphorus and suspended solids by contact filtration, *Prog. Wat. Tech.* **10**(5/6), p.255-271, 1978.
21. Rensink, J.H., High biological nutrient removal from domestic wastewater in combination with phosphorus recycling, *Wat. Sci. Tech.* **23**, p.651-, 1991.
22. Ryding, S.O. and Rast, W., *The control of eutrophication of lakes and reservoirs, Man and the biosphere series*, Volume I, U.N.E.S.C.O., Paris and The Parthenon Pub. Group, Carnforth, U.K., 1989.
23. Seckler, M.M. et. al., Phosphate removal by means of a full scale pellet reactor, *11th Int. Symp. Ind. Cryst.*, 18-20 Sept, Garmisch-Partenkirchen, Germany, 1990.
24. Tchobanoglous, G. and Burton, F.L., *Wastewater engineering: treatment, disposal and reuse*, McGraw-Hill Pub. Co., New York, 1991.
25. van Dijk, J.C. and Braakensiek, H., Phosphate removal by crystallization in a fluidized bed, *Wat. Sci. Tech.* **17**(2-3), p.133-42, 1985.
26. van Dijk, J.C. and Eggers, E., Defosfatering met een korrelreactor: een Nederlandse ontwikkeling met toekomst, *H₂O* **20**(3), p.63-68, 1987.
27. van Velsen, A.F.M. et. al., Defosfatering door magnetische separatie, *H₂O* **21**(15), p.402-411, 1988.
28. van Velsen, A.F.M. et. al., Ontwikkeling van magnetische defosfatering, *H₂O* **23**(1) p.2-8, 1990.

CHAPTER 2
CALCIUM PHOSPHATE PRECIPITATION IN A FLUIDIZED BED
IN RELATION TO PROCESS CONDITIONS:
A BLACK BOX APPROACH

Abstract

In this work the precipitation features of calcium phosphate in a fluidized bed reactor in the concentration range between 5 and 100 mg P/l were studied, and the conditions for optimum phosphate removal efficiency were established. The supply of calcium ions should be such that a Ca/P molar ratio of 3 at the inlet of the reactor is achieved. If the water to be treated does not contain magnesium or carbonate ions, the supply of base should suffice to promote a conversion of 50 - 65% of the incoming phosphate to the solid phase. In the presence of carbonate and magnesium ions, the base supply should provide a conversion of 80 - 95%. Magnesium and carbonate ions did not have a detrimental effect on the phosphate removal efficiency for inlet concentrations of up to $4.8 \cdot 10^{-3}$ and $1.8 \cdot 10^{-3}$ kmol·m⁻³, respectively. The feasibility of a process based on the precipitation of magnesium phosphate instead of calcium phosphate was demonstrated for waters with a low calcium content (Ca/P < 0.8 mol/mol). Finally a method was presented to select process conditions where co-precipitation of unwanted phases can be avoided, as well as to calculate the amount of base to be fed to the reactor.

2.1 Introduction

Several processes for removal of phosphate from wastewater are currently applied, which are based on the precipitation of phosphate salts. In the conventional routes, a reagent is added during the biological treatment of sewage, to precipitate a phosphate salt which becomes incorporated in the sludge by-product. The costs for disposal of the additional phosphate sludge, as well as the need to limit phosphate emission to the environment, has diverted the attention in recent years to processes which lead to the recovery of phosphate. Precipitation of calcium phosphate in a fluidized bed reactor is such a process.

Calcium phosphate precipitation in fluidized beds has so far been studied merely for applications where the phosphate concentrations in the water to be treated are within the range of 5 to 20 mg P/l [7,11,16,27]. Recently, the phosphate content in wastewater in the Netherlands decreased to values around 7 mg P/l mainly as a result of the large scale introduction of phosphate free detergents. These lower concentrations lead to high investment and operational costs for the fluidized bed process per unit mass of recovered phosphate. It is thus economically more attractive to apply the fluidized bed process in combination with a biological route where the phosphate is first concentrated into a small stream with a high phosphate concentration (20 to 100 mg P/l). The features of the fluidized bed process with high inlet phosphate concentrations, such as phosphate removal efficiency, mechanical stability of the phosphate grains, the reactant consumption and the sensitivity of the process to the presence of impurities were not yet determined.

Therefore a first screening study was done of a fluidized bed process with high inlet phosphate concentrations by varying operating conditions such as the inlet concentrations of calcium and phosphate and the outlet pH. Also, the effects of carbonate and magnesium ions normally encountered in the water, which can interfere with the process, were studied. Carbonate ions for example tend to co-crystallize as calcium carbonate upon the grains. Such co-crystallization has been found to be associated with a reduction in the phosphorus removal efficiency [27]. Magnesium ions at low concentrations are also known to affect the precipitation of calcium phosphate [12,19]. Besides, some wastewaters contain such a high level of magnesium ions that the precipitation of a magnesium salt instead of a calcium one occurs. Therefore the feasibility of a process where magnesium phosphate precipitates instead of calcium phosphate was also discussed.

2.2 Process description

The process is based on the precipitation of calcium phosphate obtained by mixing a phosphate solution with calcium ions and a base. The base provides a shift to the left in the chemical equilibrium given in eq. (1), thereby increasing the supersaturation.



The supersaturation β was defined depending on the crystal modification formed. For amorphous calcium phosphate (ACP) with chemical formula $Ca_3(PO_4)_2$ via the actual PO_4^{3-} activity,

$$\beta = \frac{1}{5} \ln \frac{(Ca^{2+})^3 (PO_4^{3-})^2}{K_{s,ACP}} \quad (2)$$

The brackets indicate ion activities. When magnesium ions are added instead of calcium ions, $Mg_3(PO_4)_2 \cdot 22H_2O$ may form and the supersaturation was defined analogously. A characteristic supersaturation at the reactor inlet (β_{in}) was defined as the supersaturation obtained directly after mixing of the reactants and before any precipitation takes place. In the Appendix it is shown how to calculate the supersaturation from the total (measured) concentrations of all ions in solution.

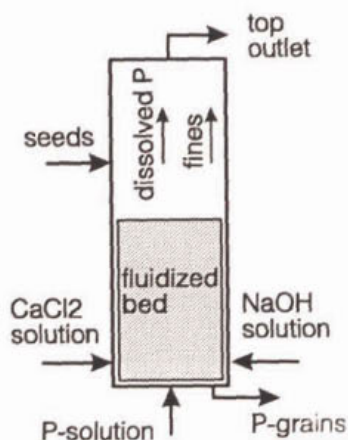


Figure 1. Schematic representation of the fluidized bed.

The core of the process is the fluidized bed (Figure 1) which is fed continuously with aqueous solutions containing phosphate ions, calcium ions and a base. Calcium phosphate precipitates upon the surface of sand grains. The phosphate covered grains are removed from the bottom of the bed and replaced intermittently by fresh sand grains.

Simultaneously to the precipitation upon the sand grains, two unwanted processes occur: primary nucleation in the liquid phase and abrasion of the mineral layer in the bed. Both processes lead to small particles (referred to as 'fines') which leave

the bed at the top and form, together with the remaining phosphate in solution, the fraction of the phosphate that is not recovered in the reactor. Aggregation of the fines with the grains, on the contrary, contribute to the phosphate recovery.

The relative importance of individual processes such as the precipitation upon the grains, primary nucleation, abrasion and aggregation depends on the supersaturation profile and thus on the hydrodynamic conditions in the bed as well as on the presence of impurities. The local supersaturation determines the nature of the crystalline phase, the kinetics of nucleation, growth and aggregation. Hydrodynamics are particularly important near the inlet nozzles, where mixing of reagents takes place, since localized high supersaturations can occur as a result of poor macromixing. Locally high supersaturations induce high nucleation rates, stimulating the production of fines. Hydrodynamics also determine the rate of aggregation and abrasion in the bed as well as the mass transfer to the grains. The presence of impurities can affect nucleation and growth rates as well as promote the precipitation of other phases in the reactor.

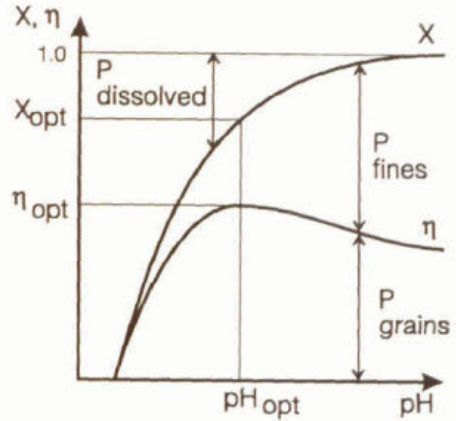


Figure 2. Phosphate streams in the fluidized bed expressed in terms of the efficiency (η) and conversion (X) as functions of the pH. The optimum values of the efficiency, conversion and pH are also indicated.

The four phosphate streams in the reactor are indicated in Figure 1. They determine the phosphate removal efficiency (η) of the reactor and the conversion of phosphate from the liquid to the solid phase (X), defined as

$$\eta = 100 \cdot (w_{P,in} - w_{P,tot}) / w_{P,in} \quad (3)$$

$$X = 100 \cdot (w_{P,in} - w_{P,sol}) / w_{P,in} \quad (4)$$

where $w_{P,in}$ represents the flow of the component phosphorus at the reactor inlet, $w_{P,tot}$ gives the total flow of phosphate both as dissolved P and as fines at the reactor outlet and $w_{P,sol}$ is the flow of dissolved P at the reactor outlet.

The phosphate streams, the efficiency and the conversion as functions of the pH at the top outlet of the reactor are illustrated in Figure 2. The optimum values of the pH (pH_{opt}),

conversion (X_{opt}) and efficiency (η_{opt}) for a given set of inlet conditions were defined as those which give the maximum efficiency and are also indicated in Figure 2.

The Ca/P and Mg/P molar ratios of the grains and fines in the fluidized bed were calculated from the calcium, magnesium and phosphate streams into and from the reactor as

$$(Me/P)_{grain} = \frac{w_{Me,in} - w_{Me,tot}}{w_{P,in} - w_{P,tot}}, \quad Me = Ca, Mg \quad (5)$$

$$(Me/P)_{fines} = \frac{w_{Me,tot} - w_{Me,sol}}{w_{P,tot} - w_{P,sol}}, \quad Me = Ca, Mg \quad (6)$$

2.3 Experimental procedure

Calcium phosphate precipitation was conducted in continuous fluidized bed reactors of two sizes. The fluidized beds had inner diameters of 0.02 and 0.05 m and a total height of 2.1 m. The details of the inlet nozzles are shown in Figure 3. The reactor was filled with sand grains as substrate for the mineral layer up to a height in rest of 0.45 ± 0.05 m. The sand grains had sizes within the range of $2 \cdot 10^{-4}$ to $6 \cdot 10^{-4}$ m. The main constituent of sand is α -quartz (SiO_2 , JCPDS 5-490), with minor amounts of anasthite ($CaAl_2Si_2O_8$, JCPDS 12-301).

The main inlet stream was an aqueous solution of $0.0004 \text{ kmol} \cdot \text{m}^{-3}$ to $0.0032 \text{ kmol} \cdot \text{m}^{-3}$ phosphoric acid neutralized with sodium hydroxide to a pH value of 4 or 6. The base stream was an aqueous solution of 0.1 to $0.2 \text{ kmol} \cdot \text{m}^{-3}$ sodium hydroxide. The calcium stream was a solution of 0.1 to $0.2 \text{ kmol} \cdot \text{m}^{-3}$ calcium chloride hexahydrate. The base and the calcium streams were fed through separate nozzles into the reactor. In some experiments the calcium and the phosphate ions were combined in the main stream, whereas in other experiments the calcium ions and the base were combined by adding a 0.1 to $0.2 \text{ kmol} \cdot \text{m}^{-3}$ $Ca(OH)_2$ suspension instead of NaOH and $CaCl_2$. The reactants were all chemical grade. Demineralized water with a conductivity of $1 \mu\text{S/cm}$ or less was used. The effect of impurities was studied by pre-mixing a magnesium chloride hexahydrate or a sodium

bicarbonate solution with the phosphate solution in a buffer vessel upstream the reactor. In addition, experiments were performed where the phosphate solution was prepared with tap water or with the effluent of a sewage treatment plant (here referred to as wastewater) enriched with phosphate. The temperature in the fluidized bed was 18 ± 3 °C. All experiments and experimental conditions are listed in Table I.

Figure 3. Details of the lower part of the fluidized beds. Beds with 0.05 m in diameter (a) and with 0.02 m in diameter (b).

The flow rates and concentrations of the elements Ca, Mg, P and Na in the streams entering the bed and leaving it through the top were measured. In addition, the inlet Ct (total inorganic carbonate) concentration was determined. The total and dissolved concentrations at the top outlet stream were measured, as well as the pH and the temperature. In order to

Table I. Experimental conditions and main results. Optimum values of pH and conversion (pH_{opt} and X_{opt}) are those of maximal efficiency (η_{opt}).

experimental conditions								results		
exp. nr.	water type	base type	D (m)	$C_{P,in}$ (mM)	$(Ca/P)_{in}$ (-)	$(Mg/P)_{in}$ (-)	Ct_{in} (mM)	pH_{opt} (-)	η_{opt} (%)	X_{opt} (%)
CaP-0	tap	Ca(OH) ₂	0.05	0.45	1.7	~0.7	<0.5	9.7	56	96
CaP-4	demi	Ca(OH) ₂	0.05	3.2	1.7	0	<0.2	6.2	52	66
CaP-7	demi	NaOH	0.05	1.6	1.5	0	<0.2	7.5	32	50
CaP-8	demi	NaOH	0.05	1.6	3	0	<0.2	6.9	42	60
CaP-9	demi	NaOH	0.05	0.8	3	0	<0.2	7.8	50	65
CaP-10	waste	NaOH	0.05	1.6	3	~0.7	1.5	7.4	32	60
CaP-11	waste	NaOH	0.05	1.6	3	~0.7	5.7	8.6	20	89
11/92	demi	NaOH	0.05	1.6	3	0.5	<0.2	8.5	40	92
36/91	demi	NaOH	0.05	1.6	3	1	<0.2	8.7	39	94
11B/92	demi	NaOH	0.05	1.6	3	2	<0.2	9.2	31	95
MgP-23	demi	NaOH	0.05	1.6	0	2	<0.2	11.2	45	75
MgP-30	demi	NaOH	0.05	1.6	0.6	1.6	<0.2	9.5	30	95
MgP-24	demi	NaOH	0.05	1.6	0.8	4.9	0.2-1.8	9.4	40	90
48/91	demi	NaOH	0.02	1.6	3	0	<0.2	7.2	40	80
MgP-20	demi	NaOH	0.02	1.6	0.8	2	0.1	9.7	40	85
MgP-13	waste	NaOH	0.02	1.6	2.1	2	3.3	9.7	11	93
MgP-19	waste	NaOH	0.02	1.6	1.7	2	0.4	9.8	22	95

measure the dissolved concentrations, the top outlet stream was filtered immediately over a 0.45 μm filter.

The concentrations of the elements P, Ca, Mg and Na were determined by inductively coupled plasma - atomic emission spectroscopy (Spectro). All samples were pre-treated with 2 N HCl in order to dissolve any suspended solids. The total carbonate concentration was measured by acid-base titration. The fines and grains were analyzed by X-ray diffraction. The grains were also analyzed by optical microscopy and scanning electron microscopy (SEM).

Contamination of the base in the storage vessel by uptake of carbonate from the air was negligible compared to the purposely added concentrations in experiment MgP-24 which matched those found in industrial practice [27].

2.4 Process characterization

2.4.1 Brief review on calcium phosphate modifications

Several calcium phosphate modifications can be formed by precipitation from solution [24]. Normally a metastable phase is formed first and undergoes one or more solution mediated recrystallization steps until the thermodynamically stable modification precipitates. For low supersaturations the sequence in which each phase is formed is in accordance with the Ostwald rule of stages [18], but at higher supersaturations and pH values (> 6) one or more amorphous compounds are formed first.

Amorphous calcium phosphate (ACP) with different characteristics - such as molecular structure, Ca/P molar ratio and solubility - may be formed depending on precipitation conditions such as the pH and the product of calcium and phosphate concentrations in solution. Table II presents some literature data on various types of ACP. For pH values between 7 and 10, ACP is a well defined compound, which is amorphous to both x-ray and electron diffraction and has a Ca/P molar ratio between 1.45 and 1.51. This holds for low

concentrations of the calcium and phosphate ions ($< 1.2 \cdot 10^{-4} \text{ kmol}^2 \cdot \text{m}^{-6}$) [4,20,22,29,31,32] as well as for high concentrations ($5 \cdot 10^{-4}$ to $3.75 \cdot 10^{-2} \text{ kmol}^2 \cdot \text{m}^{-6}$) [9,14]. For pH values higher than 10, ACP has a variable solubility and Ca/P molar ratio [22]. At higher concentrations ($> 1.0 \cdot 10^{-4} \text{ kmol}^2 \cdot \text{m}^{-6}$) a spherular form of ACP has also been encountered [8]. It transforms within 2 to 5 min into a floccular amorphous phase. Both modifications have Ca/P ratios between 1.34 and 1.37. Other phases have also been observed as precursors of hydroxyapatite (HAP) crystallization within the range of concentrations and pH values just mentioned: Abbona and Franchini-Angela [2] found poorly crystalline HAP whereas Francis and Webb [13] precipitated an amorphous dicalcium phosphate dihydrate (DCPD) with a Ca/P ratio of 1.22.

Amorphous calcium phosphate precipitates first and recrystallizes into hydroxyapatite. The process is characterized by a slow increase in the crystallinity of the suspension as well as in the Ca/P ratio of the crystals [8,21,22]. A poorly crystalline HAP is initially formed, but crystallinity improves with time as ripening and growth of HAP proceed [29].

Table II. Summary of literature data on the characteristics of amorphous calcium phosphate (ACP) .

solution pH (-)	solution Ca x P (mM ²)	crystal Ca/P (mol/mol)	note	literature
7-10	7-120	1.48 ± 0.03		[4,14,20,22] [29,31,32]
9.25-12.5	24	variable	ACP structure varies with pH	[22]
7-8	25	-	HAP poorly crystalline	[2]
7.4-9.4	300	1.35 ± 0.02 1.35 ± 0.02	ACP1, spherular ACP2, floccular	[8]
7.4	16-100	1.22	amorphous DCPD	[13]
9.8	37500	1.42 1.52	ions Cl^- ions NO_3^-	[9,10]

2.4.2 Calcium phosphate precipitation in a fluidized bed

The features of calcium phosphate precipitation analyzed in the previous section are discussed here in relation to the precipitation in a fluidized bed. When characterizing the product formed in a fluidized bed, not only the complexities of the structure of ACP and its transformation to other modifications have to be taken into account, but also the inhomogeneities in the reactor:

- the supersaturation is not constant throughout the reactor, but decreases with bed height. As more and more phosphate precipitates, the local pH decreases. The pH may vary up to 2 pH units throughout the reactor (see section 2.4.4.3).
- locally high supersaturations may develop near the inlet nozzles.
- the grains do not occupy a fixed position in the bed, but travel up and down continuously through zones of different supersaturation.
- the residence time of the grains in the reactor ($\sim 10^6$ s) is much larger than the time required for recrystallization of ACP into HAP (~ 1000 s,[4]). The residence time of fines (~ 100 s), on the other hand, is shorter than the recrystallization time, so more than one modification may develop simultaneously in the reactor.

The grains and fines produced in the fluidized bed are therefore likely to be a mixture of amorphous and crystalline materials with slightly different chemical formulas and solubilities, which result from the varying chemical and hydrodynamic conditions in the reactor. In order to simplify the analysis of the reactor behavior, it was convenient to assume that the grains and fines were one single compound with characteristics independent of process conditions. This assumption was roughly supported by our experimental data, as will be shown in section 2.4.4.3.

2.4.3 Characterization of the grains and fines

2.4.3.1 Grains and fines produced at pH values higher than 7

Table III summarizes the results of X-ray and chemical analysis of the produced grains. For pH values higher than 7 (exp. CaP-7,8 and 9) a poorly crystalline TCP was formed, as can be deduced from the Ca/P ratio and from the broad x-ray diffraction peaks (not shown). The

x-ray pattern and the chemical composition of the fines were identical to those of the grains. Light microscopy confirmed the amorphous nature of the grains (not shown) and SEM views revealed a compact mineral layer with a smooth surface (Figure 4a).

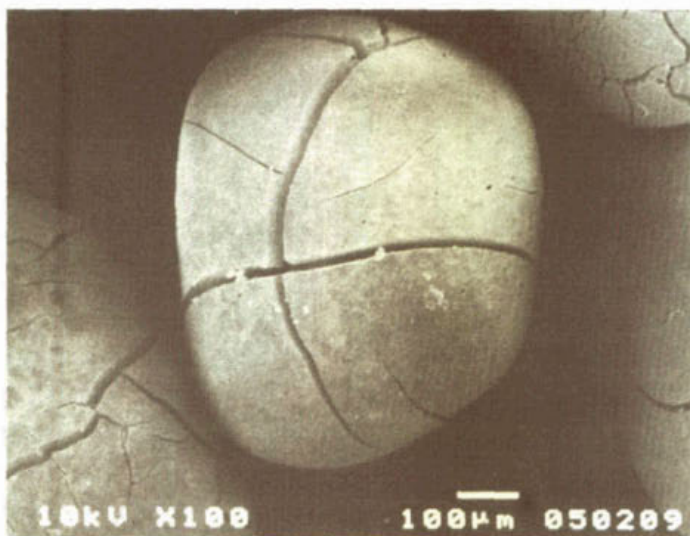
Table III. Overview of X-ray and chemical analysis of the grains.⁽¹⁾ ions Ca, P, Na, Cl always present. + = high concentration, - = low. ⁽²⁾ low crystallinity. n.m. = not measured.

liquid phase				grains		
exp. nr.	ions present ⁽¹⁾	type water	pH -	Ca/P -	Mg/P -	modification
CaP-7,8,9	-	demi	>7	1.45-1.6	-	TCP ⁽²⁾
CaP-4	-	demi	6-7	1.26	-	DCPD + ACP
CaP-0,10,11	Mg(-), Ct	tap/waste	>7	1.53	n.m.	ACP
11/92	Mg(-)	demi	>7	n.m.	n.m.	ACP
11B/92	Mg(+), Ca(+)	demi	>7	1.28	0.28	ACP
MgP-20	Mg(+), Ca(-)	demi	>7	0.14	1.35	MgP, ACP
MgP-19	Mg(+), Ct	waste	>7	0.52	1.18	CaMgCt, ACP, MgP

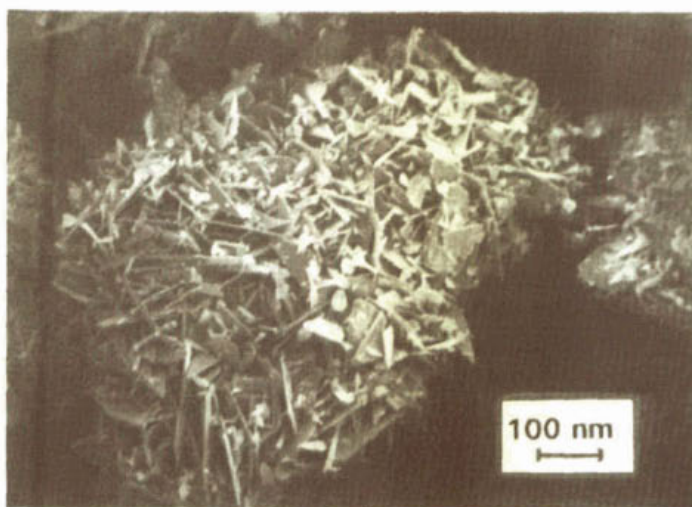
The grains and fines formed in the fluidized bed are assumed to be ACP with the molecular formula $\text{Ca}_3(\text{PO}_4)_2$, which is consistent with the measured Ca/P ratio, of 1.45 to 1.6. A solubility $K_{s, \text{ACP}}$ of $3 \cdot 10^{-27} \text{ kmol}^5 \cdot \text{m}^{-15}$ (based on activities) was fitted to the experimental results as will be shown in section 2.4.4.2.

2.4.3.2 Grains and fines produced at pH values between 6 and 7

For pH values within the range of 6 to 7 (exp. CaP-4), the grains were identified as dicalcium phosphate dihydrate (DCPD) by x-ray diffraction. The grains had an inner amorphous layer and an outer crystalline layer (observed from light microscopy of the cross section of the grains, not shown), the latter consisting of platelike DCPD crystals with lengths of 10 to 100 μm (Figure 4b). The Ca/P molar ratio in the grains was 1.26 ± 0.05 ,

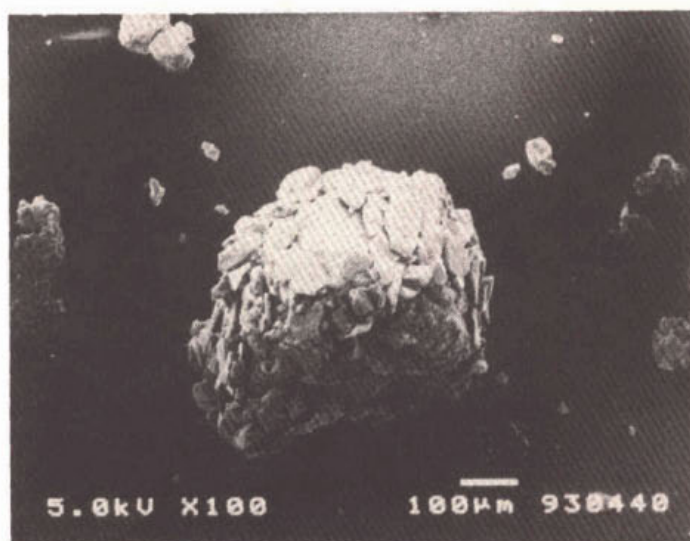


(a)



(b)

Figure 4a,b. SEM views of grains from exp. CaP-8 (a) and CaP-4 (b).



(c)



(d)

Figure 4c,d. SEM view of a grain from exp. MgP-20 (c) and a detail of the same grain (d) showing hexagonal magnesium phosphate crystals mixed with an amorphous phase (ACP).

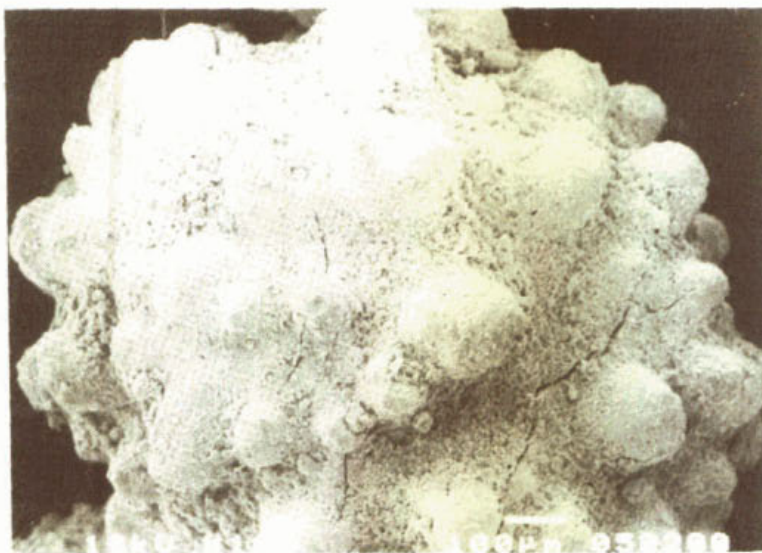


Figure 4e. SEM view of a grain taken from an intermediate axial position in the fluidized bed in exp. 11/92.

consistent with a mixture of ACP and DCPD. The crystalline layer was either formed directly or via a solution mediated recrystallization of the originally amorphous phase. This could have happened overnight, when the bed was not operated. Once formed the crystalline phase was likely to continue its growth, since the pH was 7 or lower. Abbona et. al. [1] found that the first phases formed under similar conditions at pH values of 6 and 7 were respectively DCPD and ACP, consistent with our results. It was not possible to obtain reliable measurements for the Ca/P molar ratio of the fines because of the presence of a relatively large amount of undissolved calcium hydroxide.

2.4.3.3 Effect of magnesium ions on the grains characteristics

Magnesium ions can affect the characteristics of the produced grains in two ways: it stabilizes ACP through inhibition of the development of a crystalline modification [2] and it may co-precipitate as $Mg_3(PO_4)_2 \cdot 22H_2O$ (MgP). The first effect was observed in experiments with tap water (exp. CaP-0), wastewater (exp. CaP-10 and CaP-11) or demineralized water to which magnesium was added (exp. 11/92 and 11B/92), where an x-ray amorphous calcium phosphate similar to that described earlier [4,20,22,29,31,32] was formed (Table III). The

morphology of the grains (not shown) was similar to that obtained in the absence of magnesium. Substantial co-precipitation was observed for a solution containing high magnesium and low calcium concentration (exp. MgP-20), where the grains were covered by a mixture of $\text{Mg}_3(\text{PO}_4)_2 \cdot 22\text{H}_2\text{O}$ and x-ray amorphous calcium phosphate. Magnesium phosphate was present as hexagonal platelike crystals, intermingled with irregularly shaped ACP (Figure 4c,d). Hexagonal magnesium phosphate crystals were also found by SECKLER [26] in the absence of calcium ions. If ammonium ions are also present, struvite ($\text{NH}_4\text{MgPO}_4 \cdot 6\text{H}_2\text{O}$) develops instead of magnesium phosphate [26].

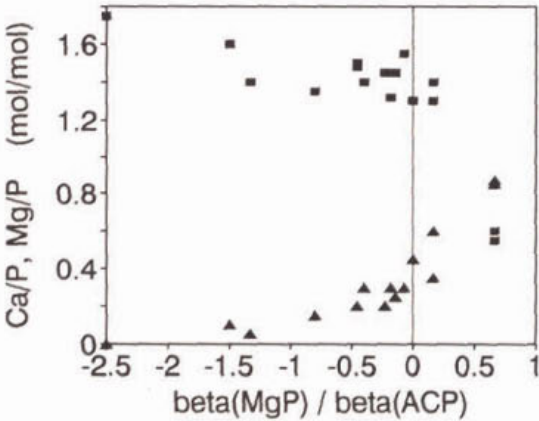


Figure 5 Ca/P (■) and Mg/P (▲) molar ratios of the grains as functions of the inlet supersaturation ratio. β_{ACP} is always positive, so negative values of the ratio indicate undersaturation with respect to MgP.

The Ca/P and Mg/P molar ratios in the grains were calculated from eq.(5) and eq.(6) for a wide range of supersaturation ratios $\beta_{\text{MgP}}/\beta_{\text{ACP}}$ (Figure 5). The solution was always supersaturated with respect to ACP ($\beta_{\text{ACP}} > 0$) so negative values of the ratio $\beta_{\text{MgP}} / \beta_{\text{ACP}}$ indicate undersaturation with respect to MgP ($\beta_{\text{MgP}} < 0$). Figure 5 shows that the grains incorporate variable amounts of magnesium, depending on the

supersaturation ratio. For solutions undersaturated with respect to MgP the only modification formed was ACP so magnesium must be incorporated in the ACP. For solutions supersaturated with respect to both ACP and MgP part of the magnesium was present as co-crystallized MgP.

2.4.3.4 Effect of carbonate ions on the grains characteristics

When not only calcium and phosphate ions were present, but also carbonate and magnesium ions (exp. MgP-19), the Ca/P and Mg/P molar ratios were 0.52 and 1.18 respectively,

consistent with a mixture of $\text{CaMg}(\text{CO}_3)_2$ (9 mol%), $\text{Mg}_3(\text{PO}_4)_2 \cdot 22\text{H}_2\text{O}$ (25 mol%) and ACP (66 mol%). The two former phases were also identified by x-ray diffraction. These conditions should be avoided in normal operation of the fluidized bed, since the phosphate removal efficiency was low, probably due to the poor mechanical resistance of these mixed grains. Besides, part of the calcium (or magnesium) ions added to the reactor are wasted, since they are consumed to precipitate $\text{CaMg}(\text{CO}_3)_2$ instead of a phosphate salt.

2.4.3.5 Mechanical stability of the grains

Grains sampled from the middle of the bed often had an irregular surface with aggregated particles upon it (Figure 4e). Grains removed from the bottom of the bed typically showed a compact mineral layer with a smooth surface (Figure 4a), probably the result of abrasion. Abrasion is likely to be more intense at the bottom of the bed, where the energy dissipation is the highest (the energy dissipation at the bottom results from the energy required to keep fluidization and from the dissipation of the kinetic energy of the main inlet stream, which is added to the reactor via a nozzle with a velocity of 1 m/s, whereas upwards in the bed merely energy needed for fluidization is dissipated).

2.4.4 Conversion

2.4.4.1 Optimum conversion

The optimum conversion (X_{opt}) for a given set of inlet conditions was defined in section 2.2 as the conversion corresponding to the maximum efficiency. When the water to be treated contained magnesium or carbonate ions, X_{opt} reached values within the range of 80 to 95%, whereas in the absence of these ions values between 50 and 65% were obtained (Table I). Since most wastewaters contain some carbonate and magnesium ions, in practice fluidized beds for phosphate removal will operate at conversions between 80 and 95%.

Low X_{opt} values are desirable because they imply a low base consumption, which is an important component in the operating costs of a fluidized bed for phosphate removal.

2.4.4.2 Calculation of equilibrium conversion

Typically, ACP precipitation is characterized by an abrupt increase in conversion at the first

stage of the precipitation. After this first stage, conversion further increases slowly. Characteristic times of ~ 10 s for the conversion in the first stage were measured in our reactor (Chapter 3) and the additional conversion attained upwards till the top outlet of the reactor was marginally higher than the initial value, so the solution leaving the top outlet of the reactor can be considered to be in equilibrium with the solids. The equilibrium conversion can be calculated from the inlet conditions, so the actual conversion in the fluidized bed can be predicted for each set of inlet conditions.

A mathematical model for the calculation of the equilibrium conversion for the system $\text{Ca-PO}_4\text{-OH}$ is presented in the Appendix. For the system $\text{Ca-Mg-PO}_4\text{-Ct-OH}$ the public domain software MINTEQA [3] was used. The model inputs were the concentrations of calcium, magnesium, phosphate and carbonate ions as well as the counter ions sodium and chloride after mixing of reactants but before precipitation. ACP was assumed to have the chemical formula $\text{Ca}_3(\text{PO}_4)_2$ and a solubility of $3 \cdot 10^{-27} \text{ kmol}^5 \cdot \text{m}^{-15}$. This solubility value was the only model parameter and was obtained by fitting from our experimental data. The model outputs were the solution pH and the supersaturation. Precipitation of ACP until equilibrium was also simulated, so the equilibrium conversion and the pH after precipitation were calculated as well.

When two or more phases precipitate simultaneously, the conversion cannot be predicted because the relative amounts of the precipitating phases are not known in advance. However, the equilibrium model can be used to calculate the inlet supersaturations with respect to the possible solids, so process conditions can be chosen which avoid the formation of an unwanted phase. For instance, as has already been shown, the incorporation of magnesium ions increases drastically for positive values of β_{MgP} (Figure 5), indicating co-precipitation of $\text{Mg}_3(\text{PO}_4)_2 \cdot 22\text{H}_2\text{O}$.

2.4.4.3 Comparison between calculated and measured conversions

In general the conversion (measured at the reactor top outlet) increases with the amount of base fed to the reactor and therefore with the measured top outlet pH, approaching a value of 100% for a sufficiently high base addition. An example is presented in Figure 6. The spread in the measured conversion was large because only part of the total flow was sampled.

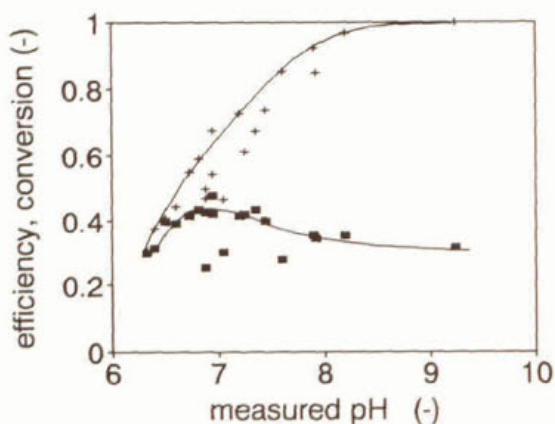


Figure 6 Efficiency and conversion in exp. CaP-8 as functions of the pH at the reactor outlet.

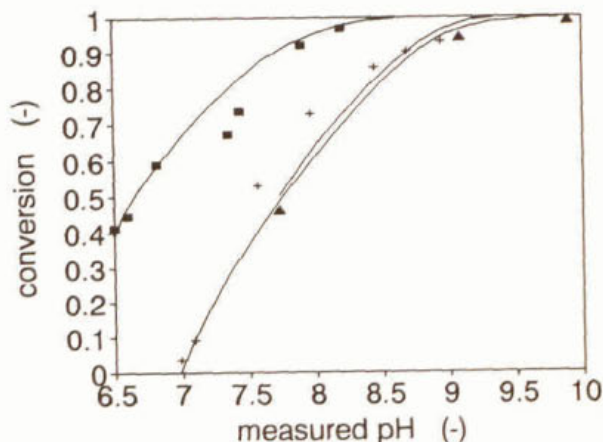


Figure 7. Measured (data points) and predicted (lines) conversion as functions of the measured top outlet pH for waters with carbonate ions (+, exp. CaP-11), magnesium ions (▲, exp. 11B/92) and without these ions (■, exp. CaP-8).

form complexes with calcium and phosphate ions, so reducing the concentration of Ca^{2+} and PO_4^{3-} available for precipitation.

The sampling procedure was later optimized (the total flow was sampled) so the reproducibility improved substantially (see for example the conversion versus pH curve of experiment CaP-11 in Figure 7).

The calculated conversions matched the measured conversions reasonably well at varying calcium, phosphate, carbonate and magnesium concentrations, at measured pH's between 6 and 11 and for different types of phosphate solution (P-enriched demineralized water and P-enriched wastewater). This is illustrated in Figure 7 for varying carbonate and magnesium concentrations (exp. CaP-8, 11B/92 and CaP-11). An increase in the total concentrations of magnesium or carbonate ions produced a shift to the right in the conversion vs. pH curve. This shift occurred because these ions

As the concentration of calcium and phosphate increased, the conversion curve shifted to the left (not shown), a result of the direct effect of these variables on the supersaturation (see eq.(2)).

The equilibrium behavior of wastewater solutions was well described by the system Ca-Mg-PO₄-Ct (Figure 7, exp. CaP-11), indicating that the influence of impurities normally present in wastewater, other than carbonate and magnesium, upon the equilibrium is minor.

Since the equilibrium conversion described most experiments quite well, it was concluded that the chemical formula of TCP and a solubility of $3 \cdot 10^{-27} \text{ kmol}^5 \cdot \text{m}^{-15}$ represent well the structure of ACP in the range of conditions studied.

The pH values before and after precipitation were also calculated. However, the calculated pH after precipitation was 1 pH unit lower than the pH measured at the top outlet of the fluidized bed, so the model does not predict the measured pH accurately. The pH was calculated to decrease up to 2 pH units as a consequence of the precipitation process.

The ability to predict the conversion can be used to determining the operating range of the fluidized bed reactor by noting that generally the optimum efficiency was obtained when the conversion was within the range of 50 - 65% in the absence of carbonate and magnesium ions and 80 - 95% otherwise (Table I). The amount of base to be added needed to obtain the required conversion can be calculated if the composition of the water to be treated is known. Optimization of the efficiency can then be achieved by adaptations within a narrow range of base addition.

The conversion cannot be used as a parameter to determine the value of the efficiency. Prediction of the efficiency through the supersaturation at the reactor bottom before precipitation (β_m) also failed, as can be deduced from experiments with various phosphate and calcium concentrations (exp. CaP-7,8,9). They all had common β_m values (not shown), but resulted in different efficiencies. The efficiency when treating water of a given composition can only be determined experimentally.

2.4.5 Phosphate removal efficiency

2.4.5.1 Effect of start-up

During start-up the phosphate removal efficiency depends on the precipitation of ACP upon the surface of the bare sand grains. As time proceeds, a calcium phosphate mineral layer develops upon the sand grains, so that precipitation upon calcium phosphate takes place.

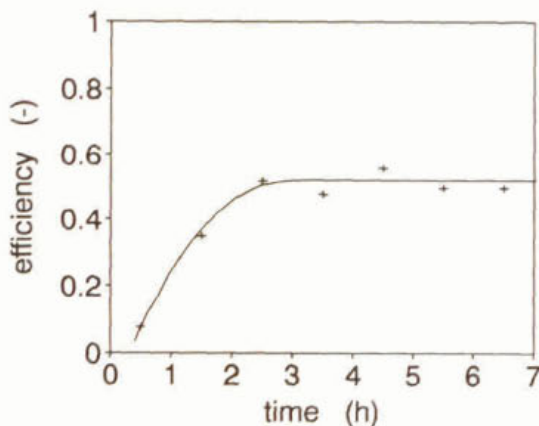


Figure 8 Efficiency against time during start-up (exp. CaP-4). At $t=0$ the fluidized bed is filled with bare sand grains. Inlet P concentration = $3.2 \cdot 10^{-3} \text{ kmol} \cdot \text{m}^{-3}$.

The efficiency vs. time curve for exp. CaP-4 (Figure 8) shows that the growth upon a sand surface was less favorable than growth upon a calcium phosphate surface. After a period of 3 h, when the calcium phosphate layer had an average thickness of $2 \mu\text{m}$, a constant efficiency was obtained. JOKO [17] found a similar effect for a fixed bed with low inlet phosphate concentrations. The thickness of $2 \mu\text{m}$ found in our experiments corresponded to a phosphate concentration in the grains of 4 mg P/g grain, which compares well with the value found by JOKO [17], of 1 mg P/g grain.

2.4.5.2 Effect of the inlet phosphate concentration (P_{in})

The optimum efficiency for experiments with varying P_{in} (exp. CaP-0,4,8,9) is shown in Figure 9. The optimum efficiency increased for a decreasing inlet phosphate concentration. The experiment with the highest P_{in} value of $3.2 \cdot 10^{-3} \text{ kmol} \cdot \text{m}^{-3}$ (exp. CaP-4) formed an exception to this general trend, due to the crystal modification formed (DCPD), which was different from ACP found in the other experiments. The development of this DCPD probably came from the discontinuous operation of the bed. At the lowest P_{in} value, JOKO [17] and SECKLER [27] have found optimum efficiencies similar to those reported in Figure 9.

The use of a $\text{Ca}(\text{OH})_2$ suspension instead of a NaOH solution in exps. with P_{in} values of 0.4 and 3.2 (exp. CaP-0 and CaP-4) also contributed to an improvement of the optimum

efficiency. The $\text{Ca}(\text{OH})_2$ particles are likely to dissolve slowly along the bed length, distributing the supersaturation more evenly throughout the bed, and thus favoring growth upon the grains and aggregation of developed fines with the grains.

2.4.5.3 Effect of the inlet Ca/P molar ratio ($(\text{Ca}/\text{P})_{\text{in}}$)

When comparing $(\text{Ca}/\text{P})_{\text{in}}$ values of 3 and 1.5 (exps. CaP-8 and CaP-7) the former resulted in a higher optimum efficiency (Table I), showing the need to add calcium ions to the reactor in an amount above the stoichiometric value for ACP (1.5).

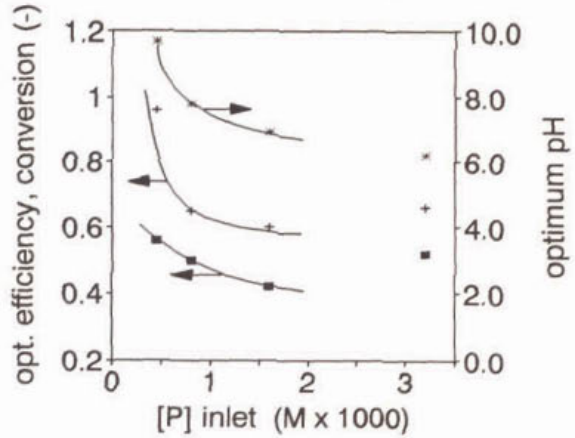


Figure 9. Optimum efficiency (■), optimum conversion (+) and optimum pH (*) as functions of the inlet P concentration. DCPD precipitated at the highest P concentration, otherwise ACP was formed. Exp. CaP-0, CaP-9, CaP-8 and CaP-4.

2.4.5.4 Effect of the water type, carbonate and magnesium ions

The use of P-enriched wastewater (exp. CaP-10, $\eta=32\%$) led to a lower optimum efficiency than a similar experiment with P-enriched demineralized water (exp. CaP-8, $\eta=42\%$). The difference can be partly attributed to the carbonate content in the wastewater ($1.5 \cdot 10^{-3} \text{ kmol} \cdot \text{m}^{-3}$). By further increasing the carbonate content in the wastewater up to $6.8 \cdot 10^{-3} \text{ kmol} \cdot \text{m}^{-3}$ (exp. CaP-11) the optimum efficiency dropped even more ($\eta=20\%$). The measured Ca/P molar ratio in the grains was 1.54, indicating that only minor co-crystallization of CaCO_3 occurred. CaCO_3 co-crystallization has been observed in an industrial scale fluidized bed when the total carbonate content of the water was higher than $1 \cdot 10^{-3}$ to $2 \cdot 10^{-3} \text{ kmol} \cdot \text{m}^{-3}$ [27].

Magnesium ions are always present in wastewaters. When the inlet Mg/P molar ratio, $(\text{Mg}/\text{P})_{\text{in}}$, was lower than 2, the optimum efficiency was not affected. Above this value, the optimum efficiency decreased, as shown in Figure 10 (experiments CaP-8, 11/92, 36/91 and

11B/92).

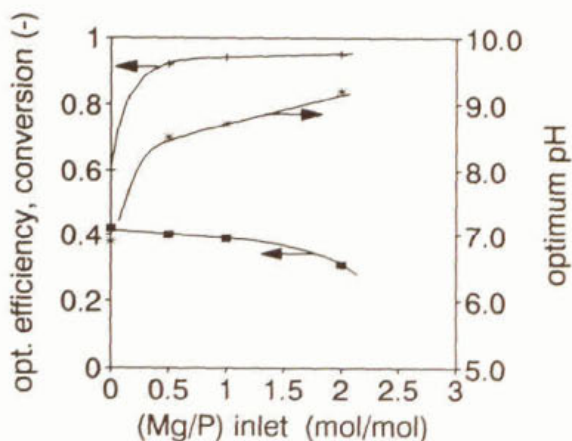


Figure 10. Efficiency (■), optimum conversion (+) and optimum pH (*) as functions of the Mg/P molar ratio at the reactor inlet. Exp. CaP-8, 11/92, 36/92 and 11B/92.

When the wastewater already contains high magnesium concentrations, it might be advantageous to substitute the calcium stream by a small, supplementary, magnesium stream. In the absence of calcium ions, an optimum efficiency of 45% was found for the precipitation of $\text{Mg}_3(\text{PO}_4)_2 \cdot 22\text{H}_2\text{O}$ (exp. MgP-23). Similar efficiencies have previously been obtained for the precipitation of struvite ($\text{NH}_4\text{MgPO}_4 \cdot 6\text{H}_2\text{O}$) [26]. When the calcium concentration was low ($\text{Ca/P} < 0.8$), a mixture of $\text{Mg}_3(\text{PO}_4)_2 \cdot 22\text{H}_2\text{O}$ and ACP was formed and efficiencies similar to those found during calcium phosphate precipitation were obtained (exp. MgP-20) even if the water contained carbonate concentrations of up to $1.8 \cdot 10^{-3} \text{ kmol} \cdot \text{m}^{-3}$ (exp. MgP-24). The $(\text{Mg/P})_{\text{in}}$ should be 2 or higher (compare exp. MgP-20 and MgP-30). If $0.8 < (\text{Ca/P})_{\text{in}} < 1.5$, ACP precipitated preferentially at a calcium supply insufficient to provide for a high efficiency ($(\text{Ca/P})_{\text{in}} < 3$, see section 2.4.5.3), so the optimum efficiency was low (exp. 11B/92).

2.4.5.5 Effect of the reactor size

The efficiencies obtained in the reactors with diameters 0.05 m and 0.02 m were the same (experiments CaP-8 and 48/91, as well as MgP-24 and MgP-20 in Table I).

2.5 Conclusions

A parametric study of the phosphate removal in a fluidized bed reactor was made. The

phosphate removal efficiency depends on the composition of the water to be treated, and a maximum efficiency of 50% was achieved. In general, the calcium ions supply should be enough to bring the inlet Ca/P molar ratio to the value of at least 3. The base supply should suffice to reach a conversion of 50 - 65% in the absence of carbonate and magnesium ions and of 80 - 95% in their presence. The pH values corresponding to these conditions were generally within the range 7.5 to 9.

Generally a low inlet phosphate concentration favors high efficiencies (56% for $0.5 \cdot 10^{-3}$ kmol \cdot m $^{-3}$ P and 42% for $1.6 \cdot 10^{-3}$ kmol \cdot m $^{-3}$ P).

The amorphous calcium phosphate formed was suitably represented by the chemical formula $\text{Ca}_3(\text{PO}_4)_2$, having a pH independent solubility of $3 \cdot 10^{-27}$ kmol 5 \cdot m $^{-15}$ (based on activities). Substantial co-crystallization of $\text{Mg}_3(\text{PO}_4)_2 \cdot 22\text{H}_2\text{O}$ occurred for high concentrations of magnesium ions and low concentrations of calcium ions in the water (molar ratios $\text{Mg}/\text{P} > 1.6$ and $\text{Ca}/\text{P} < 0.8$). When the calcium, magnesium and carbonate ions were present ($\text{Ca}/\text{P} = 1.6$, $\text{Mg}/\text{P} = 2$ and $\text{Ct} = 0.4 \cdot 10^{-3}$ kmol \cdot m $^{-3}$), not only ACP and $\text{Mg}_3(\text{PO}_4)_2 \cdot 22\text{H}_2\text{O}$ were formed, but also $\text{CaMg}(\text{CO}_3)_2$.

Chemical equilibrium relationships can be used to select process conditions where co-precipitation of unwanted phases are avoided, as well as to calculate the amount of base to be fed to the reactor.

Magnesium ions dissolved in the water to be treated can be tolerated at inlet Mg/P molar ratios of 2 or less. Carbonate contents of $1.8 \cdot 10^{-3}$ kmol \cdot m $^{-3}$ or less can be tolerated. If the water contains low calcium concentrations (inlet molar Ca/P ratio < 0.8), substitution of the calcium stream by a magnesium stream may be applied to precipitate magnesium phosphate at efficiencies comparable to calcium phosphate precipitation.

2.6 Appendix: Mathematical model for the chemical equilibrium for the system Ca-PO $_4$ -OH

A quantitative description of the chemical equilibria in an aqueous solution for the system

Ca-PO₄-OH is presented, based on mass balances, chemical equilibrium relations, and electroneutrality in the liquid phase [30,15,23]. The components considered are calcium, phosphate as well as the counter ions chlorine and sodium. These components are present in solution as a large number of ions and complexes.

A mass balance for the components Ca and P in the liquid phase is

$$c_{P,in} \cdot (1-X) = [PO_4^{3-}] + [HPO_4^{2-}] + [H_2PO_4^-] + [H_3PO_4^0] + [CaH_2PO_4^+] + [CaHPO_4^0] + [CaPO_4^-] \quad (1)$$

$$c_{Ca,in} - \frac{3}{2}c_{P,in} \cdot X = [Ca^{2+}] + [CaOH^+] + [CaH_2PO_4^+] + [CaHPO_4^0] + [CaPO_4^-] \quad (2)$$

The mass balances for the components Na and Cl are just identities, since these components neither form any complex in relevant amounts nor participate in the precipitation reaction:

$$c_{Na,in} = [Na^+] \quad (3)$$

$$c_{Cl,in} = [Cl^-] \quad (4)$$

The electroneutrality requirement gives

$$[H^+] + 2 \cdot [Ca^{2+}] + [CaOH^+] + [CaH_2PO_4^+] + [Na^+] = [OH^-] + 3 \cdot [PO_4^{3-}] + 2 \cdot [HPO_4^{2-}] + [H_2PO_4^-] + [CaPO_4^-] + [Cl^-] \quad (5)$$

The concentrations of the ions and complexes are determined from the following chemical equilibrium relations:

$$K_w = (H^+)(OH^-) = 1.0 \cdot 10^{-14} \text{ kmol}^2 \cdot \text{m}^{-6} \quad (6)$$

$$K_1 = (H^+)(H_2PO_4^-)/(H_3PO_4^0) = 7.1 \cdot 10^{-3} \text{ kmol} \cdot \text{m}^{-3} \quad (7)$$

$$K_2 = (H^+)(HPO_4^{2-})/(H_2PO_4^-) = 6.3 \cdot 10^{-8} \text{ kmol} \cdot \text{m}^{-3} \quad (8)$$

$$K_3 = (H^+)(PO_4^{3-})/(HPO_4^{2-}) = 4.5 \cdot 10^{-13} \text{ kmol} \cdot \text{m}^{-3} \quad (9)$$

$$K_4 = (Ca^{2+})(OH^-)/(CaOH^+) = 5.0 \cdot 10^{-2} \text{ kmol} \cdot \text{m}^{-3} \quad (10)$$

$$K_5 = (Ca^{2+})(PO_4^{3-})/(CaPO_4^-) = 3.5 \cdot 10^{-7} \text{ kmol} \cdot \text{m}^{-3} \quad (11)$$

$$K_6 = (Ca^{2+})(HPO_4^{2-})/(CaHPO_4^0) = 2.0 \cdot 10^{-3} \text{ kmol} \cdot \text{m}^{-3} \quad (12)$$

$$K_7 = (Ca^{2+})(H_2PO_4^-)/(CaH_2PO_4^+) = 3.98 \cdot 10^{-2} \text{ kmol} \cdot \text{m}^{-3} \quad (13)$$

The complexes involving the ions sodium and chloride do not affect the chemical equilibria substantially and are thus neglected. The concentration and the activity of an ion with valence ν are related by

$$(A^\nu) = \gamma_\nu [A^\nu] \quad (14)$$

The activity coefficients were estimated from the Davies equation [6]:

$$\log(\gamma) = -0.5 \cdot \nu_i^2 \left(\frac{\sqrt{\mu}}{1 + \sqrt{\mu}} - 0.2\mu \right) \quad (15)$$

$$\mu = \frac{1}{2} \sum_1^i [A_i] \cdot v_i^2 \quad (16)$$

The concentrations of the components $c_{P,in}$, $c_{Ca,in}$, $c_{Na,in}$, $c_{Cl,in}$ as well as the conversion (X) are experimentally determined. The previous equations form a closed set of non-linear equations which is solved by the multi-variable method of Newton-Raphson [25]. The concentrations of all ions and complexes in solution are thus obtained. At the reactor bottom, after mixing of the inlet streams but before precipitation, the conversion X is just zero, so the supersaturation and inlet pH are calculated. At the reactor outlet, the ions are allowed to vanish from solution (due to precipitation) until the supersaturation equals zero, so the equilibrium conversion and the outlet pH are derived.

List of symbols

()	activity, $\text{kmol} \cdot \text{m}^{-3}$	η	efficiency, -
[]	concentration, $\text{kmol} \cdot \text{m}^{-3}$	ν	valence, -
c	concentration, $\text{kmol} \cdot \text{m}^{-3}$	<i>Subscripts</i>	
Ct	total CO_3^{2-}	in	inlet reactor
D	reactor diameter, m	grain	sand covered with mineral layer
K_s	solubility product, $\text{kmol}^5 \cdot \text{m}^{-15}$	opt	optimum
X	conversion, -	tot	component as fines and in solution at the reactor outlet
w_A	flow rate of component A, $\text{kg} \cdot \text{s}^{-1}$	sol	component in dissolved form at the reactor outlet
<i>Greek letters</i>		<i>Solid phases</i>	
β	supersaturation, -	ACP	amorphous calcium phosphate, $\text{Ca}_3(\text{PO}_4)_2$
β_{in}	supersaturation at the reactor inlet after mixing of reactants and before precipitation, -	CaMgCt	calcium magnesium carbonate, $\text{CaMg}(\text{CO}_3)_2$
γ	activity coefficient, -		
μ	ionic strength, $\text{kmol} \cdot \text{m}^{-3}$		

DCPD	dicalcium phosphate dihydrate, $\text{CaHPO}_4 \cdot 2\text{H}_2\text{O}$	MgP	magnesium phosphate, $\text{Mg}_3(\text{PO}_4)_2 \cdot 22\text{H}_2\text{O}$
HAP	hydroxyapatite, $\text{Ca}_{10}(\text{PO}_4)_6(\text{OH})_2$	TCP	tricalcium phosphate, $\text{Ca}_3(\text{PO}_4)_2$

References

1. Abbona F. et al., The initial phases of calcium and magnesium phosphates precipitated from solutions of high to medium concentrations, *J. Cryst. Growth* **74**(3), p.581-90, 1986.
2. Abbona, F. et Franchini-Angela, M., Crystallization of calcium and magnesium phosphates from solutions of low concentration, *J. Cryst. Growth* **104**, p.661-671, 1990.
3. Ambrose, R.B. et al. Environmental software at the U.S. environmental protection agency's center for exposure assessment modeling, submitted to *Environmental Software*, Feb. 1989.
4. Boskey, A.L. and Posner, A.S., Conversion of amorphous calcium phosphate to microcrystalline hydroxyapatite. A pH dependent, solution mediated, solid-solid conversion, *J. Phys. Chem.* **77**(19), p.2313-2317, 1973
5. Boskey, A.L. and Posner, A.S., Formation of hydroxyapatite at low supersaturation, *J. Phys. Chem.* **80**(1), p.40-5, 1976.
6. Davies, C.W. *Ion Association*, Butterworths, London, 1962.
7. Dijk, J.C.van and Braakensiek, Phosphate removal by crystallization in a fluidized bed, *H. Wat. Sci. Tech.* **17**(2-3), p.133-142, 1984.
8. Christoffersen, J. et al., A contribution to the understanding of the formation of calcium phosphates, *J. Cryst. Growth* **94**, p.767-777, 1989.
9. Eanes, E.D. and Posner, A.S., Kinetics and mechanism of conversion of noncrystalline calcium phosphate to crystalline hydroxyapatite, *Trans. New York Academy of Sciences, Meeting of the Div. of Biophysics*, Nov. 18, 1965.
10. Eanes, E.D., Gillissen, I.H. and Posner, A.S., Intermediate states in the precipitation of hydroxyapatite, *Nature*, October 23, p.365-367, 1965.
11. Eggers, E. and Kiestra, Der Kornreaktor zur Phosphatentfernung aus Abwaesser: von

Labor bis Grossmasstab, *H. ISSW Seminar*, Karlsruhe, 1988.

12. Fergusson, J.F. et. al. Calcium phosphate precipitation at slightly alkaline pH values, *J.W.P.C.F.* **45** (4), p.621-631, 1973.
13. Francis, M.D. and Webb, N.C., Hydroxyapatite formation from a hydrated calcium monohydrogen phosphate precursor, *Calc. Tiss. Res.* **6**, p.335-42, 1971.
14. Fueredi Milhofer et. al., Crystal growth and phase transformation in the precipitation of calcium phosphates, *Faraday Discuss. Chem. Soc.* **61**(Precipitation), p.184-93, 1976.
15. Hagen, A.R., Calcium orthophosphate solubilities as represented by a model in three dimensions, *Acta Odontol. Scand.* **33**(2), p.67-83, 1975.
16. Hirasawa, I. and Toya, Y. Fluidized-bed process for phosphate removal by calcium phosphate crystallization, *A.C.S. Symp. Ser.* **438**, p.355-363, 1990.
17. Joko, I., Sawada S., Goto, C. and Toyokura, K. Phosphorus removal from wastewater by crystallization method: preparation and performance of artificial seed materials, in *Ind. Cryst.* **84**, S.J. Jančić and E.J. de Jong (Ed.), Elsevier, Amsterdam, 1984.
18. Kemenade van, M.J.J.M. and de Bruyn, P.L. A kinetic study of precipitation from supersaturated calcium phosphate solutions, *J. Colloid Interface Sci.* **118**(2), p.564-85, 1987.
19. Kibalczyk et. al. The effect of magnesium ions on the precipitation of calcium phosphates, *J. Cryst. Growth* **106**(2-3), p.355-366, 1990.
20. Lundager Madsen, H.E., Lopez Valero, I., Lopez Acevedo, V. and Boistelle, R., The formation product of amorphous tricalcium phosphate at 37°, *J. Crystal Growth* **75**(3), p.429-34, 1986.
21. Meyer, J.L. Phase transformation in the spontaneous precipitation of calcium phosphate, *Croat. Chem. Acta* **56**(4), p.753-67, 1983.
22. Meyer, J.L. and Weatherall, C.C. Amorphous to crystalline calcium phosphate phase transformation at elevated pH, *J. Colloid and Interface Sci.* **89**(1), p.257-267, 1982.
23. Nancollas, G.H. et al., Calcium phosphates-speciation, solubility, and kinetic considerations, in: *Chemical Modelling in aqueous Systems*, Jenne E.A. (Ed.), A.C.S. Symp. Ser. no. 93, Am. Chem. Soc., 1979.
24. Nancollas, G.H. et al., Mineral phases of calcium phosphate, *Anat. Rec.* **224**(2), p.234-241, 1989.

25. Press, W.H. et al., *Numerical recipes. The art of scientific computing*, Cambridge Univ. Press, 1986.
26. Seckler, M.M., Bruinsma, O.S.L. and van Rosmalen, G.M., Crystallization of calcium and magnesium phosphates in a fluidized bed, *Proc. 3rd European Conf. Crystal Growth*, Budapest 5-11 May 1991, p. 932, A.Lörinczy (Ed.), Transtech Pub., 1991.
27. Seckler, M.M. et. al., Phosphate removal by means of a full scale pellet reactor, *11th Int. Symp. Ind. Cryst.*, 18-20 Sept, Garmisch-Partenkirchen, Germany, 1990.
28. Strates B.S., Newman, W.F. and Levinkas, G.J., The solubility of bone mineral. II Precipitation of near-neutral solutions of calcium and phosphate, *J. Phys. Chem.* **61**, p.279-282, 1957.
29. Termine, J.D. and Posner, A.S., Calcium phosphate formation in vitro. I. Factors affecting initial phase separation, *Arch. Biochem. Biophys.* **140**, p.307-317, 1970.
30. Ting-Po, I. and Nancollas, G.H., EQUIL- A general computational method for the calculation of solution equilibria, *Anal. Chem.* **44**(12), p.1940-1950, 1972.
31. Tropp, J., Blumenthal, N.C. and Waugh, J.S., Phosphorus NMR study of solid amorphous calcium phosphate, *J. Am. Chem. Soc.* **105**, p.22-26, 1983
32. Walton, A.G. et. al., Nucleation of calcium phosphate from solution, *Canadian J. Chem.*, **45**, p.2696-2701, 1967.

CHAPTER 3

IDENTIFICATION OF PHYSICAL PROCESSES IN A FLUIDIZED BED FOR PHOSPHATE REMOVAL

Abstract

The main processes concerning the precipitation of calcium phosphate in a fluidized bed were studied. Primary nucleation and molecular growth occur at the bottom of the bed, where the incoming phosphate is mixed with the reactants, producing fine particles which partly aggregate with the grains of the bed and further leave the reactor with the liquid effluent. This aggregation seems to be the most important process for phosphate removal, while molecular growth of the grains seems to be of secondary importance.

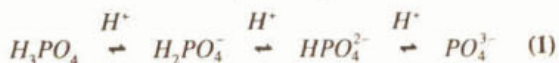
3.1 Introduction

Fluidized beds are often used for the crystallization of coarse products with a narrow particle size distribution, since classification of solids in the bed permits removal of crystals with a pre-specified size [4]. Recently fluidized beds have also been used for the separation of several sparingly soluble compounds from water. Processes for removal of calcium ions from drinking water (water softening) and of environmentally hazardous species such as heavy metals from wastewaters have been developed to full scale. One industrial scale plant for phosphate removal from domestic wastewater has also been built, based on the precipitation of calcium phosphates [6]. In the latter case overall phosphate removal efficiencies of about 90% could be obtained by applying recirculation and filtration of the treated water. The single pass reactor efficiency however, was only 50%. In order to omit the filtration step and to reduce the recirculation, higher single pass phosphate removal efficiencies have to be reached. Experiments in a bench scale plant under widely varied operating conditions (Chapter 2 and [5]) as well as optimized pilot plant experiments have not succeeded to provide higher efficiencies. In order to improve this figure, a better understanding of the fundamentals of the process is needed. In this paper the main processes concerning the precipitation of calcium phosphate in a fluidized bed and their time-scales were

experimentally studied by identifying the local phenomena in the bed. Fluidization characteristics of the system such as local voidage and segregation were not considered here. They will be studied in Chapter 5.

3.2 Process description

The process is based on the precipitation of calcium phosphate by mixing the phosphate containing wastewater with a source of calcium ions and a base. The base provides a shift to the right in the chemical equilibria given in equation (1), thereby increasing the supersaturation. The supersaturation with respect to amorphous calcium phosphate (ACP), $\text{Ca}_3(\text{PO}_4)_2$, is defined as shown in equation (2).



$$\beta = \frac{1}{5} \cdot \ln \frac{(\text{Ca}^{2+})^3 \cdot (\text{PO}_4^{3-})^2}{K_{\text{ACP}}} \quad (2)$$

The brackets indicate ion activities. The activities of the water molecules are assumed to be constant. K_{ACP} is the solubility product of ACP.

A schematic view of the fluidized bed is shown in Figure 1. The phosphate solution (influent), the calcium source and the base are added continuously at the reactor bottom. Calcium phosphate deposits upon the surface of sand grains. The phosphate covered grains are removed at the bottom of the bed and replaced intermittently by fresh sand grains. Simultaneously to the precipitation upon the sand grains, small calcium phosphate particles (fines) are generated in the reactor. This fines stream partly leaves the bed at the top and forms, together with the remaining dissolved phosphate stream, the percentage of phosphate which is not recovered by the fluidized bed. Part of these fine particles aggregate with the sand grains on their way up in the bed and thus contribute to the P removal efficiency.

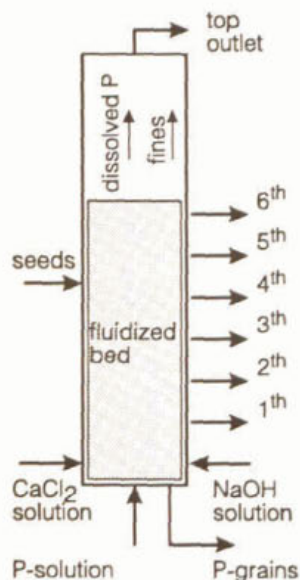


Figure 1. Schematic representation of a fluidized bed for calcium phosphate precipitation. The multiple outlets are used for the measurement of local properties.

The phosphate streams leaving the reactor are conveniently quantified in terms of the ratio between the phosphate flow rate in a given stream (in kg P/s) and the flow rate entering the reactor. The dimensionless fines fraction (X_f), efficiency (η) and conversion (X) are then defined as:

$$X_f = \frac{W_{P,fines}}{W_{P,infl}} ; \quad \eta = \frac{W_{P,grains}}{W_{P,infl}} ; \quad X = \frac{W_{P,fines} + W_{P,grains}}{W_{P,infl}} \quad (3)$$

$$X_f + \eta = X \quad (4)$$

The axial position in the reactor (H) can be related to the residence time (τ), i.e. the time needed for the liquid phase and the fines to travel from the bottom of the reactor to that particular axial position. It is assumed that the liquid moves upwards as a plug flow and that the fines in solution move with the same velocity as the liquid, so that the following relation holds,

$$\tau = H \cdot \epsilon / v_{sup} \quad (5)$$

where v_{sup} is the superficial velocity in the fluidized bed and ϵ is the bed porosity.

3.3 Experimental procedure

Continuous experiments in a fluidized bed (Figure 1) were performed in which the phosphate dimensionless values of X_f , η and X at various reactor heights were determined. Experiments in a plug flow reactor, which was simply the column of Figure 1 to which no sand grains were added, were also performed. In this way the precipitation of fines could be studied independently from the processes occurring in the presence of the grains.

The reactor had a diameter of 0.05 m and a height of 2.1 m and was provided with 6 outlets at various heights. The bottom of the reactor was provided with three nozzles for the inlets of a phosphate solution (influent), a calcium and a NaOH solution (base), respectively. A run

started with the 6th (upper) outlet open, the reactor being filled with a bed of bare sand. After a start-up period of 24 h to allow the deposition of a mineral layer upon the sand grains surface, the reactor effluent was sampled for analysis as described below. After that the 5th outlet was opened. The bed became then a little shorter than before and the sampling procedure was repeated. In this way the profiles along the reactor length of all the relevant variables could be measured. The process conditions are summarized in Table I.

Table I. Process conditions in the fluidized bed.

- inlet phosphate concentration:	$1.6 \cdot 10^{-3}$	$\text{kmol} \cdot \text{m}^{-3}$
- inlet Ca/P molar ratio:	3.0	-
- pH at the reactor outlet:	7.2	-
- superficial velocity:	$1.1 \cdot 10^{-2}$	$\text{m} \cdot \text{s}^{-1}$
- sand grains type:	SiO_2	-
- sand diameter:	$3.85 \cdot 10^{-4}$	m
- initial bed height in fluidization:	0.37	m
- average bed porosity:	0.76	-

The concentrations and flow rates of the streams entering and leaving the reactor were measured. For the latter stream 'total' and 'filtered' samples were taken. For the 'total' samples, the total flow was poured by gravity into the sampling recipient, thus avoiding segregation of fines during sampling. The 'filtered' portion was collected by suctioning with a syringe provided with a filter ($0.45 \mu\text{m}$), thus reducing the filtering time to a minimum. Both the total and the filtered samples were analyzed for the calcium, phosphate and sodium concentrations by inductively coupled plasma - atomic emission spectroscopy (Spectro). The concentrations of these ions in the fines stream was calculated as the differences between the 'total' and 'filtered' samples. The particle size distribution of the fines was measured on-line using a laser diffraction technique (Coulter LS 130).

The grains and fines removed from the reactor were air-dried for at least 48 h. The grains were subsequently weighed, so the bed porosity could be calculated. Grains and fines had their calcium and phosphate contents determined and were analyzed by X-ray diffraction.

Chemical grade reagents and demineralized water (conductivity lower than $1 \mu\text{S/cm}$) were used. The influent was a H_3PO_4 solution with the pH adjusted to 5 with NaOH. Calcium and

base reagent solutions were prepared with $\text{CaCl}_2 \cdot 6\text{H}_2\text{O}$ and NaOH , respectively.

The plug flow reactor was the same as described above, but no sand was added. The experimental procedure and process conditions were the same as before.

3.4 Results

Figure 2 shows the various dimensionless phosphate streams defined by eq. (3) as a function of the residence time in the fluidized bed. The conversion (X) increased abruptly in the first 20 s (which corresponds to a bed height of 0.3 m) and changed little afterwards. Most of the converted phosphate

was present as fines near the fluidized bed bottom, as shown by the X_f curve. Most of these fines disappeared as they travelled upwards together with the liquid phase, and the phosphate in the grains (η) increased accordingly (see eq. (4)). Near the

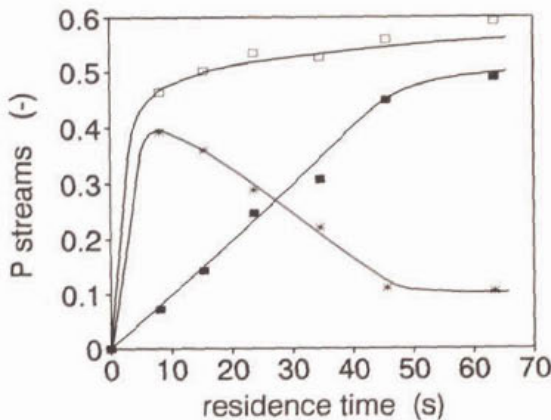


Figure 2. Dimensionless phosphate streams in the fluidized bed as a function of the residence time. □ = conversion (X), * = fines flow (X_f), ■ = efficiency (η).

fluidized bed outlet the system approached equilibrium, since all three phosphate streams were about constant.

Figure 3 shows the particle size distribution (PSD) of the fines in the fluidized bed, expressed as number percentage, at several residence times. The PSD expressed as volume percentage (not shown) varied with residence time in a similar way. The number averaged size increased

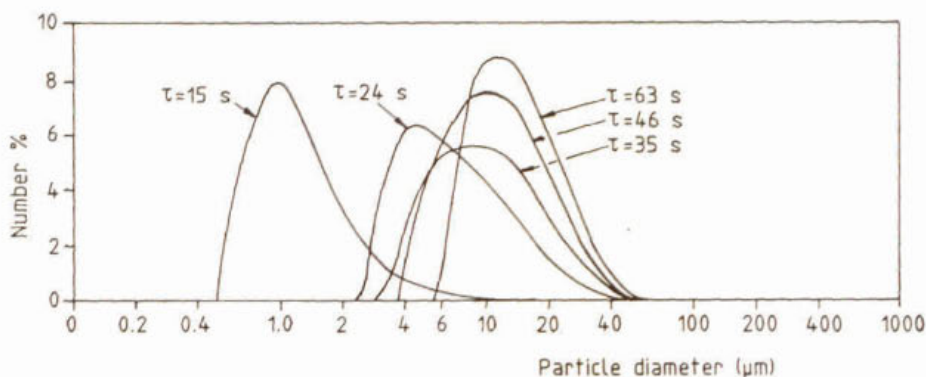


Figure 3. Particle size distribution of the fines in the fluidized bed at various residence times.

from 1 μm to 20 μm within 60 s. This matches with an average linear growth rate of 3×10^{-7} m/s.

In the absence of sand grains (plug flow reactor), the phosphate conversion varied with the residence time as shown in

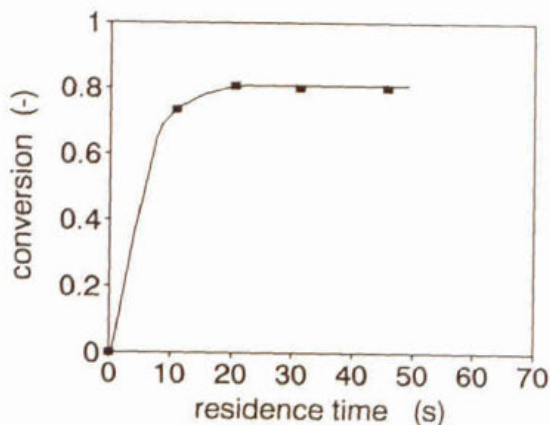


Figure 4. Conversion in the plug flow reactor as a function of the residence time.

Figure 4. Phosphate conversion into a solid phase increased abruptly in the first 20 s (corresponding to a bed height of 0.2 m) and remained constant afterwards.

The PSD of the fines in the plug flow reactor at several residence times is shown in Figure 5 and indeed remained almost constant along the reactor. A number average diameter of 5 μm was obtained at a residence time of 10 s or less, thus corresponding with an apparent

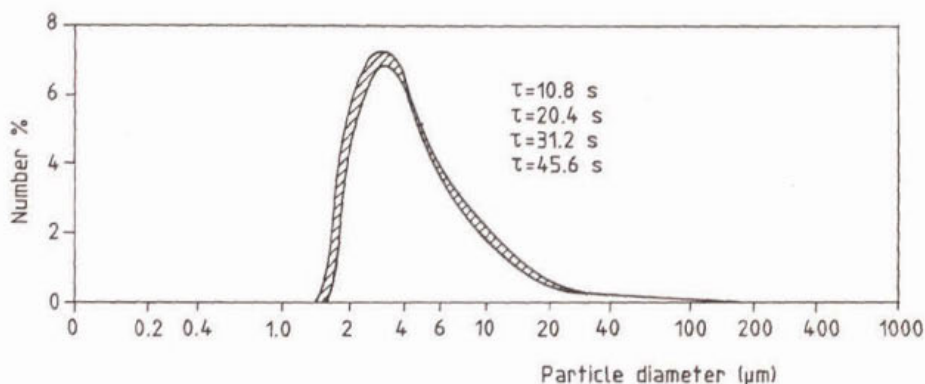


Figure 5. Particle size distribution of fines in the plug flow reactor. The curves for the indicated residence times fall within the hatched area.

growth rate of 5×10^{-7} m/s or more.

The grains and the fines from the fluidized bed as well as from the plug flow reactor were identified by X-ray diffraction analysis as a low crystallinity tricalcium phosphate, with chemical formula $\text{Ca}_3(\text{PO}_4)_2$. Chemical analysis gave a Ca/P molar ratio of 1.52 ± 0.05 , consistent with the chemical formula.

3.5 Discussion

In the previous section it was shown how the phosphate ions entering the fluidized bed were distributed between the three dimensionless streams, fines, grains and soluble phosphate, characterized respectively by X_f , η and $1-X$. Furthermore, changes in the fines PSD with time were shown. The potential mechanisms for the changes in the stream values are discussed below.

3.5.1 Primary nucleation and molecular growth

Primary nucleation and molecular growth of fines and grains are supposed to be responsible for the conversion of phosphate from the liquid to the solid phase. Figures 2 and 4 show that

the conversion in both the plug flow reactor and the fluidized bed, and thus the primary nucleation and molecular growth, were fast processes that were completed within 20 s. In the rest of the plug flow reactor and of the fluidized bed ($\tau > 20$ s) primary nucleation and molecular growth hardly occurred, since the conversion varied little.

Primary nucleation and molecular growth of calcium phosphate only occur when the reactants (calcium ions, phosphate ions and base) are mixed on a molecular scale. Since these processes are fast, it is likely that their kinetics are influenced by mixing conditions and so are precipitate characteristics such as crystallinity, particle size distribution, impurity uptake, etc. A better understanding of the influence of mixing on the precipitate characteristics is therefore needed and will be studied in Chapter 6.

3.5.2 Aggregation

The apparent growth rate of the fines in the plug flow reactor was estimated from the measured PSD and from the fines residence time in the reactor. An apparent growth rate of $5 \times 10^{-7} \mu\text{m/s}$ was obtained, a value which seems too large to be caused by molecular growth only. Therefore subsequent fines-fines aggregation is most likely to happen. The tendency towards aggregation during calcium phosphate precipitation has been earlier reported in the literature [1,2,3].

In the fluidized bed, the measured changes in PSD of the fines with time could result from two types of aggregation, fines-grains and fines-fines.

Aggregation of grains-fines is also consistent with the observed disappearance of fines as they traveled upwards in the fluidized bed (see X_f in Figure 2). From Figure 2 it can be estimated that this disappearance corresponds with at least $\sim 2/3$ of the phosphate removed by the fluidized bed. The remaining $1/3$ was removed either by aggregation or by molecular growth. Aggregation of fines-grains thus plays an important role in the phosphate removal efficiency. A better understanding of the aggregation process may therefore lead to an improvement of the phosphate removal efficiency in the fluidized bed. The aggregation process will be studied in Chapters 4 and 7.

3.5.3 Abrasion

Abrasion of the grains in the fluidized bed, which results in fines generation at the cost of a loss in the recovered phosphate, cannot be excluded. Far from the fluidized bed inlet (at $\tau > 10$ s) the values of η and X_r result from a competition between aggregation of fines-grains which causes η to increase and abrasion which causes η to decrease. The aggregation process dominates, since η increases with τ in Figure 2. Near the fluidized bed inlet ($\tau < 10$ s) the same competition holds, but primary nucleation and growth of fines and grains do occur there as well. Abrasion is expected to be specially important near the inlet nozzles, where energy dissipation is the highest.

3.6 Conclusions

The main processes concerning the precipitation of calcium phosphate in a fluidized bed were established. Fines are produced by primary nucleation and molecular growth at the reactor bottom. Aggregation among the fines occurs rapidly, particles of $5\ \mu\text{m}$ being formed within 10 s or less. The fines also aggregate with the grains as they travel upwards in the reactor, this process being completed within 50 s. The liquid phase approaches equilibrium within 20 s, the corresponding reactor height being 0.3 m. Molecular growth upon the grains is a secondary process with respect to the phosphate removal.

Since the primary nucleation, molecular growth and aggregation of calcium phosphate are all fast processes, it is likely that they are influenced by mixing conditions. The influence of mixing upon these processes and thus upon precipitate characteristics such as size distribution will be studied in Chapter 6. Since the phosphate removal in the fluidized bed largely depends on aggregation, this process will be further studied in Chapters 4 and 7. Local fluidization characteristics will be considered in Chapter 5.

References

1. Feenstra, T.P. and de Bruyn, P.L., Light scattering studies on solutions containing calcium phosphates, *J. Colloid Interf. Sci.* **73**, p.431-437, 1980.
2. Fueredi-Milhofer, H. et al., Crystal growth and phase transformation in the precipitation of calcium phosphates, *Faraday Discuss. Chem. Soc.* **61**(Precipitation), p.184-93, 1976.
3. Melikhov, I.V. et al., The effect of dissolved impurity on calcium phosphate nucleation in supersaturated medium, *J. Colloid Interf. Sci.* **127**(2), p.317-27, 1989.
4. Nývlt, J. *Industrial Crystallization. The state of the art*, Weinheim, Basel: Verlag Chemie, 1982.
5. Seckler, M.M., Bruinsma, O.S.L. and van Rosmalen, G.M., Crystallization of calcium and magnesium phosphates in a fluidized bed. *3rd Europ. Conf. Cryst. Growth*, May 5-11, 1991, Budapest, Hungary.
6. Seckler, M.M. et al., Phosphate removal from waste water by means of a full scale pellet reactor, *11th Int. Symp. Industrial Crystallization*, Sept. 18-20, 1990, Garmisch-Partenkirchen, Fed. Rep. Germany.

CHAPTER 4

KINETICS OF NUCLEATION, AGGREGATION AND BREAKAGE OF CALCIUM PHOSPHATE

Abstract

Calcium phosphate precipitation from a clear solution was studied in continuous and batchwise set-ups. An amorphous modification (ACP) was formed first and recrystallized into hydroxyapatite. ACP formation was completed within 0.5 s or less, and consisted of nucleation by a homogeneous mechanism, molecular growth, aggregation and breakage. After this period, nucleation and molecular growth became negligible, but the particle size distribution was further modified by aggregation and breakage up to precipitation times of 30 s. The kinetics of nucleation were estimated and those of aggregation and breakage were described by means of a mathematical model based on the moments of the particle size distribution. The aggregation rate decreased with the pH and increased with the particle size. The breakage rate increased with the energy dissipation rate.

4.1 Introduction

In Chapter 3 the basic processes occurring in a fluidized bed for phosphate removal were identified. It was found that primary particles of amorphous calcium phosphate (ACP) precipitate at the bottom of the reactor and subsequently aggregate with the grains in the fluidized bed, thus contributing to the phosphate removal. If optimization of the phosphate removal is to be achieved, the formation of primary particles of ACP must be well understood.

Much has been published on the structure of amorphous calcium phosphate as well as on the kinetics of its transformation to more stable calcium phosphate modifications. However, there is a lack of information on the kinetics of ACP precipitation within the timescales of interest in a fluidized bed for phosphate removal. In this chapter the mechanisms and the kinetics of the elementary processes during ACP precipitation from clear solutions were thus studied.

The elementary processes considered were nucleation, molecular growth, aggregation and breakage.

Batchwise experiments were performed to study ACP precipitation for residence times equal to or larger than the residence time in a fluidized bed for phosphate removal (~ 200 s). Furthermore continuous experiments were applied to study the precipitation for residence times as low as 0.5 s. The experimental set-up for the continuous experiments consisted of a non-seeded mixed suspension, mixed product removal reactor (MSMPR) placed upstream of a plug flow reactor (PFR). In the MSMPR primary nucleation, growth, aggregation and breakage of the particles take place. In the PFR, nucleation and growth are negligible, so that aggregation and breakage are isolated and can be more easily studied. A simple mathematical model for the kinetics of aggregation and breakage in a PFR was developed.

4.2 Mathematical model for aggregation and breakage in a plug flow reactor (PFR)

When calcium phosphate is allowed to precipitate in a mixed suspension, mixed product removal reactor (MSMPR) placed upstream of a plug flow reactor (PFR), in the MSMPR four elementary processes take place simultaneously but in the PFR only aggregation and breakage proceed. In this section a mathematical model is presented for aggregation and breakage in a PFR. The MSMPR is not modelled, but is merely considered as a source of freshly formed particles that are fed to the PFR. The mathematical model is based on the moment transformation of the population balance (section 4.2.1) coupled to the kinetics of aggregation (section 4.2.2) and breakage (section 4.2.3). A model summary is presented in section 4.2.4.

4.2.1 Population balance

A plug flow reactor at steady state is considered, fed with calcium phosphate particles freshly formed in an MSMPR. The residual supersaturation in the MSMPR is low. The particles in the PFR thus undergo aggregation and breakage, but no further nucleation or growth. The population balance and the respective boundary condition are given by

$$\frac{\partial n(t,L)}{\partial t} = + B_{ag}(t,L) - D_{ag}(t,L) + B_{br}(t,L) - D_{br}(t,L) \quad (1)$$

$$n(t_0,L) = n_0(L)$$

where t represents the precipitation time (t_0 at the inlet), L the particle size, n the population density, B and D the birth and death functions for the aggregation and breakage. The difference $B_{ag} - D_{ag}$ represents the aggregation function and $B_{br} - D_{br}$ the breakage function. The precipitation time is calculated from the superficial velocity (v_{sup}) and the axial position in the PFR (x) as

$$t = x / v_{sup} \quad (2)$$

The moment transformation of eq.(1) is obtained by multiplying all of its terms by $L^p dL$ and integrating from 0 to ∞ (Randolph and Larson, [17]):

$$\frac{\partial m_p(t)}{\partial t} = + \overline{B_{ag,p}}(t) - \overline{D_{ag,p}}(t) + \overline{B_{br,p}}(t) - \overline{D_{br,p}}(t) \quad (3)$$

$$m_p(t_0) = m_{p,0} \quad p=0,1,2,\dots$$

$$m_p(t) = \int_0^\infty L^p n(t,L) dL \quad (4)$$

$$\begin{aligned} \overline{B_{ag,p}}(t) &= \int_0^\infty L^p B_{ag}(t,L) dL \\ \overline{D_{ag,p}}(t) &= \int_0^\infty L^p D_{ag}(t,L) dL \\ \overline{B_{br,p}}(t) &= \int_0^\infty L^p B_{br}(t,L) dL \\ \overline{D_{br,p}}(t) &= \int_0^\infty L^p D_{br}(t,L) dL \end{aligned} \quad (5)$$

The p^{th} moment of the distribution $m_p(t)$ is defined by eq.(4). The term $\overline{B_{ag,p}} - \overline{D_{ag,p}}$ represents the rate of change of the p^{th} moment of the particle size distribution (PSD) due to aggregation. Similarly, $\overline{B_{br,p}} - \overline{D_{br,p}}$ represents the rate of change of the p^{th} moment of the PSD due to breakage. Through the moment transformation, the population balance, which is a single equation with two independent variables (t, L), is substituted by a set of p equations with only one independent variable (t).

The particular forms of the birth and death functions $B_{ag}, D_{ag}, B_{br}, D_{br}$ (which after the moment transformation give the functions $\overline{B_{ag}}, \overline{D_{ag}}, \overline{B_{br}}, \overline{D_{br}}$), depend on the specific aggregation and disruption models chosen. These models are presented below.

4.2.2 Aggregation

Hulburt and Katz [8] proposed a population balance model for aggregation assuming: (i) two body aggregation; (ii) volume conservation, i.e. the volume of 2 particles before and after aggregation does not change; (iii) constant volumetric shape factor; (iv) the frequency of successful collisions between the particles of volumes v and v' is proportional to the product of their population densities - a successful collision is one which effectively leads to an aggregate; (v) the proportionality factor k_{ag} (aggregation kernel) is size independent. Unfortunately the method only gives a solution for the $0^{th}, 3^{rd}, \dots, (n+3)^{th}$ moment of the distribution. For the 0^{th} and 3^{rd} moments they give

$$\overline{B_{ag,0}}(t) - \overline{D_{ag,0}}(t) = -\frac{1}{2} k_{ag} m_0(t)^2 \quad (6)$$

$$\overline{B_{ag,3}}(t) - \overline{D_{ag,3}}(t) = 0 \quad (7)$$

Since the 3^{rd} moment represents the total volume of the particles, eq. (7) is consistent with the hypothesis of volume conservation.

In order to obtain equations similar to eqs.(6) and (7) for all the moments ($0^{th}, 1^{st}, 2^{nd}, \dots$), we refer to Hounslow and co-workers [7]. They considered aggregation with a size

independent kernel in a batch system. The initial PSD was assumed to be represented by the following exponential function:

$$n(t-t_0, L) = \frac{N_0}{v_0} \exp\left(-\frac{k_v L^3}{v_0}\right) \quad (8)$$

where N_0 and v_0 are arbitrary constants. They solved the population balance for a batch system without breakage and derived the following expression for the moments of the distribution as a function of time:

$$m_p(t) = m_p(t_0) \left(\frac{2}{N_0 k_{ag} t + 2}\right)^{1-p/3} \quad (9)$$

Differentiation of this equation with respect to time provides the wanted aggregation rates in a plug flow reactor:

$$\overline{B_{ag,p}}(t) = \overline{D_{ag,p}}(t) = -\frac{1}{2} (1 - p/3) k_{ag} m_0(t) m_p(t) \quad (10)$$

$p=0,1,2,\dots$

The aggregation rates for the 0th and 3rd moments coincide with eqs.(6) and (7), as expected. An implicit assumption in eq. (10) is that no process other than aggregation takes place.

4.2.3 Breakage

Randolph [16] proposed a two-body breakage model which assumes that the death function of a particle with size L is proportional to its population density and to the power s of the particle size:

$$D_{br}(t, L) = k_{br} n(t, L) L^s \quad (11)$$

Here a value of 1 is assumed for s . The breakage death function assumes a negligible value for very small particles. Further assuming equal-volume breakage, a relation between the death and birth functions can be derived

$$B_{br}(t,L) \cdot dL \cdot dt = 2 \cdot D_{br}(t,cL) \cdot d(cL) \cdot dt \quad (12)$$

$$B_{br}(t,L) = 2 \cdot c \cdot D_{br}(t,cL) \quad (13)$$

By assuming that the particle volume is conserved in the disruption process, the value of c in eq. (13) is $2^{1/3}$. The moment transformation of eq.(11) and (13) is derived as

$$\overline{B_{br,p}}(t) = \int_0^\infty L^p \cdot 2c \cdot D_{br}(t,cL) \cdot dL \quad (14)$$

$$\overline{D_{br,p}}(t) = \int_0^\infty L^p \cdot D_{br}(t,L) \cdot dL \quad (15)$$

Subtracting eq. (15) from eq. (14) and using eq. (11), the breakage rate is obtained. For $c = 2^{1/3}$ and $s = 1$,

$$\overline{B_{br,p}} - \overline{D_{br,p}} = (2^{1-p/3} - 1) k_{br} m_{p+1}, \quad p=0,1,2,\dots \quad (16)$$

When $p=3$ the right hand side of eq.(16) vanishes, so the 3rd moment of the PSD remains constant during breakage, consistent with the hypothesis of volume conservation. Equation (16) must be solved for a finite number of moments, i.e. this equation must be truncated in the p^{th} moment of the PSD. In order to solve eq. (16) for the p^{th} moment, information about the $(p+1)^{\text{th}}$ moment is required. Therefore, an additional closure equation relating moments of different orders is needed. Hulburt and Katz [8] presented such a relation for PSD's that can be represented by a Laguerre series. However, if eq. (16) is truncated in the 3rd moment, the use of this equation can be avoided since m_3 is just the volume fraction of solids and is thus a known constant (independent of m_{3+i}).

4.2.4 Model summary

The mathematical model for aggregation and breakage in a PFR is obtained by combining eqs. (3),(10) and (16):

$$\begin{aligned} \frac{\partial m_p(t)}{\partial t} = & - \frac{1}{2} (1 - p/3) k_{ag} m_0(t) m_p(t) + \\ & + (2^{1-p/3} - 1) k_{br} m_{p+1} \\ m_p(t_0) = & m_{p,0}, \quad p=0,1,2,3 \end{aligned} \quad (17)$$

The model assumptions can be summarized as: steady state; ideal plug flow; negligible growth and nucleation; arbitrary PSD (solution for 0th and 3rd moments only) or exponential PSD (solution for 0th, 1st, 2nd and 3rd moments); volume conserving, two-body, size independent aggregation; volume conserving breakage; breakage into two equally sized fragments; breakage rate proportional to the particle size.

The model inputs are the moments of the PSD at the PFR inlet (boundary conditions), whereas the moments of the distribution as functions of time are its outputs. The aggregation and breakage kernels, k_{ag} and k_{br} are the adjustable model parameters.

4.3 Experimental

4.3.1 Batch experiments

The reagents used were chemical grade $\text{CaCl}_2 \cdot 6\text{H}_2\text{O}$, H_3PO_4 , NaOH and demineralized water with a conductivity lower than $1 \mu\text{S/cm}$. An aqueous solution of H_3PO_4 having its pH adjusted to 8 with NaOH (P solution) was allowed to reach thermal equilibrium ($25 \pm 0.1^\circ\text{C}$) in a 1.6 l jacketed glass reactor. At the start of the experiment 0.025 l of a calcium chloride solution (Ca solution) was pipetted into the reactor. The compositions, volumes and pH of the P solution, Ca solution as well as of their mixture are given in Table I. Both solutions had been passed through $0.22 \mu\text{m}$ filters to remove dirt particles which otherwise would act as heterogenous nuclei. A centrifugal pump provided the mixing of reactants through external recirculation of the vessel contents. Both unfiltered and filtered ($0.45 \mu\text{m}$) samples were

taken regularly from the reactor and analyzed for the concentrations of the elements sodium, phosphorus and calcium by inductively coupled plasma - atomic emission spectroscopy (Spectro). The particles were analyzed under a transmission electron microscope (TEM). The pH was continuously recorded.

Table I Process conditions of the batch experiments. ⁽¹⁾ after precipitation

Solution	pH (-)	Volume (l)	Conc. P (kmol·m ⁻³)	Conc. Ca (kmol·m ⁻³)
P solution	8	1.5	$1.52 \cdot 10^{-3}$	-
Ca solution	7	0.025	-	0.273
Mixture	7.25 ⁽¹⁾	1.525	$1.50 \cdot 10^{-3}$	$4.48 \cdot 10^{-3}$

4.3.2 Continuous experiments

The experimental set-up consisted mainly of a mixed suspension, mixed product removal reactor (MSMPR) which outlet was connected directly to the inlet of a plug flow reactor (PFR), as schematically shown in Figure 1. The MSMPR was a perspex cylindrical recipient with a diameter of 0.025 m, a height of 0.020 m, a useful volume of 0.004 l, provided with a propeller-type glass impeller (160 - 2000 rpm) with a diameter of 0.023 m. The PFR consisted of a PVC tube with an internal diameter of $6 \cdot 10^{-3}$ m and a variable length (0.2 to 20 m).

The reagents used were chemical grade $\text{CaCl}_2 \cdot 6\text{H}_2\text{O}$, H_3PO_4 , NaOH and demineralized water with a conductivity lower than 1 $\mu\text{S}/\text{cm}$. Calcium phosphate precipitation was performed continuously by feeding an undersaturated solution containing the ions Ca^{2+} and PO_4^{3-} , a sodium hydroxide solution as well as a dilution water stream into the MSMPR. The flow rates and concentrations of the streams entering the MSMPR for all experiments were such that the phosphate and calcium concentrations after mixing of reactants were $1.6 \cdot 10^{-3}$ kmol·m⁻³ and $4.8 \cdot 10^{-3}$ kmol·m⁻³. The flow rates and concentrations for a typical experiment (exp. nr. N0160) are shown in Table II. In some experiments (see below) the flow rate of the sodium hydroxide solution or the total flow rate was adjusted to give the desired pH or

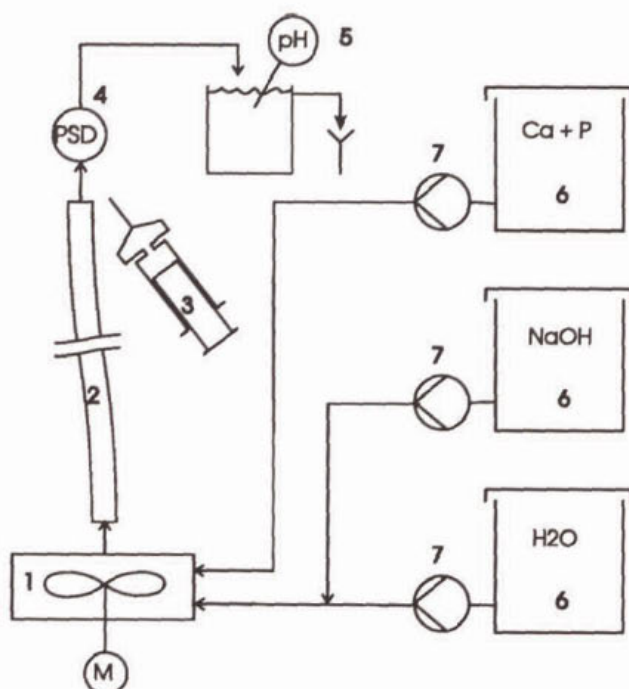


Figure 1. Experimental set-up: MSMPR (1), PFR (2), filter for sampling (3), PSD meter (4), pH meter (5), storage vessels (6) and peristaltic pumps (7).

energy dissipation rate in the PFR, respectively.

The flow rates and concentrations of all streams entering and leaving the reactor were measured. Unfiltered and filtered samples were regularly taken from the MSMPR outlet as well as from the PFR outlet. Unfiltered samples were collected by pouring the total flow into a sampling recipient whereas filtered samples were collected by placing a $0.45\ \mu\text{m}$ filter in a syringe and suctioning directly from the outlet stream. This filtering procedure led to filtration times as low as 0.3 s. The concentrations of the elements sodium, phosphate and calcium were measured by inductively coupled plasma - atomic emission spectroscopy (Spectro). The carbonate concentration in the NaOH solution storage vessel was also measured (acid-base titration) to assure that the total carbonate level in the reaction medium was below $0.2 \cdot 10^{-3}\ \text{kmol} \cdot \text{m}^{-3}$. The particle size distribution (PSD) of the product was measured in line with a laser diffraction technique (Coulter LS-130). Particle sizes between

0.1 and 800 μm could be measured in this way. The residence time of the suspension in the PSD meter was 1.6 s (calculated for a superficial velocity of 0.667 m/s in the PFR, which corresponds to an energy dissipation rate of $1.0 \text{ W}\cdot\text{kg}^{-1}$ in the PFR calculated as shown in section 4.4.7). The pH at the PFR outlet was recorded continuously. The particles were analyzed under a transmission electron microscope (TEM). The samples were prepared by placing droplets of the suspension upon carbon coated grids and removing the excess water with a tissue paper. The samples were then air-dried and placed in the TEM.

Table II Process conditions for the continuous experiment N0160.

Solution	Flow rate ($\text{m}^3\cdot\text{s}^{-1}\cdot 10^6$)	Concentration		
		P ($\text{kmol}\cdot\text{m}^{-3}$)	Ca ($\text{kmol}\cdot\text{m}^{-3}$)	Na ($\text{kmol}\cdot\text{m}^{-3}$)
Ca, P solution	9.3	$3.2\cdot 10^{-3}$	$9.6\cdot 10^{-3}$	-
NaOH solution	0.2	-	-	0.26
water	9.1	-	-	-
mixture	18.6	$1.6\cdot 10^{-3}$	$4.8\cdot 10^{-3}$	$3.0\cdot 10^{-3}$

The impeller rotation speed in the MSMPR, the total flow rate (expressed as the energy dissipation rate in the PFR), the NaOH flow rate (expressed as the outlet pH) and the precipitation time were varied as shown in Table III. The precipitation time was varied by changing the length of the PFR.

4.4 Definitions and preliminary calculations

4.4.1 Precipitation time

At the inlet of the MSMPR the precipitation time was arbitrarily chosen as $t=0$. The total precipitation time (t) is defined as the sum of the residence times in the MSMPR (0.2 s), in the PFR (variable) and in the measuring device. The latter was either the filter (0.3 s) or the PSD meter (1.6 s). The time intervals just mentioned refer to a superficial velocity of 0.667 m/s in the PFR (with a corresponding energy dissipation rate of $1.0 \text{ W}\cdot\text{kg}^{-1}$ in the PFR

calculated as shown in section 4.4.7).

Table III. Experimental conditions for the MSM-PR-PFR system, kinetic parameters for aggregation and breakage in the PFR (k_{ag} and k_{br}) and time-volume-averaged sizes ($L_{4,3}$).

<i>exp.</i> <i>nr.</i>	N_{MSMPR} (rpm)	E_{PFR} (W· kg ⁻¹)	<i>pH</i> -	<i>t</i> (s)	k_{ag} (m ³ ·# ⁻¹ · s ⁻¹ ·10 ⁺¹¹)	k_{br} (#· m ⁻¹ ·s ⁻¹)	$L_{4,3}$ (m· ·10 ⁴)
N0160	160	1.0	7.8	2 to 30	9.1	4600	1.02
N0400	400	1.0	7.8	2 to 30	9.7	4300	1.04
N0750	750	1.0	7.8	2 to 30	22	4000	1.42
N1000	1000	1.0	7.8	2 to 30	20	4500	1.40
N2000	2000	1.0	7.8	2 to 30	23	5900	1.68
E1.0	750	1.0	7.8	2 to 30	20	4200	1.36
E1.8	750	1.8	7.8	2 to 30	8.1	7000	0.97
E2.9	750	2.9	7.8	2 to 30	2.0	8000	0.79
PH7.5	750	1.0	7.5	2 to 30	-	-	-
PH7.8	750	1.0	7.8	2 to 30	20	5000	1.55
PH8.0	750	1.0	8.0	2 to 30	12	5000	1.66
PH8.6	750	1.0	8.6	2 to 30	7.0	5000	1.65
PH10	750	1.0	10	2 to 30	-	-	-
CONV7.1	~ 400	1.0	7.1	0.2 to 20	-	-	-
CONV7.2	~ 400	1.0	7.2	0.2 to 20	-	-	-
CONV7.7	~ 400	1.0	7.7	0.2 to 20	-	-	-

4.4.2 Supersaturation

The supersaturation β is defined in terms of ion activities for the precipitation of ACP with a chemical formula $Ca_3(PO_4)_2$ and a solubility K_s :

$$\beta = \frac{1}{5} \ln \frac{(Ca^{2+})^3(PO_4^{3-})^2}{K_s} \quad (18)$$

The supersaturation was calculated from the measurements of the solution composition with the model for the equilibrium in the liquid phase presented in Chapter 2.

4.4.3 Types of particles

The term *primary particle* will be used for a particle formed exclusively by nucleation and molecular growth. The solid entity produced by subsequent aggregation of primary particles is simply called a *particle*.

4.4.4 Growth rate and average particle size

The growth rate (G) is defined as

$$G = dL/dt \quad (19)$$

where L is the particle size. For the growth rate of primary particles, $L_{primary}$ should be used instead of L . The average particle size $L_{i,j}$ is defined in terms of the moments of the PSD m_i and m_j as

$$L_{i,j} = (m_j/m_i)^{1/(i-j)} \quad (20)$$

where the values of i and j determine the type of average. The number-averaged particle size ($L_{1,0}$), the volume-averaged particle size ($L_{4,3}$) and the volume-number average size ($L_{3,0}$) were used in this work.

4.4.5 Conversion

The conversion (X) represents the fraction of phosphate entering the reactor that precipitates. It is defined as

$$X = \frac{c_{Pin} - c_{Pliq}}{c_{Pin}} \quad (21)$$

where c_{Pin} is the total phosphate concentration in the MSMR and c_{Pliq} is the dissolved phosphate concentration at the outlet of the PFR. The conversion is within the range 0 to 1 and depends on the amount of base added as well as on the precipitation time. The conversion is exclusively associated with the elementary processes nucleation and molecular

growth, that determine the phosphate consumption from the solution.

4.4.6 Moments of the PSD

The moments of the PSD were calculated from the volume based histogram $vol\%_i$ versus L_i (output of the PSD meter) and from the conversion by

$$m_p = \sum_i \frac{vol\%_i}{100} \cdot m_3 \cdot L_i^{p-3} \quad (22)$$

$$m_3 = \frac{mw_{ACP}}{\delta_P \cdot \rho_{ACP} \cdot k_v} \cdot X \cdot c_{Pin} \quad (23)$$

where i indicates the size sub-range. $k_v \cdot m_3$ is the volume fraction of particles, where each particle is an aggregate of primary particles. The number of P atoms in the ACP molecule δ_P is 2, the molecular weight of ACP mw_{ACP} is 310 $kg \cdot kmol^{-1}$. The density of the ACP particles ρ_{ACP} , which are aggregates containing entrapped water, is estimated to be 2000 $kg \cdot m^{-3}$ and the volume shape factor k_v , $\pi/6$.

Eq. (23) can also be used to calculate the volume fraction of primary particles $m_{3,primary}$, by substitution of ρ_{ACP} by $\rho_{ACP, primary}$. The latter can be taken as the density of tricalcium phosphate (3140 $kg \cdot m^{-3}$).

4.4.7 Energy dissipation rate

The energy dissipation rate E , also called mixing intensity, is defined as the power input per unit mass of fluid. For a PFR, E is directly related to the pressure drop (ΔP):

$$E = \frac{\Delta P \cdot v_{sup}}{L_R \cdot \rho_f} \quad (24)$$

Strictly, the actual fluid velocity ($v_{sup}/\text{porosity}$) should be used in the equation above, but for diluted suspensions the difference between the actual and the superficial velocity may be

neglected. The pressure drop for a PFR was calculated from the Fanning equation [15] with friction factors of 0.0097, 0.0091 and 0.0088 for the three superficial velocities used in the experiments (0.667, 0.83 and 1 m/s):

$$\Delta P = \frac{4 f L_R \rho_f}{D_R} \cdot \frac{v_{sup}^2}{2} \quad (25)$$

For an MSMPR, the energy dissipation rate was estimated from the following correlation for mixed vessels [15]:

$$E = N_p \frac{N^3 \cdot D_i^5}{V} \quad (26)$$

where N_p is the power number (dimensionless), which for propeller-type impellers assumes a value of 0.9 [15], N is the agitator rotation speed (s^{-1}), D_i the impeller diameter (m) and V the useful volume of the MSMPR (m^3).

4.5 Results and discussion

4.5.1 Batch experiments

Batch experiments were performed in order to study the ACP precipitation at timescales of the same order of magnitude and longer than those found in a fluidized bed for phosphate removal. The main features of the precipitation process as well as an estimate of the solubility of ACP are presented in this section.

4.5.1.1 Stages of calcium phosphate precipitation

Calcium phosphate formed in a batch reactor from solutions with Ca and P concentrations of $4.5 \cdot 10^{-3}$ and $1.5 \cdot 10^{-3} \text{ kmol} \cdot \text{m}^{-3}$ as well as a pH of 7.25 (measured after the first precipitation stage at a time of 15 s) was amorphous from x-ray as well as electron diffraction with a Ca/P molar ratio of 1.48 ± 0.03 , in agreement with earlier investigations [1,4,5,10,13,19,20,24]. The primary particles observed under a TEM were spheroids with

diameters of $2 \cdot 10^{-8}$ to $5 \cdot 10^{-8}$ m similar to those observed elsewhere [11,12], as shown in Figure 2. The particles appear as the dark areas in the figure and are strings of aggregated primary particles.

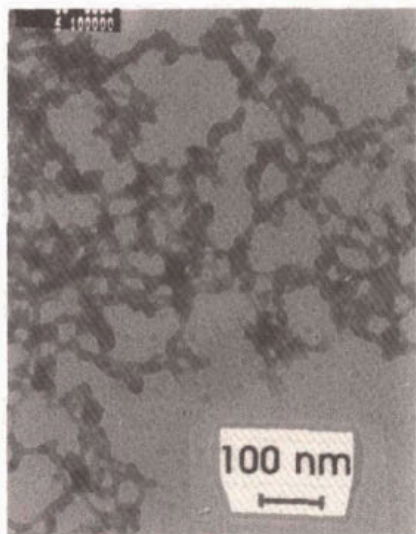
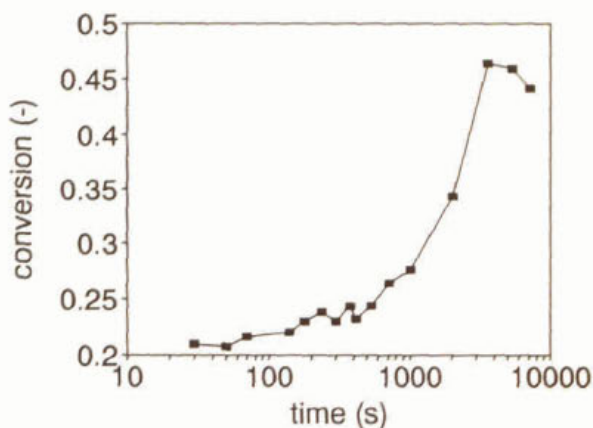


Figure 2. TEM view of ACP particles freshly precipitated in a batch reactor, pH 7.6. Dark areas are rings of aggregated primary ACP particles and light areas the background. The same morphology was found for particles from a plug flow reactor.

Amorphous calcium phosphate (ACP) is metastable and undergoes solvent mediated recrystallization into hydroxyapatite (HAP), which is the thermodynamically stable modification. The precipitation of ACP and its recrystallization were followed in a batch reactor by measuring the conversion, pH and Ca/P molar ratio of the particles with time as shown in Figure 3. Three main precipitation stages were identified. In the first stage most of the ACP precipitated as the conversion increased from 0 to 0.21 within 20 s or less. In the second stage the residual supersaturation with respect to ACP was consumed as the conversion increased gradually up to 0.23 at 300 s. In the third stage substantial HAP was formed as the conversion rapidly increased up to 0.45 at 3000 s.

The development of the pH followed the conversion: an increase in conversion was always accompanied by a decrease in pH. This decrease in pH was consistent with the chemical equilibrium of the solution: as PO_4^{3-} ions vanished from the solution due to precipitation, part of the hydrogenated phosphate ions or complexes (HPO_4^{2-} , CaHPO_4° , etc) dissociated to replenish the solution with PO_4^{3-} ions. In this process, H^+ ions were liberated to the solution, causing the observed decrease in pH.

The Ca/P of the particles increased, indicating that some recrystallization into HAP was already taking place after the early stages of precipitation. This increase in Ca/P ratio of the



(a)

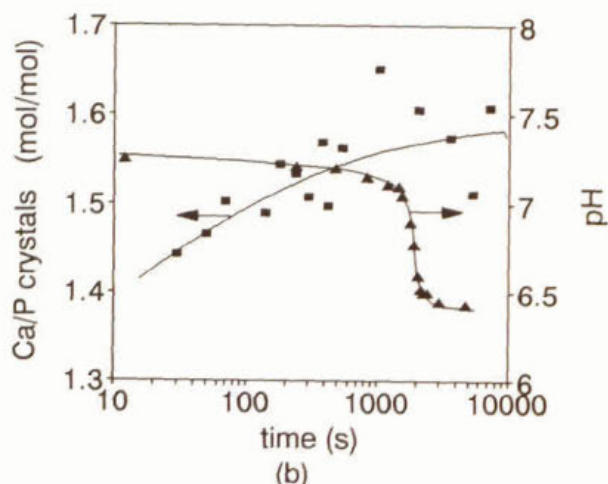


Figure 3. Conversion (a), solids Ca/P molar ratio (b, ■) and pH (b, ▲) as functions of time in the batch reactor. Total concentrations in $\text{mmole} \cdot \text{l}^{-1}$: $\text{P}=1.5$, $\text{Ca}=4.48$ and $\text{Na}=2.86$.

particles can also be attributed to the occurrence of structural changes in the ACP [3].

The Ca/P ratio of the particles after 7000 s was 1.60, smaller than the value of HAP (1.67). This value is consistent with that of a calcium deficient, poorly crystalline HAP, which is known to be formed upon recrystallization from ACP [2,12,13]. The Ca/P ratio and crystallinity of HAP further increase after longer periods as ripening of HAP proceeds [19] (not investigated).

4.5.1.2 Solubility product of ACP

Usually solubility measurements are made by allowing equilibration between the solid and the solution. This procedure cannot be applied to ACP, since this material recrystallizes into

HAP before equilibrium is reached. However, an estimate of the solubility of ACP may be made by assuming that ACP reached equilibrium just before substantial HAP precipitation started in the batch experiment, i.e. at 300 s in Figure 3. Since the conversion changed negligibly for times between 20 and 300 s (i.e. during the second stage of precipitation), the estimated solubility is likely to represent well the precipitation of ACP in this time range. Thus, from the solution composition at 300 s, the solubility product of ACP (assumed to

have the chemical formula $\text{Ca}_3(\text{PO}_4)_2$) was experimentally determined as $K_s = 3 \cdot 10^{-27} \text{ kmol}^5 \cdot \text{m}^{-15}$ (based on activities).

In order to validate the procedure above, K_s was used to predict the conversion in the MSMPR-PFR for several pH values and assuming equilibrium at the reactor outlet. The calculated conversion agreed reasonably well with the measured conversion for a precipitation time of 2 s, as can be seen in Figure 4. Besides, K_s was found to represent well the conversion in a fluidized bed

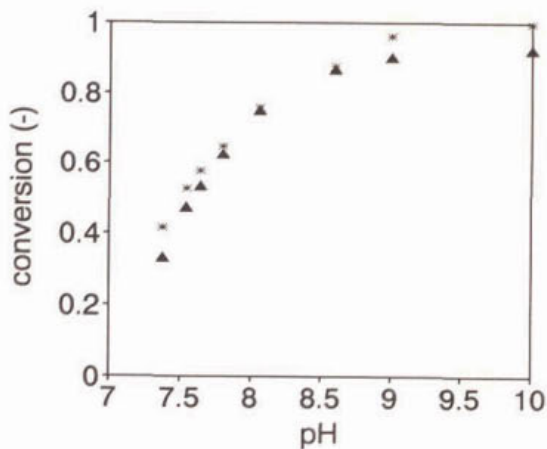


Figure 4. Equilibrium (*) and measured (▲) conversion as functions of the measured pH for a precipitation time of 2 s in the MSMPR-PFR.

for various calcium and phosphate concentrations (Chapter 2). Therefore, the K_s value of $3 \cdot 10^{-27} \text{ kmol}^5 \cdot \text{m}^{-15}$ can be used to predict the conversion when a reactor is fed with solutions of arbitrary composition.

4.5.2 Continuous experiments

Continuous experiments were performed in order to study the early stages of ACP precipitation (0.5-30 s). Firstly the main features of the precipitation process are compared to the results obtained with a batch reactor. Next the elementary processes (nucleation, molecular growth, aggregation and breakage) in the MSMPR and in the PFR are identified. The absence of nucleation and growth in the PFR is demonstrated and the sensibility of all elementary processes to the chemical and hydrodynamic conditions in the reactor is shown. Finally, each of the elementary processes are separately considered in more detail.

4.5.2.1 Early stages of ACP precipitation

The product obtained from solutions with Ca and P concentrations of respectively $4.8 \cdot 10^{-3}$

and $1.6 \cdot 10^{-3} \text{ kmol} \cdot \text{m}^{-3}$ as well as pH values between 7.1 and 10 in an MSMPR was similar to that found in batchwise operation. For some samples the x-ray diffraction showed a low crystallinity material with wide peaks that matched those of HAP and TCP. A mixture of an amorphous and crystalline material was found under the TEM. It is not clear whether this crystalline material was formed in the reactor or during the drying process.

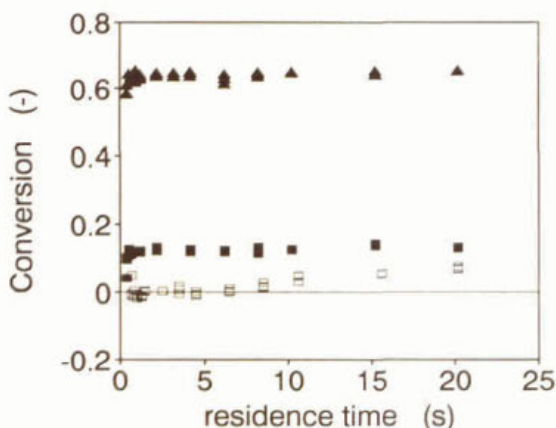


Figure 5. Conversion in a MSMPR-PFR as a function of time for measured outlet pH values of 7.7 (▲), 7.2 (■) and 7.1 (□). Exps. CONV7.7, CONV7.2 and CONV7.1. Residence time=0 at the MSMPR inlet.

Figure 5 shows the development of the conversion with time in the MSMPR-PFR for 3 pH values. Typically, the conversion increased abruptly at the beginning of the precipitation process (times of 0.5 s or less) and then further increased slowly. These results are consistent with the first and second precipitation stages observed in the batch reactor. If the pH was low enough, however, an induction time of a few seconds preceded precipitation.

4.5.2.2 Elementary processes in the MSMPR

Nucleation and molecular growth of ACP took place in the MSMPR, since a non-negligible conversion was measured right at its outlet (Figure 5, except for a pH of 7.1). For most experiments, the PSD at the MSMPR outlet had the typical form shown in Figure 6. Very large particles ($\sim 100 \mu\text{m}$) were produced in a short precipitation time (2 s, which is the residence time in the reactor plus in the measuring device), so the corresponding apparent growth rate, of $\sim 10^6 \text{ m/s}$, was much higher than that of slightly soluble compounds. Therefore the large particles produced in the MSMPR must have been formed by *aggregation*. *Breakage* is likely to have occurred in the MSMPR as well, as suggested by the loose structure of the particles (each particle is a large aggregate of the primary particles

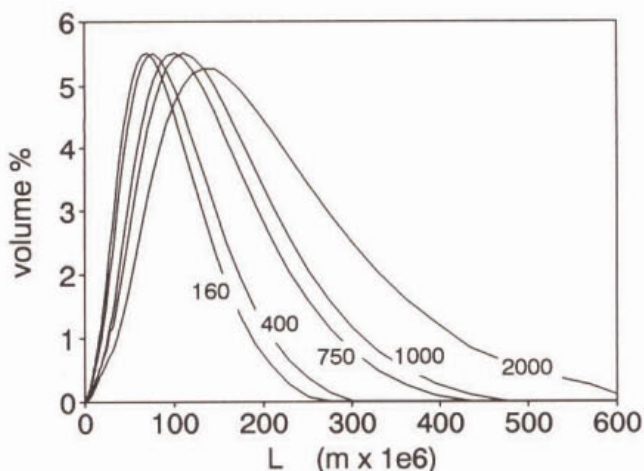


Figure 6. PSD at the MSMPR outlet for various impeller rotation speeds (rpm). Exps. N0160 to N2000, pH=7.8, precipitation time =2 s.

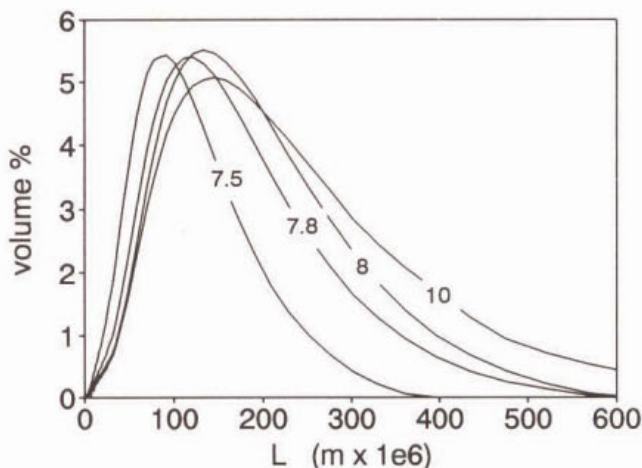


Figure 7. PSD at the MSMPR outlet for various pH values. Exp. PH7.5 to PH10. Rotation speed =750 rpm, precipitation time=2 s.

shown in the TEM view, Figure 2), by the large particle sizes (breakage is usually more intense for large particles) and by the high energy dissipation rate in the MSMPR ($\sim 3 \text{ W} \cdot \text{kg}^{-1}$). Breakage did occur in the PFR (see below) for particles sizes of $\sim 100 \mu\text{m}$ and mixing intensities of ~ 1 to $3 \text{ W} \cdot \text{kg}^{-1}$, thus comparable to those in the MSMPR.

The PSD at the outlet of the MSMPR (~ 2 s) shifted towards larger sizes as the mixer rotation speed increased (Figure 6, exp. N0160, N0400, N0750, N1000, N2000). The same occurred when the pH increased (Figure 7). Therefore the elementary processes in the MSMPR were sensitive to both *hydrodynamic and chemical conditions*.

4.5.2.3 Elementary processes in the PFR

Hardly any conversion occurred in the PFR, as Figure 5 shows, so that *molecular growth* was also negligible. Figure 8 (exp. E1.0) gives the PSD in the PFR for various precipitation times. The precipitation time of 2 s corresponds to the PFR inlet (MSMPR outlet plus residence time in the measuring device). The particles increased in size between precipitation

times of 2 and 5 seconds, showing that *aggregation* was the dominant process. After 5 seconds the PSD shifted to smaller sizes again, indicating that *breakage* became dominant. Breakage was not effective for the smallest particles, since particles smaller than 10 μm were not detected. This observation indicates that the equal-volume breakage model adopted in this work is more adequate than attrition models. The absence of particles smaller than 10 μm also indicates that *primary nucleation* did not play a role in the PFR. Therefore the only processes taking place in the PFR were aggregation and breakage.

The aggregation and breakage in the PFR were sensitive to *hydrodynamic conditions*. For a low mixing intensity ($1.0 \text{ W}\cdot\text{kg}^{-1}$) the PSD behaved as explained before: first the PSD shifted to the right and then to the left (Figure 8). As the mixing intensity in the PFR increased from $1.0 \text{ W}\cdot\text{kg}^{-1}$ to $1.8 \text{ W}\cdot\text{kg}^{-1}$ the initial shift to the right in the curve PSD-time became less pronounced (not shown). A further increase in the mixing intensity to $2.9 \text{ W}\cdot\text{kg}^{-1}$ resulted in an initial shift in the opposite direction, i.e. towards smaller sizes (Figure 9).

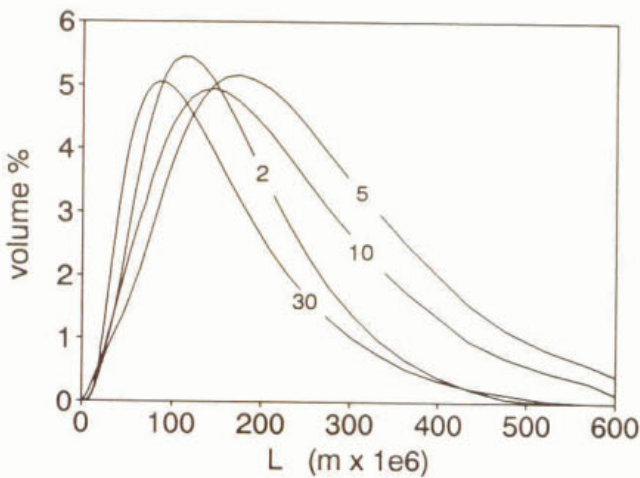


Figure 8. PSD in the PFR for various precipitation times (s). Exp. E1.0. Rotation speed =750 rpm, mixing intensity PFR =1 W/kg, pH=7.8. The PSD shifts first to the right (due to aggregation) and then to the left (due to breakage).

4.5.2.4 Molecular growth

Molecular growth occurred mainly in the MSMPR. For this type of reactor, the growth rate of the primary particles (G), the number-averaged primary particle size ($L_{1,0,primary}$) and the residence time (t) are related to each other as [6]

$$L_{1,0,primary} = G \cdot t \tag{27}$$

$L_{1,0,primary}$ was estimated as $\sim 2 \cdot 10^{-8}$ m from TEM views for a residence time of ~ 0.5 s, so eq. (27) gives a growth rate of $\sim 4 \cdot 10^{-8}$ m/s.

4.5.2.5 Nucleation

First it will be shown that nucleation in the MSMPR is likely to proceed by a homogenous mechanism, since the number concentration of primary particles ($m_{0,primary}$) produced was much larger than the concentration of

heterogeneous nuclei normally found in solutions. An estimate of $m_{0,primary}$ can be obtained from eq. (20),

$$m_{0,primary} = \frac{m_{3,primary}}{L_{3,0,primary}^3} \quad (28)$$

It can be easily demonstrated from the theory of an MSMPR [17] that

$$\begin{aligned} L_{3,0,primary} &= \sqrt[3]{6} \cdot G \cdot t \\ L_{1,0,primary} &= G \cdot t \end{aligned} \quad (29)$$

Substitution in eq. (28) gives

$$m_{0,primary} = \frac{m_{3,primary}}{6 \cdot L_{1,0,primary}^3} \quad (30)$$

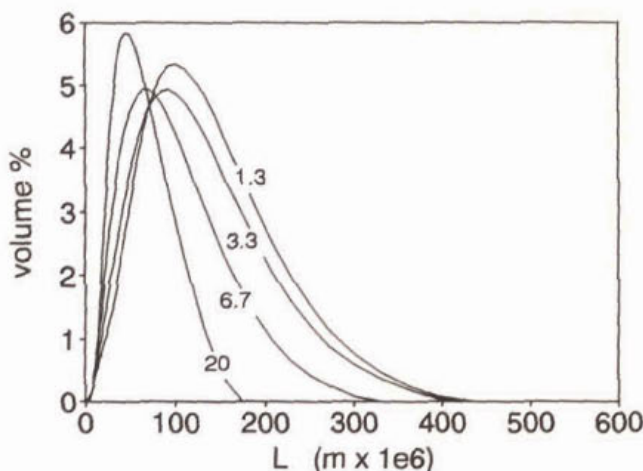


Figure 9. PSD in the PFR for various precipitation times (s) and for a high mixing intensity of $2.9 \text{ W} \cdot \text{kg}^{-1}$. Exp. E2.9. Rotation speed = 750 rpm. pH=7.8. The PSD shifts only to the left (due to breakage).

The number-averaged primary particle size $L_{1,0,primary}$ was estimated from the TEM views as $2 \cdot 10^{-8}$ m. The 3rd moment of the distribution $m_{3,primary}$ was calculated from eq. (23) with the primary particle density $\rho_{ACP, primary}$ instead of the particle density. The value of tricalcium phosphate was used for $\rho_{ACP, primary}$, $3140 \text{ kg} \cdot \text{m}^{-3}$. Other conditions were an inlet phosphate concentration c_{pin} of $1.6 \cdot 10^{-3} \text{ kmol} \cdot \text{m}^{-3}$, a conversion X of 0.5 and a precipitation time t of 0.5 s. Equation (30) thus gives a primary particle number concentration $m_{0,primary} \sim 2 \cdot 10^{18} \text{ \#} \cdot \text{m}^{-3}$, much higher than the concentration of heterogenous nuclei of 10^{12} to $10^{14} \text{ \#} \cdot \text{m}^{-3}$ (Walton, [23]). The nucleation kinetics can therefore be estimated assuming homogenous nucleation.

Nielsen [14] gives the following expression for the kinetics of homogeneous nucleation:

$$J = \frac{D}{d_{molec}^5} \beta^2 \left(\frac{k^3 T^3}{3\pi \sigma^3 v_{molec}^2 k_{cl}} \right)^{1/2} \exp\left(-\frac{\sigma^3 v_{molec}^2 k_{cl}}{k^3 T^3 \beta^2}\right) \quad (31)$$

The theory of homogeneous nucleation also gives a relation for the critical nucleus size:

$$r^* = 2 v_{molec} \sigma / k T \beta \quad (32)$$

If the nucleation rate J and the corresponding supersaturation (β defined in eq. (18)) are experimentally determined, then eq.(31) can be used to calculate the cluster surface tension. This parameter is independent of the supersaturation, so the nucleation rate for any solution composition can be predicted.

A method to calculate nucleation rates from induction time measurements in unseeded precipitation has been proposed [9,21,22], that is based on the assumptions of constant growth rate and on progressive primary nucleation rate. This leads to

$$t_{ind} = \sqrt[4]{\frac{4 \cdot m_{3,primary}}{J \cdot G^3}} \quad (33)$$

where the induction time t_{ind} is defined as the time needed for the formation of a detectable macroscopic volume fraction $k \cdot m_{3,primary}$ of the new phase. Eq. (33) can be used for the

conditions of experiment CONV7.1, where an induction time t_{ind} of 8 s was observed (see Figure 5). From the process conditions and parameters shown in Table IV and from eqs. (23) and (33) an experimental nucleation rate J of $10^{14} \text{ \#} \cdot \text{m}^{-3} \cdot \text{s}^{-1}$ was determined.

The experimentally determined nucleation rate of $10^{14} \text{ \#} \cdot \text{m}^{-3} \cdot \text{s}^{-1}$, the corresponding supersaturation of 1.04 and the data of Table IV were inserted in eq. (31) to give a cluster surface tension σ of $20.27 \text{ mJ} \cdot \text{m}^{-2}$.

Since the pre-exponential term in eq.(31) varies little with the supersaturation in comparison with the exponential term, it can be assumed to be constant. The expression for the nucleation of ACP then becomes

$$J = 10^{35} \exp(-54 / \beta^2) \text{ \#} \cdot \text{m}^{-3} \cdot \text{s}^{-1} \quad (34)$$

The expression above is consistent with the experimental results of Lundager Madsen et. al. [10]. However, they calculated a surface tension of $81 \text{ mJ} \cdot \text{m}^{-2}$, much higher than the value found here. This discrepancy was mainly caused by the different assumptions made in the calculations (mainly the definition of the supersaturation and the assumed solubility of ACP), and not by the difference in the experimental results.

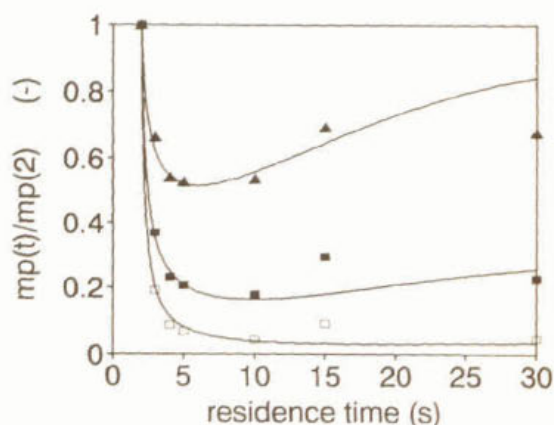
The cluster surface tension and the supersaturation were next inserted in eq. (32) to give a radius of the critical nucleus r^* of $1.6 \cdot 10^{-9} \text{ m}$, which corresponds ~ 13 ACP molecules.

4.5.2.6 Aggregation and breakage

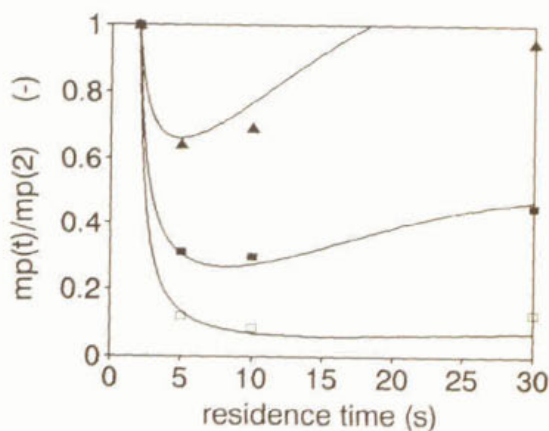
It has been shown that aggregation and breakage occur in both the MSMPR and in the PFR. In the PFR, these are the only processes taking place, so that a quantitative analysis is possible, based on the mathematical model presented earlier. The analysis was made in terms of the development of the moments of the PSD with time.

Table IV. Process conditions and parameters used in the equation for primary nucleation. Exp. CONV7.1.

c_{Pin}	$1.6 \cdot 10^3$	$\text{kmol} \cdot \text{m}^{-3}$
D	10^{-9}	$\text{m}^2 \cdot \text{s}^{-1}$
d_{molec} (TCP)	$6.79 \cdot 10^{-10}$	m
G (MSMPR)	$\sim 4 \cdot 10^{-8}$	$\text{m} \cdot \text{s}^{-1}$
k_v	$\pi/6$	-
k_{cl} (spheres)	16.755	-
mw_{ACP}	310	$\text{kg} \cdot \text{kmol}^{-1}$
v_{molec}	$1.64 \cdot 10^{-28}$	m^3
T	298	K
X	0.03	-
β	1.04	-
δ_p	2	-
$\rho_{ACP,primary}$	3140	$\text{kg} \cdot \text{m}^{-3}$



(a)



(b)

Figure 10. Normalized 0th (□), 1st (■) and 2nd (▲) moments of the PSD as functions of time for 160 rpm (a) and 1000 rpm (b). Exp. N0160, N1000. Data points are exp. values, lines model predictions.

measured moments of the distribution and the results are shown in Table III. For given process conditions (inlet PSD, pH and mixing intensity in the PFR), one value for k_{ag} and one for k_{br} were chosen for each set of moments m_0 , m_1 and m_2 and for all precipitation times. In general a good fit of all the 3 moments was obtained (Figure 10a), but sometimes large deviations in one of the moments occurred (e.g. m_2 in Figure 10b).

Figure 10a shows the moments of the PSD as functions of time, normalized with respect to the moments at the inlet of the PFR. Typically an abrupt decrease of the measured moments m_0 , m_1 and m_2 took place within a precipitation time of 5 seconds, followed by a slight increase which continued up to the longest precipitation time studied. Since aggregation causes a reduction in the moments m_0 , m_1 and m_2 whereas breakage causes an increase, the variation of the moments with time provides an interpretation of the processes in the PFR in a way similar to the analysis already presented in section 4.5.2.3 which was based on the development of the PSD with time.

The model parameters, k_{ag} and k_{br} , were adjusted to the

The impeller rotation speed in the MSMPR was varied in experiments N0160, N0400, N0750, N1000, N2000, i.e. the moments of the PSD at the inlet of the PFR were changed (at higher rotation speeds the particle size at the inlet of the PFR was larger). Since only the inlet condition of eq. (17) changed, the aggregation and breakage parameters are expected to remain constant throughout these experiments. Indeed, the breakage parameter remained approximately constant, but the aggregation parameter increased with the rotation speed, indicating that aggregation increases with the particle size. It is unlikely that the residual supersaturation at the outlet of the MSMPR, which may have varied with the rotation speed in the MSMPR, affected the aggregation rate. As the mixer speed is increased, a lower residual supersaturation is expected and therefore a lower k_{ag} , contrary to the observed trend.

The energy dissipation rate in the PFR was varied in experiments E1.0, E1.8, E2.9. The breakage parameter increased with the energy dissipation rate as expected, but the aggregation parameter decreased. If orthokinetic aggregation is considered, k_{ag} is expected to increase with the mixing intensity because of an enhancement in the particles collision frequency. If perikinetic aggregation is assumed, k_{ag} should be independent of the mixing intensity because the collisions are caused by brownian motion within the eddies in the turbulent field. The observed variation of k_{ag} with the mixing intensity can therefore not be explained by either of the two aggregation mechanisms. It is possible that k_{ag} varied with the particle size, which was not constant throughout these experiments. This possibility is further explored below.

The observed variation of k_{ag} with the mixing intensity in the PFR as well as with the inlet conditions (exp. E1.0, E1.8, E2.9 and N0160, N0400, N0750, N1000, N2000) may be explained from its dependency on the volume-averaged particle size ($L_{4,3}$). In Figure 11 the aggregation rate constant k_{ag} for each experiment is plotted against the time-averaged $L_{4,3}$ value. The time-averaged particle size was chosen because the rate constants are based on integral measurements over the PFR. At a pH of 7.8 there is a linear correlation between k_{ag} and $L_{4,3}$, in contradiction with the adopted assumption of size independent aggregation. Because of this contradiction, a different approach is followed in Chapter 7, where an implicit size dependent aggregation constant is introduced based on a general physical model.

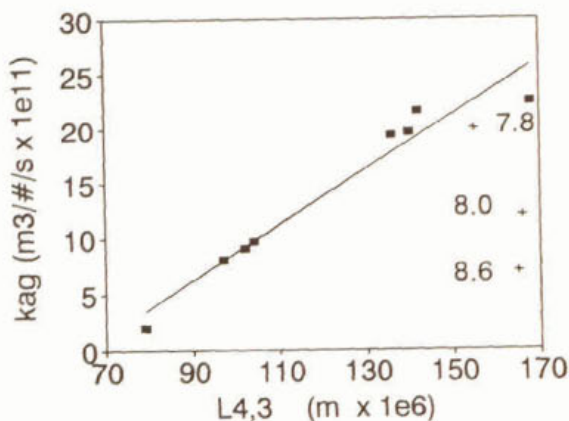


Figure 11. Aggregation rate constant as a function of the time-averaged particle size for a pH 7.8 (■, exp. E1.0 to E2.9, N0160 to N2000) and for varying pH (+, exp. PH7.8 to PH8.6). A linear relationship exists for points at a pH=7.8.

pH of 7 [18]. The value for ACP is not known.

4.6 Implications for a fluidized bed for phosphate removal

A fluidized bed for phosphate removal contains, besides primary particles, large sand grains of $\sim 500 \mu\text{m}$, so the following elementary processes take place: (i) nucleation, molecular growth, aggregation and breakage of primary particles; (ii) molecular growth of grains; (iii) aggregation between primary particles and grains; (iv) abrasion (breakage) of grains. The processes in (i) are related to primary particles and were studied in this Chapter. The other processes are governed by the same laws as those in (i), so the results obtained for primary particles in an MSMR-PFR may be, at least qualitatively, extrapolated to the fluidized bed.

ACP was found to precipitate very rapidly and to have a strong tendency towards aggregation. The aggregates formed loose structures which were easily broken by shear stresses in the flow field. In a fluidized bed it is likely that conversion and aggregation rates are slower, since the mixing of reactants is less intense: $E_{\text{Fluid Bed}} \sim 0.05 \text{ W} \cdot \text{kg}^{-1}$ far from inlet

Table III shows that the aggregation rate constant increased as the pH decreased. The reason for this behavior might well be in the value of the zeta-potential of the particles, which strongly depends on the pH level and which should be close to zero to lead to a maximum in the aggregation rate constant (this holds for both orthokinetic and perikinetic aggregation). For synthetic hydroxyapatite the zeta-potential equals zero at a

nozzles and $\sim 0.09 \text{ W}\cdot\text{kg}^{-1}$ at the bottom (Chapter 7), whereas $E_{\text{MSMPR}} \sim 3 \text{ W}\cdot\text{kg}^{-1}$ and $E_{\text{PFR}} \sim 1 \text{ W}\cdot\text{kg}^{-1}$. Conversion times of $\sim 10 \text{ s}$, longer than the value $\sim 0.5 \text{ s}$ found in the MSMPR-PFR, were indeed observed in a fluidized bed (Chapter 3), indicating that the conversion rate in a fluidized bed is largely determined by hydrodynamic conditions.

In order to improve the phosphate removal efficiency in a fluidized bed, molecular growth upon the grains and aggregation fines-grains have to be stimulated, whereas grains abrasion has to be minimized. Molecular growth on the grains surface can only occur in a small volume in the reactor, where the conversion into primary particles is incomplete. It is therefore necessary to offer as much grain surface area as possible near the inlet nozzles. An optimization of the aggregation-breakage behavior in the fluidized bed might be achieved by adjusting the mixing intensity in the bed, specially near the inlet nozzles. The optimum energy dissipation rate has to be found with experiments in a fluidized bed.

Aggregation was found to be more pronounced for a low pH value of 7.8 than for a pH of 8.6. This is consistent with the measured phosphate removal efficiency of a fluidized bed in the absence of carbonate and magnesium ions (Figure 6 of Chapter 2), which increased as the pH decreased from 8.2 to 7. It is likely that at the low pH values the zeta-potential of ACP is lower, so stimulating aggregation and thus the P removal efficiency. The pH value which stimulates aggregation the most seemed to derive from a compromise between the chemical conversion, which increased with the pH, and the zeta-potential controlled aggregation rate, which probably decreased with the pH.

The recrystallization of ACP into HAP is a slow process ($\sim 1000 \text{ s}$). Residence times of the liquid phase in a fluidized bed are short ($\sim 200 \text{ s}$), so recrystallization of fines is unlikely. The residence time of the grains is much larger, so the formation of HAP upon the grains might occur. However, continuous deposition of fresh ACP upon the grains by aggregation is likely to hinder HAP formation to some extent.

4.7 Conclusions

The precipitation features of calcium phosphate precipitation for Ca and P concentrations of respectively $4.8 \cdot 10^{-3}$ and $1.6 \cdot 10^{-3} \text{ kmol} \cdot \text{m}^{-3}$ as well as pH values between 7.1 and 10 were studied.

Calcium phosphate precipitates as an amorphous material (ACP) with a Ca/P molar ratio of 1.48 and a solubility K_s of $3 \cdot 10^{-27} \text{ kmol}^5 \cdot \text{m}^{-15}$ (based on activities). Conversion of phosphate ions from the liquid to the solid phase proceeds within 0.5 s or less. The elementary processes responsible for this conversion are homogeneous nucleation and molecular growth. The primary particles are $\sim 5 \cdot 10^{-8} \text{ m}$ in diameter and further aggregate to form particles of $100 \mu\text{m}$ within 2 s. For longer precipitation times nucleation and molecular growth become negligible so that further particle growth occurs only by aggregation. As the particles grow, breakage becomes increasingly important so a constant PSD is approached within $\sim 30 \text{ s}$.

The following expression for the rate of homogeneous nucleation was found:

$$J = 10^{35} \exp(-54 / \beta^2) \quad \# \cdot \text{m}^{-3} \cdot \text{s}^{-1}$$

The kinetics of aggregation and breakage were described by a mathematical model with size independent aggregation and breakage proportional to the particle size. The breakage rate parameter increased with the energy dissipation rate in the PFR. The aggregation rate parameter decreased with the pH. This parameter increased with the particle size, in contradiction with the assumption of size independent aggregation. These parameters were within the ranges

$$k_{ag} \sim (2 \text{ to } 23) \cdot 10^{-11} \quad \#^{-1} \cdot \text{m}^3 \cdot \text{s}^{-1}$$

$$k_{br} \sim 4000 \text{ to } 8000 \quad \# \cdot \text{m}^{-1} \cdot \text{s}^{-1}$$

List of symbols

()	ion activity, $\text{kmol}\cdot\text{m}^{-3}$	N_p	power number, -
B	birth function, $\#\cdot\text{m}^{-3}\cdot\text{m}^{-1}\cdot\text{s}^{-1}$	r^*	size of critical nucleus, m
c_{pliq}	concentration of dissolved phosphate, $\text{kmol}\cdot\text{m}^{-3}$	s	exponential factor for the breakage rate
c_{pin}	phosphate concentration at the MSMPR inlet after mixing of reactants, $\text{kmol}\cdot\text{m}^{-3}$	t	precipitation time, s
d_{molec}	molecular diameter, m	T	temperature, K
D	death function, $\#\cdot\text{m}^{-3}\cdot\text{m}^{-1}\cdot\text{s}^{-1}$	v_{molec}	molecular volume, m^3
D	molecular diffusivity, $\text{m}^2\cdot\text{s}^{-1}$	v_{sup}	superficial velocity, $\text{m}\cdot\text{s}^{-1}$
D_i	impeller diameter, m	vol%	volume percent
D_R, L_R	PFR diameter, length, m	V	MSMPR volume, m^3
E	mixing intensity, $\text{W}\cdot\text{kg}^{-1}=\text{m}^2\cdot\text{s}^{-3}$	x	axial position in the PFR
f	friction factor, -	X	conversion, -
g	gravity, $\text{m}\cdot\text{s}^{-2}$	<i>Greek letters</i>	
G	growth rate, $\text{m}\cdot\text{s}^{-1}$	β	supersaturation, -
J	nucleation rate, $\#\cdot\text{m}^{-3}\cdot\text{s}^{-1}$	δ_p	number of P atoms in the ACP molecule
k	Boltzmann constant, $=1.38\cdot 10^{-23} \text{ J}\cdot\text{K}^{-1}$	ΔP	pressure drop, $\text{N}\cdot\text{m}^{-2}$
k_{ag}	aggregation parameter, $\#\cdot\text{m}^3\cdot\text{s}^{-1}$	ρ	density, $\text{kg}\cdot\text{m}^{-3}$
k_{br}	breakage parameter, $\#\cdot\text{m}^{-1}\cdot\text{s}^{-1}$	σ	interfacial tension, $\text{J}\cdot\text{m}^{-2}$
k_{cl}, k_v	cluster and volume shape factors, -	<i>Super- and subscripts</i>	
K_s	solubility product of ACP in activities, $\text{kmol}^5\cdot\text{m}^{-15}$	0	at the PFR inlet
$L_{i,j}$	average particle size, defined in eq.(20), m	ag	aggregation
mw	molecular weight, $\text{kg}\cdot\text{kmol}^{-1}$	br	breakage
n	population density, $\#\cdot\text{m}^{-3}\cdot\text{m}^{-1}$	f	fluid
N	rotation speed, rpm	i	size range
		p	p^{th} moment of the PSD

References

1. Boskey, A.L. and Posner, A.S., Conversion of amorphous calcium phosphate to microcrystalline hydroxyapatite, A pH dependent, solution mediated, solid-solid conversion, *J. Phys. Chem.* **77**(19), p.2313-2317, 1973
2. Christoffersen, J. et. al., A contribution to the understanding of the formation of calcium phosphates, *J. Cryst. Growth* **94**, p.767-777, 1989.
3. Eanes, E.D., Gillessen and Posner, A.S., Intermediate states in the precipitation of hydroxyapatite, *Nature* **208**, October 23, 1965
4. Eanes, E.D. and Posner, A.S., Kinetics and mechanism of conversion of noncrystalline calcium phosphate to crystalline hydroxyapatite, *Trans. New York Academy of Sciences, Meeting of the Div. of Biophysics*, Nov. 18, 1965
5. Fueredi Milhofer et. al., Crystal growth and phase transformation in the precipitation of calcium phosphates, *Faraday Discuss. Chem. Soc.* **61**(Precipitation), p.184-193, 1976.
6. Jancic, S.J. and Grootcholten, P.A.M., *Industrial Crystallization*, Delft Univ. Press, Delft, 1984.
7. Hounslow, M.J., Ryall, R.L. and Marshall, V.R., A discretized balance for nucleation, growth and aggregation, *A.I.Ch.E.J.* **34**(11), p.1821-32, 1988
8. Hulburt, H.M. & Katz, S., Some problems in particle technology. A statistical mechanical formulation, *Chem. Eng. Sci.* **19**, p.555-574, 1964.
9. Kashchiev, D., Verdoes, D. and van Rosmalen, G.M., *J. Crystal Growth* **110**, p.373-, 1991.
10. Lundager Madsen, H.E., Lopez Valero, I., Lopez Acevedo, V. and Boistelle, R., The formation product of amorphous tricalcium phosphate at 37°, *J. Crystal Growth* **75**(3), p.429-34, 1986.
11. Melikhov, I.V., The effect of dissolved impurity on calcium phosphate nucleation in supersaturated medium, *J. Colloid Interface Sci.* **127**(2), p. 317-327, 1989
12. Meyer, J.L., Phase transformation in the spontaneous precipitation of calcium phosphate, *Croat. Chem. Acta* **56**(4), pp. 753-67, 1983
13. Meyer, J.L. and Weatherall, C.C., Amorphous to crystalline calcium phosphate phase

transformation at elevated pH, *J. Colloid and Interface Sci.* **89**(1), p.257-267, 1982

14. Nielsen, A.E., *Kinetics of precipitation*, Pergamon Press, London, 1964

15. Perry, R.H. and Green, D. (Editors), *Chemical Engineers Handbook*, 6th ed, Mc. Graw Hill, N.Y., 1984.

16. Randolph, A.D., Effect of crystal breakage on crystal size distribution in a mixed suspension crystallizer, *Ind. & Eng. Chem. Fund.* **8**(1), p.58-62, 1969.

17. Randolph, A.D. and Larson, M.A., *Theory of particulate processes. Analysis and techniques of continuous crystallization*, Academic Press, 2nd ed., 1988.

18. Somasundaran, P. and Wang, Y.H.C., Surface chemical characteristics and adsorption properties of apatite, in *Adsorption on and surface chemistry of hydroxyapatite*, Ed. D.N. Misra, Plenum Press, N.Y., 1984.

19. Termine, J.D. and Posner, A.S., Calcium phosphate formation in vitro. I. Factors affecting initial phase separation, *Arch. Biochem. Biophys.* **140**, p.307-317, 1970.

20. Tropp, J., Blumenthal, N.C. and Waugh, J.S., Phosphorus NMR study of solid amorphous calcium phosphate, *J. Am. Chem. Soc.* **105**, p.22-26, 1983.

21. van der Leeden, M.C., Verdoes, D., Kashchiev D., and van Rosmalen, G.M. In *Advances in Industrial Crystallization* (Eds. Garside, J., Davey R.J. and Jones, A.G., Butterworth-Heinemann, London, 1991), p. 31-.

22. Verdoes, D., *Calcium carbonate precipitation in relation to detergent performance*, Ph.D. Thesis, Delft University Press, Delft, 1991.

23. Walton, A.G., *The formation and properties of precipitates*, Interscience, 1967.

24. Walton, A.G. et. al., Nucleation of calcium phosphate from solution, *Canadian J. Chem.*, **45**, p.2696-2701, 1967.

CHAPTER 5

AXIAL DISTRIBUTION OF PARTICLES IN A FLUIDIZED BED FOR PHOSPHATE REMOVAL

Abstract

In a fluidized bed for phosphate removal, precipitation of a phosphate shell proceeds upon sand grains in fluidization. Since the shell is less dense than the sand grains, a suspension with a distribution in particle sizes and densities develops. The axial distribution of particles in such a system has been studied both theoretically and experimentally. Complete segregation occurred when the bed consisted of bare sand grains with a spread in sizes (100-300 μm and 200-600 μm). As growth of a phosphate shell developed upon the grains, partial mixing between the segregated layers proceeded. A mathematical model was developed which predicts the axial distribution of particles in the bed. The model is based on a velocity-voidage relationship and on a stability mechanism for segregation, coupled to a simplified description of the precipitation process. Simulations of the fluidized bed for phosphate removal show that sand grains of small sizes should be used to achieve a high phosphate content in the product as well as to maintain a high specific surface area of the grains. Besides, the use of sand grains of small sizes minimizes the amount of bare sand that segregates at the bottom of the bed just after its addition, an undesirable but unavoidable phenomenon.

5.1 Introduction

Phosphate removal in a fluidized bed is based on the precipitation of a mineral phosphate shell upon the sand grains which constitute the bed. Since the shell deposition occurs preferentially at the bottom of the bed, and since the mineral phosphate has a lower density than the sand grains, a suspension with a spread in sizes and densities develops. This normally gives rise to segregation. When there is a spread only in sizes or only in densities, the larger or denser particles segregate to the bottom. However, when there is a spread in both variables and when the larger particles have the lower densities, such as with shell

covered sand grains, segregation proceeds according to the local bed density. Usually, the removal of the particles and the addition of fresh sand grains is made intermittently, so that the fluidization characteristics change not only with the axial position, but also with time.

The fluidization characteristics of a fluidized bed for phosphate removal such as voidage, bed density and specific surface area of the particles affect the process performance in several ways. They play an important role in the phosphate removal since they determine the specific surface area available for growth. The specific surface area is particularly important at the lower part of the bed because of the preferential phosphate deposition at the bottom, where the supersaturation is the highest. The fluidization characteristics also determine the largest possible particle size undergoing fluidization, and consequently they impose an upper limit to the phosphate content of the produced particles. Segregation determines the fate of the freshly added sand grains within the bed. The surface of bare sand grains is unfavorable for phosphate deposition, so they should not reach the bottom of the bed when they are just added, but remain in the upper part of the bed until they are covered by a phosphate shell.

In this chapter the fluidization characteristics of a fluidized bed for phosphate removal are studied both theoretically and experimentally. A mathematical model of this system is developed, based on the velocity-voidage relationship and on the segregation in the bed according to the bed density, coupled to a simplified description of the precipitation process. Fluidization experiments are performed in order to determine whether the fluidized bed is well mixed or segregated, and if this behavior can be described by the mathematical model. Simulations are performed in order to optimize the operation of a fluidized bed for phosphate removal with respect to the phosphate content in the product and the specific surface area of the particles. Ways of minimizing the presence of bare sand grains at the bottom of the fluidized bed are discussed.

5.2 Theory

5.2.1 Definitions and terminology

Types of suspensions - the particles constituting a fluidized bed may have a distribution in properties such as size, density, shape, etc. A group of particles in the bed having the same properties (identical particles) is called a *bed component* or *suspension component*. The suspension as a whole is called a *multicomponent suspension*. A *binary suspension* contains only two components. If only one component is present, the term *monocomponent suspension* is used. A suspension is called *well mixed* if the volume fraction of all its components is independent of the axial position in the bed. If an objective correspondence exists between a suspension component and an axial position in the fluidized bed, the suspension is called *segregated*. For intermediate cases, the term *partially segregated suspension* is used. Often, components with dissimilar fluidization characteristics tend to segregate in *layers*. Each layer may contain one or more components.

Porosity or voidage (ϵ) - is the volume fraction of fluid in the bed.

Superficial velocity (v_{sup}) - is defined as the fluid flow rate divided by the cross section of the empty fluidized bed.

Particle terminal velocity (v_t) - When a single particle is allowed to settle in a infinite motionless fluid, gravity, drag and buoyancy forces act upon it. The stationary velocity attained when these forces balance each other is called the particle terminal velocity.

Particle settling velocity (v) - This is the analogue of the terminal velocity when a population of particles is settling (or is fluidized by an upgoing stream). The settling velocity is affected by particle-particle interactions, which alter the flow field in the continuous phase. The buoyancy forces acting upon the particle are determined by the bed density (see below) rather than by the liquid density. For the fluidization of monocomponent suspensions, the settling velocity is expressed as

$$v = \frac{v_{sup}}{\epsilon} \quad (1)$$

Particle density (ρ_p) - In a fluidized bed for phosphate removal the particles consist of a core of sand (usually quartz sand) covered by a phosphate shell (usually $\text{Ca}_3(\text{PO}_4)_2$). The average particle density is given by

$$\rho_p = (d_{core} / d_p)^3 \cdot (\rho_{core} - \rho_{shell}) + \rho_{shell} \quad (2)$$

Bed density (ρ_{bed}) - is defined as the volume averaged density of a suspension under fluidization. For a monocomponent suspension the bed density is given by

$$\rho_{bed} = \rho_f \cdot \epsilon + \rho_p \cdot (1 - \epsilon) \quad (3)$$

5.2.2 Fluidization of monocomponent suspensions

When a fluid flows upwards through a fixed bed of particles, the bed starts to expand when the pressure drop becomes equal to the bed weight. The bed expands smoothly as the superficial velocity increases up to the value of the particle terminal velocity. Khan and Richardson [2] compared several velocity-voidage relationships for uniformly sized spherical particles, and concluded that the equation suggested by Richardson and Zaki [6] gave the best agreement with the available experimental data over a wide range of Galileo number ($10^{-2} < \text{Ga} < 10^{10}$) and voidage values ($0.4 < \epsilon < 1$). This equation is limited, however, in that it requires knowledge about the particle terminal velocity. Its accuracy is therefore limited by the precision in the estimate of the terminal velocity. An equation which does not suffer from this limitation and is derived from the empirical Carman-Kozeny equation, is [8]

$$\frac{\epsilon^3}{(1-\epsilon)^{0.8}} = 130 \cdot \frac{v_{sup}^{1.2} \cdot (\mu/\rho_f)^{0.8}}{g \cdot d_p^{1.8}} \cdot \frac{\rho_f}{\rho_p - \rho_f} \quad (4)$$

Equation (4) was compared with the equation of Richardson and Zaki [6] for the

conditions of interest for this work, i.e. the fluidization of (non-spherical) bare sand as well as shell covered grains. Equation (4) showed a better agreement with the experiments, so it was chosen for further use. With equation (4) the voidage of a monocomponent suspension can be predicted if the particle size, density and the superficial velocity in the bed are known. Once the voidage is known, the bed density can be calculated from eq.(3). If the mass of particles is also known, the bed height can be calculated:

$$H = \frac{M_p}{\rho_p \cdot A \cdot (1 - e)} \quad (5)$$

Equation (5) can also be used to obtain the porosity of a monocomponent bed from measurements of the mass of particles (M_p) and of the bed height (H). In this way, the voidage-velocity relation, eq. (4), can be verified experimentally.

5.2.3 Fluidization of multicomponent suspensions

When particles of different sizes or densities constitute the fluidized bed, partial or total segregation may occur if the size or density ratios are large enough. The coarser or denser particles in the distribution tend to segregate to the bottom. For a population of particles with mixed sizes *and* densities the axial distribution of particles also depends on the superficial velocity and on the overall bed composition. For a binary suspension with denser particles of smaller diameter, Moritomi [3] has found that, at low superficial velocities, the denser (and smaller) particles segregate to the bottom of the bed. At intermediate velocities the bed becomes well mixed whereas at high fluid velocities the denser particles segregate to the top. The velocity at which the layers invert depends on the overall bed composition. The axial distribution of particles in these binary systems was described by a mathematical model developed by Gibilaro [1]. This model is based on *stability considerations*: the compositions of the layers adjust themselves in order to minimize the potential energy of the suspension. This condition is satisfied when the bed density at the bottom layer is maximal.

Syamlal [7] described the segregation in binary suspensions (for components of different density and size) by using a more fundamental approach. They applied mass and momentum

balance equations for the fluid and for the suspension components over each differential volume element in the fluidized bed. The stability requirements were incorporated in these balance equations. The axial and radial profiles of the volume fractions of the two suspension components were derived.

Patwardhan and Tien [4] developed a segregation model for multicomponent suspensions based on the settling velocities of the fluidized particles and on their random motion. The latter was described by an empirically determined particle *dispersion coefficient*. An axial particle distribution for multicomponent suspensions was obtained. They applied the method on adsorption beds upon which a bacterial film was deposited [5]. This model disregards the tendency for segregation dictated by stability considerations. This tendency may be neglected only if the fluidization characteristics of the various suspension components are similar.

5.2.4 Mathematical model for the axial distribution of particles in a fluidized bed for phosphate removal

5.2.4.1 Model selection

A fluidized bed for phosphate removal consists of a multicomponent system with a spread in particle sizes and densities, with fluidization characteristics governed by stability considerations as well as dispersion. Given the large spread in particle sizes and densities normally found in practice, it is likely that stability largely determines the overall system behavior. The mathematical models available in the literature are unsuitable to describe this system: Gibilaro's model [1] can only be applied to binary systems and Patwardhan's model [4] neglects stability considerations. Therefore a new model was developed, based on stability considerations, but extended to take into account multicomponent systems. A description of this model follows.

5.2.4.2 Fluidization

The fluidized bed reactor is fed at the bottom with a solution supersaturated with respect to the mineral phosphate salt. Precipitation of this salt occurs upon the sand grains thus developing a phosphate shell upon the grains. The particles (product) are intermittently removed at the bottom and at the same time fresh sand grains are added at the top. The

model describes the period between two successive product removal - sand grains addition events.

At the start, the fluidized bed consists of a discrete number of components 'i' of known density ($\rho_{p,i}$) and size ($d_{p,i}$). These bed components form completely segregated layers, each with the fluidization characteristics (bed density and voidage) of monocomponent fluidization. The bed density, voidage and bed height in each layer thus are calculated from the monocomponent fluidization equations presented earlier (eq.(3), (4) and (5), respectively). The total bed height is obtained simply by summing up the contributions of the 'i' suspension components,

$$H_{tot} = \sum_i H_i \quad (6)$$

The segregated layers are axially arranged in the bed in such a way that the potential energy of the system is minimized, i.e. the layers with the larger bed density values occupy lower axial positions in the bed.

The deposition of a phosphate shell upon the grains is assumed to take place only at the lowest segregated layer. As the particles grow the local bed density decreases. Eventually the bed density of the two lower layers become equal. When this occurs, the two layers are allowed to mix, thus forming a single, binary layer. Further growth of this layer may lead to further mixing with other layers in the bed, so that a multicomponent layer develops.

The height of a multicomponent layer (H_{layer}) is obtained by summing up the contribution of each suspension component in the layer. These contributions are obtained from the monocomponent fluidization equations (eq.(4) and (5)) and from the mass of each suspension component in the layer (M_i). The volume fraction of the suspension component 'i' in the layer is then calculated from

$$c_i = \frac{M_i}{\rho_{p,i}} \cdot \frac{1}{H_{layer} \cdot A} \quad (7)$$

Finally, the average layer porosity and the average bed density of the layer are obtained from

$$e_{avg} = 1 - \sum_i c_i \quad (8)$$

and

$$\rho_{bed,avg} = \sum_i \rho_{p,i} \cdot c_i + \rho_f \cdot e_{avg} \quad (9)$$

Equation (9) is the multicomponent equivalent of equation (3).

5.2.4.3 Deposition of a phosphate shell upon the grains

Since this Chapter is mainly focused on the fluidization aspects of a fluidized bed for phosphate removal, a simple description of the precipitation processes was adopted. Precipitation of a phosphate shell upon the grains was assumed to take place at a constant rate which is independent of fluidization conditions. The phosphate deposition rate upon the grains (ϕ_{shell} , in $m^3 \text{ shell} \cdot s^{-1}$) relates to measurable quantities as

$$\phi_{shell} = v_{sup} \cdot A \cdot c_{P,in} \cdot \eta \cdot \frac{mw}{\delta} \cdot \frac{1}{\rho_{shell}} \quad (10)$$

where the phosphate removal efficiency (η) is defined as the fraction of the phosphate flow entering the fluidized bed which is deposited upon the grains.

In Chapter 4 it was shown that precipitation is a rapid process which occurs mainly at the lower part of the bed. Here it is assumed that growth occurs only in the lowest layer. The layer is assumed to be well mixed so that growth occurs uniformly throughout the layer. The linear growth rate of the particles in the bottom layer thus only depends on the phosphate deposition rate (ϕ_{shell}) and on the total surface area of the particles, given by their volume (M_p/ρ_p) and size (d_p):

$$G = \frac{1}{3} \cdot \phi_{shell} \cdot d_p \cdot \frac{\rho_p}{M_p} \quad (11)$$

with G being defined as $d(d_p)/dt$. Equation (11) holds for spherical, smooth particles. If the layer is formed by more than one suspension component, eq. (11) is slightly adapted: the growth rate of each suspension component is calculated considering that the shell deposition rate on that component is the fraction of ϕ_{shell} that is proportional to the surface area of that component. Note that the identity of the suspension components within a layer is not lost. Once the growth rate is known, the changes in particle sizes and densities of all components in the layer with time can be calculated.

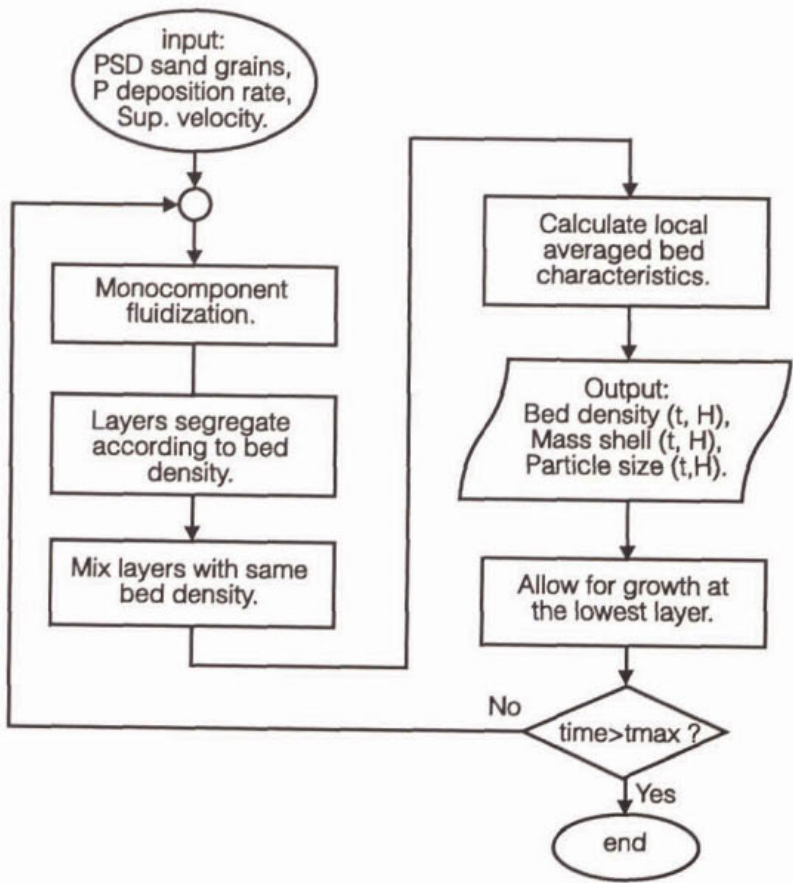


Figure 1. Block diagram of the mathematical model for the particle axial distribution in a fluidized bed for phosphate removal.

5.2.4.4 Model structure

The processes described in the previous sections (5.2.4.2 and 5.2.4.3) were incorporated in a Turbo-pascal (Borland) code. A block diagram of the model is presented in Figure 1. The main model inputs were the superficial velocity, the overall bed composition (mass fraction, density and size of each bed component) at the start of the process, the inlet flow, inlet phosphate concentration and the phosphate removal efficiency. Model outputs are fluidization characteristics (voidage, bed density, specific surface area, etc.) as well as characteristics of the solid phase (mass fraction of shell in the particle, particle size and core size) as functions of axial position and time. The only model parameters are the numerical coefficients in the velocity-voidage equation (eq.(4)).

5.3 Experimental

First the fluidization of sand grains was investigated for two size distributions as well as for two bed sizes. Subsequently the fluidization of sand grains covered by a phosphate shell with a density lower than the sand grain density was studied for two types of phosphate salts, for sand grains with two size distributions (narrow and wide) as well as for two precipitation times. An overview of the experimental conditions is given in Table I and Table II.

Table I. Experimental conditions ⁽¹⁾ a mixture of magnesium phosphate and amorphous calcium phosphate. ⁽²⁾ amorphous calcium phosphate.

exp. nr.	sand diameter (μm)	phosphate shell	bed diameter (m)	fluidization time (h)
Sf2	100-300	none	0.02	-
Sf5	100-300	none	0.05	-
Sc2	200-600	none	0.02	-
Sc5	200-600	none	0.05	-
MgP26	200-600	CaMgP ⁽¹⁾	0.02	26
MgP44	200-600	CaMgP ⁽¹⁾	0.02	44
CaP56	352-420	CaP ⁽²⁾	0.05	56

Table II. Flow rates, concentrations and pH values of the streams entering the fluidized bed for phosphate removal. n.m. = not measured.⁽¹⁾ top outlet reactor.

Stream nr.	flow $\text{m}^3 \cdot \text{s}^{-1}$ $\times 10^7$	P conc. $\text{kmol} \cdot \text{m}^{-3}$ $\times 10^3$	Ca conc. $\text{kmol} \cdot \text{m}^{-3}$ $\times 10^3$	Mg conc. $\text{kmol} \cdot \text{m}^{-3}$ $\times 10^3$	Na conc. $\text{kmol} \cdot \text{m}^{-3}$ $\times 10^3$	pH -
<i>Experiments MgP26 and MgP44</i>						
Influent	33	1.7	1.3	0	1.7	5
Mg soln.	1.1	0	0	100	0	n.m.
NaOH soln.	0.90	0	0	0	100	n.m.
<i>Total</i>	<i>218</i>	<i>1.6</i>	<i>1.2</i>	<i>3.2</i>	<i>4.1</i>	<i>9 \cdot 10^{(1)}</i>
<i>Experiment CaP56</i>						
Influent	213	1.7	0	0	1.7	5
Ca soln.	11	0	100	0	0	n.m.
NaOH soln.	5.6	0	0	0	100	n.m.
<i>Total</i>	<i>218</i>	<i>1.6</i>	<i>4.8</i>	<i>3.2</i>	<i>4.1</i>	<i>9 \cdot 10^{(1)}</i>

5.3.1 Equipment

Both fluidization columns used for the precipitation of the phosphate salts consisted of cylindrical perspex vessels, 2.1 m in height, with diameters of either 0.02 m or 0.05 m, and provided with three inlet nozzles (Figure 2a,b). The main nozzle was positioned vertically at the symmetry axis of the bed. In the bed of 0.02 m in diameter, the main nozzle had an open end, so the stream was injected axially. In the bed of 0.05 m, the main nozzle had four lateral holes, so four streams were injected radially at angles of 90° with respect to each other. The fluid velocity through the holes was 1 m/s. Two secondary nozzles were placed horizontally at the wall of the beds. The total flow rate through these nozzles was only 5% of the main flow and the fluid velocity at the nozzles was low (0.2 m/s). These inlet arrangements produced recirculating streams in the lowest 0.2 m of the bed, but above this level a smooth fluidization behavior was obtained.

The streams were pumped into the fluidized bed through peristaltic pumps, which provided the accuracy in flow rates required for precipitation. The oscillations in the flows, an

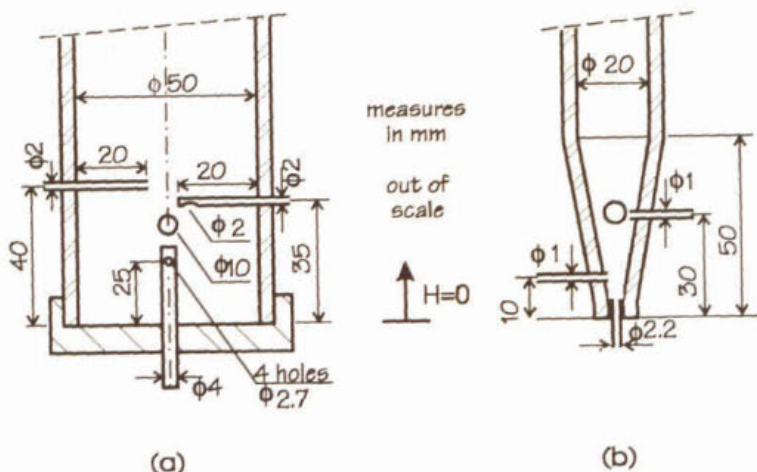


Figure 2. Lower part of fluidized beds with diameters 0.05 m (a) and 0.02 m (b). The reference position for the bed height is at $H=0$.

intrinsic property of this type of pump, were minimized by placing an air cushion at the outlet of each pump.

5.3.2 Experimental procedure

5.3.2.1 Fluidization of sand grains

In experiments Sf2, Sf5, Sc2 and Sc5 either the column with a diameter of 0.02 m or of 0.05 m was continuously fed with water at a superficial velocity of $0.011 \text{ m} \cdot \text{s}^{-1}$. Quartz sand with a density ρ_{core} of $2630 \text{ kg} \cdot \text{m}^{-3}$ and in either of the two size ranges shown in Figure 3 was used. The bed was sampled from the top to the bottom by suctioning. The number of layers sampled varied between 10 and 16 and their height from 0.05 m to 0.15 m. For each sampled layer 'i', the layer height (H_i), the mass of the particles (M_i) and the particle size distribution were measured.

5.3.2.2 Fluidization of sand grains covered with a phosphate shell: sand with a wide size distribution

In experiments MgP26 and MgP44 the column with a diameter of 0.02 m was continuously fed with an aqueous solution containing the calcium and phosphate ions as well as with two

small secondary streams consisting of a NaOH solution and a solution containing magnesium ions. The superficial velocity was $0.011 \text{ m}\cdot\text{s}^{-1}$. The flow rates and concentrations of the streams entering the fluidized bed are shown in Table II. The phosphate removal efficiency was 25%. At the start of each experiment *coarse* sand grains with the particle size distribution shown in Figure 3 and with a density of $2630 \text{ kg}\cdot\text{m}^{-3}$ were added. The phosphate shell deposited upon the sand grains consisted of a mixture of amorphous calcium phosphate ($\text{Ca}_3(\text{PO}_4)_2$) and magnesium phosphate ($\text{Mg}_3(\text{PO}_4)_2\cdot 22\text{H}_2\text{O}$) with a density of $1620 \text{ kg}\cdot\text{m}^{-3}$. No addition or removal of grains was applied during the experiments, so the deposition of a phosphate shell upon the grains caused the bed height to increase. The bed was sampled as explained previously.

For each sampled layer 'i', the layer height (H_i) and mass of the particles (M_i) were measured. The average particle density ($\rho_{p,i}$) was measured with a pycnometer. The average shell-to-core mass ratio ($M_{\text{shell},i}/M_{\text{core},i}$) was determined by dissolving the phosphate shell in $\text{HCl } 2 \text{ kmol}\cdot\text{m}^{-3}$ for a known particle mass. The average density of the phosphate shell ($\rho_{\text{shell},i}$) was

calculated from ρ_{core} , $\rho_{p,i}$ and $M_{\text{shell},i}/M_{\text{core},i}$. Finally, remaining sand grains were sieved so the core size distribution was determined. It was not possible to measure the particle size distribution of the shell covered grains because they abraded upon sieving. The experimentally determined particle density, shell density and the shell-to-core mass ratios are quantities averaged over the mixture of particles in layer 'i'. The distribution of these properties within a layer was not measured.

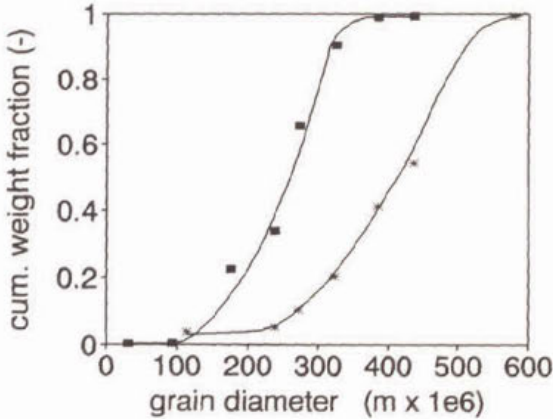


Figure 3. Particle size distribution of fine (■) and coarse (*) sand grains.

5.3.2.3 Fluidization of sand grains covered with a phosphate shell: sand with a narrow size

distribution

In experiment CaP56 the column with a diameter of 0.05 m was continuously fed with an aqueous solution containing phosphate ions as well as with two small secondary streams consisting of a NaOH solution and a solution containing calcium ions. The superficial velocity was $0.011 \text{ m}\cdot\text{s}^{-1}$. The flow rates and concentrations of the streams entering the fluidized bed are shown in Table II. The phosphate removal efficiency was 50%. At the start of the experiment sand grains were added, consisting mainly of quartz with a density of $\rho_{\text{core}} = 2630 \text{ kg}\cdot\text{m}^{-3}$ and with a narrow particle size distribution (352 - 420 μm). Amorphous calcium phosphate ($\text{Ca}_3(\text{PO}_4)_2$) with a density of $1990 \text{ kg}\cdot\text{m}^{-3}$ deposited upon the sand grains. The sampling procedure and the measurements in each sampled layer were the same as above. Additionally, the sampled layers were used for separate fluidization experiments in order to determine the average terminal velocity of the particles in each layer. The terminal velocity was obtained by measuring the voidage at varying superficial velocities. The limiting superficial velocity for $\epsilon \rightarrow 1$ was taken as the average terminal velocity of the particles.

5.4 Results and discussion

5.4.1 Accuracy of the predicted voidage

The accuracy of the voidage-velocity equation (eq. (4)) was evaluated by comparing predicted and experimentally determined values of voidage. The predicted values were derived from the mass averaged particle size and density measured for each sampled layer. Experimentally determined voidages of each layer followed from the substitution of the measured layer mass ($M_{p,i}$), layer height (H_i) and averaged particle density ($\rho_{p,i}$) values in eq. (5). Predicted and experimentally determined voidage values are compared in Figure 4. For the fluidization of sand grains the predicted and experimentally determined values agreed with each other within 0.03 voidage unit, but for the fluidization of particles with a phosphate shell, the predicted porosities were 0.07 voidage unit too low. These deviations are likely to be related to the presence of small primarily formed particles (fines) in the bed, which may have caused an increase in apparent viscosity of the liquid phase. The particle morphology may also have contributed to the deviations: the sand grains had smooth surfaces with sharp edges, whereas

the grown particles were spherical and had a rough, irregular surface.

5.4.2 Fluidization of sand grains

Firstly the fluidization conditions during the start-up are considered, where the fluidized bed is filled with sand grains upon which no phosphate shell is deposited. Particle size distributions of the layers in the bed from experiment Sc2 are shown in Figure 5. The largest particles occupy the lower part of the bed, as expected. This occurred irrespective of the bed size, 0.02 or 0.05 m, and of the size range of the sand grains, coarse or fine (exp. Sf2, Sf5, and Sc5, not shown).

The degree of segregation in the bed was evaluated by comparing the experimentally determined axial distribution of the voidage with model predictions for a completely segregated as well as for a well mixed bed, as shown in Figure 6a. The experimentally determined voidages were calculated as explained in section 5.4.1. The predicted voidages were derived from the overall bed composition (particle size distribution of the sand grains). The experimental data approached closely the behavior of a fully segregated bed, except at

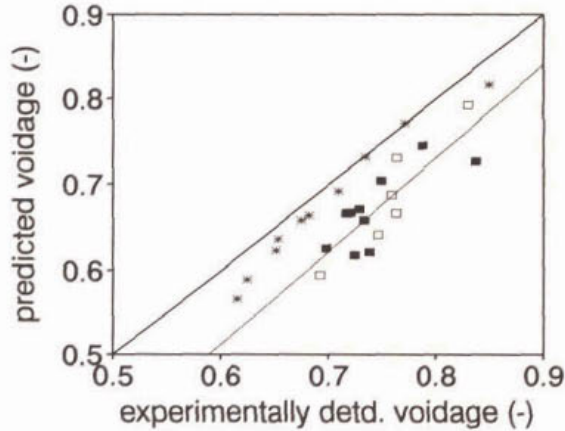


Figure 4. Predicted versus experimentally determined voidages for experiments Sc2 (*), MgP26 (□) and MgP44 (■). Dotted lines are regression values for P-covered grains.

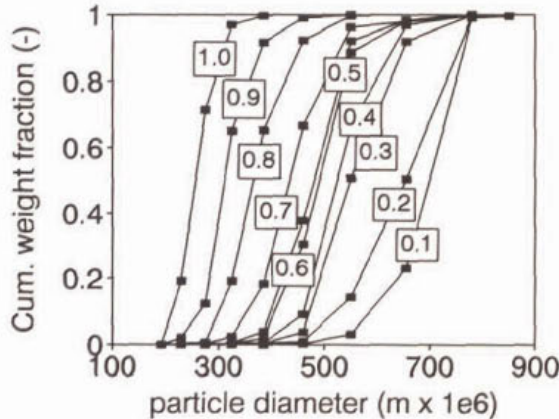


Figure 5. Size distribution of sand grains (exp. Sc5). Numbers on the lines indicate the normalized axial position (H/H_{tot}). Total bed height $H_{tot}=1.59$ m.

the lowest 0.2 m, where the inlet liquid jet promoted mixing of the solid phase. The mixing in the fluidized bed with a diameter of 0.02 m is more pronounced than in the bed with a diameter of 0.05 m (Figure 6a), but the fluidization pattern in most of the bed height was essentially the same for both fluidized beds. The design of the bed bottom therefore affected only the fluidization characteristics at the bottom, but not in the rest of the column. The segregation can also be studied in terms of the axial distribution of the bed density (Figure 6b). The approaches based on bed density and voidage are completely analogous, since the predicted bed density and voidage are related by eq. (3). The predicted and measured values of the total bed height agreed well with each other (1.66 and 1.67 m).

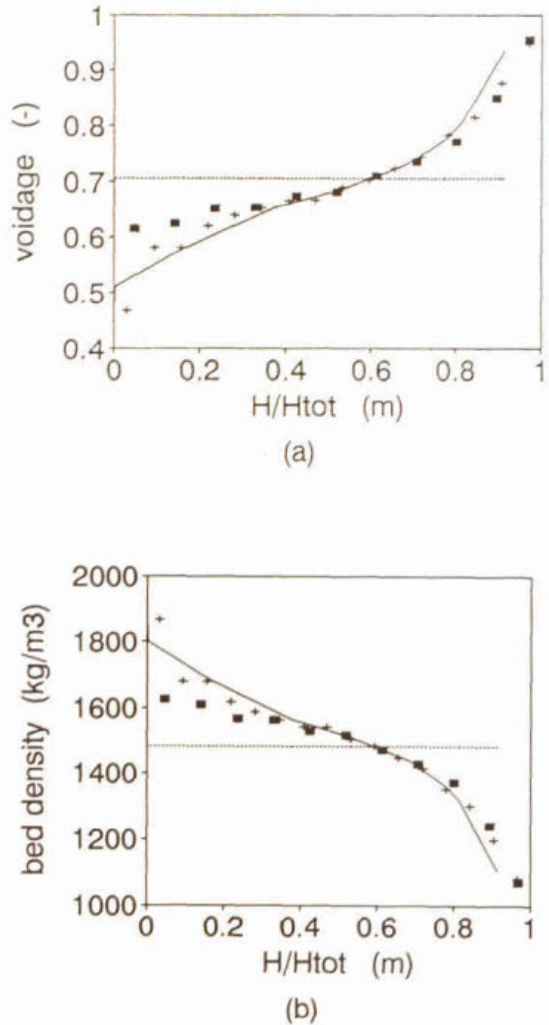


Figure 6. Voidage (a) and bed density (b) versus normalized bed height for coarse sand. Bed diameters 0.02 (■) and 0.05 m (+). Lines are predicted values. Exp. Sc2, Sc5.

5.4.3 Fluidization of sand grains covered with a phosphate shell: sand with a wide particle size distribution

The fluidization characteristics of a fluidized bed for phosphate removal was studied for precipitation times of 0, 26 and 44 hours. Immediately after the start the bed consisted of a fully segregated suspension of sand grains with a bed density and particle size decreasing with the bed height, as already mentioned in section 5.4.2.

Deposition of a phosphate shell upon the grains during 26 h straightened the bed density versus normalized bed height curve into a horizontal line for the major part of the bed height, as shown in Figure 7a. Upon further deposition till 44 h the curve remained flat but the absolute value of the bed density decreased slightly. These trends were qualitatively predicted theoretically, as indicated by the continuous lines in Figure 7a. The discrepancy between the measured and predicted bed density values in the figure follows from the fact that the voidage-velocity relationship did not describe the fluidization of grains covered by a phosphate shell as well as it did for sand grains (see section 5.4.1).

The measured shell-to-core mass ratio, $M_{\text{shell}}/M_{\text{core}}$, as a function of the normalized bed height is shown in Figure 7b. The ratio was constant at the lower part of the bed and decreased with the normalized bed height. The theoretical values of this variable, shown in the figure as continuous lines, agreed rather well with the experimental data. The theoretical curve, however, predicted that no phosphate shell was formed on the grains at the top of the bed, whereas some deposition was observed. This indicated either the presence of axial dispersion of the particles, or that some shell deposition also occurred at the top of the bed.

At first sight the data in Figure 7a and b seem to indicate that at 44 h a considerable part of the bed - from the bottom to a normalized height of 0.6 - formed a homogeneous layer. However, the axial distribution of the cores of the grains plotted in Figure 7c shows that this was not the case. Besides, the average core size at the bottom of the bed decreased with time from 600 to 500 μm , whereas at the top of the bed the opposite effect took place: the particle sizes increased from 220 to 320 μm (Figure 7c). Apparently particles were transported in the

axial direction: the initially fully segregated bed became partially mixed. All these trends are also predicted theoretically.

5.4.4 Fluidization of sand grains covered with a phosphate shell: sand with a narrow particle size distribution.

In section 5.4.3 a fluidized bed initially fed with sand having a wide particle size distribution was found to be segregated according to the bed densities of its components. In order to verify whether the model is still applicable when the bed densities of the components are close to each other, experiments using sand grains with a narrow size distribution (352 - 420 μm) were performed (exp. CaP56).

The bed density and mass fraction of phosphate shell upon the sand grains as functions of the axial position in the bed for a fluidization time of 56 h are shown in Figure 8a,b. The bed

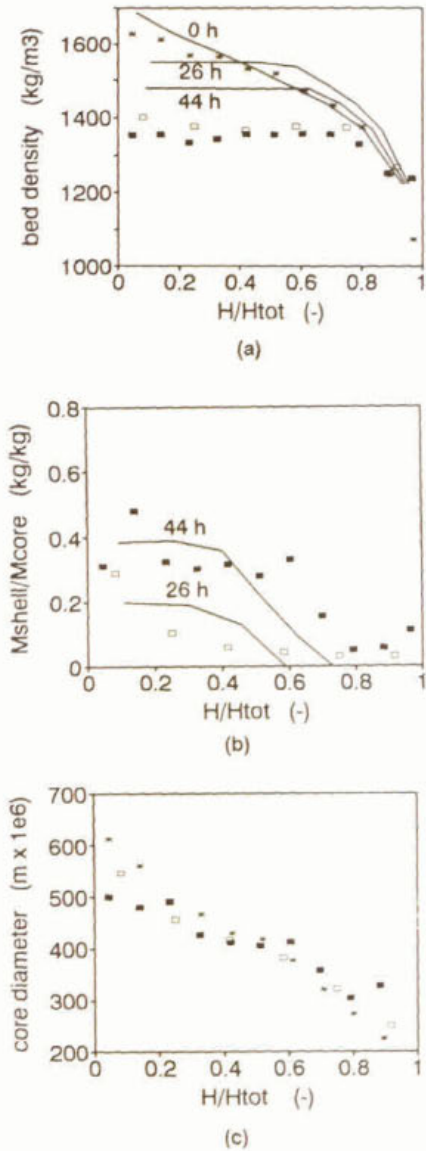


Figure 7. Bed density (a), shell mass fraction (b) and core size (c) against the normalized bed height. Sand with a wide size distribution, measured at 0 h (▲), 26 h (□), and 44 h (■). Lines are predicted values. Exp. Sc2, MgP26, MgP44.

density was constant throughout the bed and the mass fraction of the phosphate shell in the particles decreased with the bed height. As a further indication of segregation in the bed, the

terminal velocity of the particles in each layer were determined by separate experiments. The particles with the largest terminal velocities segregated at the bottom of the bed as shown in Figure 8b.

Segregation was, however, less pronounced than in the case of sand grains with a wide size distribution, as can be concluded by comparing the axial distribution of the phosphate content in the grains: there was a high phosphate content even at the top of the bed (Figure 8b), which was not the case for the sand grains with a wide spread in size (Figure 7b).

If it is considered that the bed is formed by a number of components with sizes within the range 380-420 μm , the model predicts reasonably well the observed axial distribution of bed density and shell-to-core mass ratio, shown as continuous lines in Figure 8a and b. This surprising result indicates that even small differences in bed density may give

rise to segregation in the bed. Note that the mathematical model is based on equilibrium considerations, which means that even an infinitesimal difference in the bed densities of the bed components is sufficient to promote segregation and that the model does not take into account *how large* the driving force for segregation is. In practice it is likely that if the

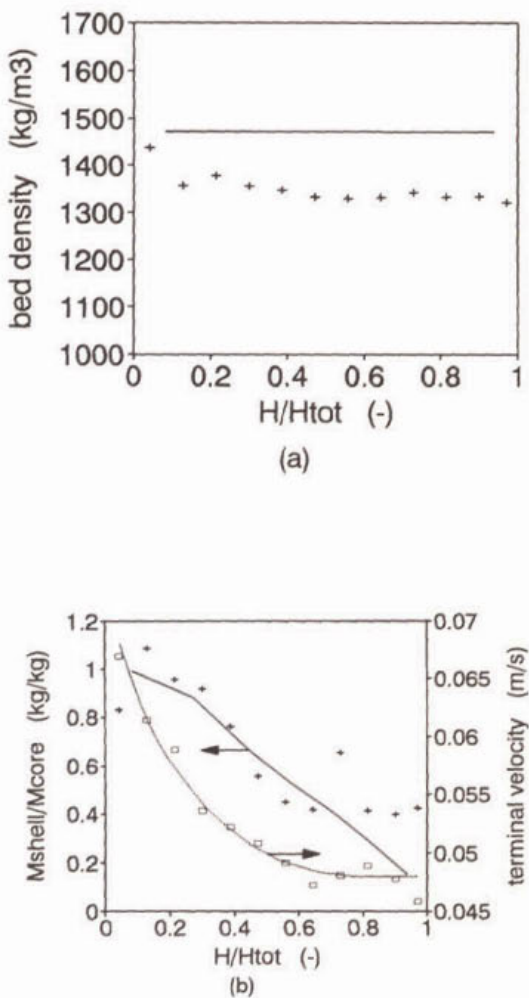


Figure 8. Bed density (a), shell mass fraction (b) and terminal velocity (b) against the normalized bed height. Sand with a narrow size distribution. Fluidization time of 56 h. Lines are predicted values. Exp. CaP56.

differences in bed density are small, such as for sand grains with a narrow particle size distribution, segregation becomes less important. Therefore, the possibility that the observed segregation was *not* governed by stability factors should also be considered: the observed segregation could be caused by the dispersion of the particles combined with a localized growth at the bottom of the bed.

5.4.5 Implications for a fluidized bed for phosphate removal

The mathematical model presented in section 5.2.4 is next used to optimize the operation of the fluidized bed with respect to the *phosphate content in the product* and the *specific surface area* of the particles at the bed bottom. Ways of minimizing the *presence of bare sand grains at the bed bottom* right after their addition, an undesirable but unavoidable phenomenon, are discussed.

5.4.5.1 Simulation conditions

Simulations of a fluidized bed for phosphate removal were performed for cores as well as shells of two size ranges and densities. The time interval between start-up and the first product removal/core addition event was simulated. At the start-up the bed was filled with bare cores. The operational conditions common for all the simulations are shown in Table III and those varied in each simulation in Table IV .

5.4.5.2 Phosphate content in the product

One of the basic features of the fluidized bed process is the possibility of recovering phosphate in a concentrated form. A high phosphate concentration in the product may be obtained by adjusting the chemistry of the system so that a concentrated phosphate modification is formed (e.g. amorphous calcium phosphate, $\text{Ca}_3(\text{PO}_4)_2$ instead of magnesium phosphate $\text{Mg}_3(\text{PO}_4)_2 \cdot 22\text{H}_2\text{O}$) and by adjusting the fluidization conditions so as to minimize the amount of sand grains incorporated in the product, i.e. by maximizing the shell-to-core mass ratio ($M_{\text{shell}}/M_{\text{core}}$). The latter is achieved by reducing the mass flow rate of sand to the system (the phosphate deposition rate cannot be varied because it is fixed by the inlet conditions, the phosphate removal efficiency and the phosphate modification formed). The flow rate of sand in intermittent operation may be reduced either by limiting the amount of

sand used in each sand addition event or by increasing the time interval between two additions. Since both alternatives are equivalent, only the latter situation was considered. The time interval between two successive sand grains additions is called 'fluidization time'.

Table III. Process conditions common to all simulations of a fluidized bed for phosphate removal.

Superficial velocity	$\text{m}\cdot\text{s}^{-1}$	0.011
Core mass	kg	2.5
P concentration influent	$\text{kmol}\cdot\text{m}^{-3}$	0.0016
P removal efficiency	-	0.5
Fluid density	$\text{kg}\cdot\text{m}^{-3}$	1000
Fluid viscosity	$\text{kg}\cdot\text{m}^{-1}\cdot\text{s}^{-1}$	0.001

Table IV. Process conditions for simulations of a fluidized bed for phosphate removal. ⁽¹⁾ PSD shown in Figure 3. ⁽²⁾ particle sizes twice as small as coarse sand.

Simulation case nr	PSD core	ρ_{shell}	ρ_{core}	$\rho_{\text{shell}}/\rho_{\text{core}}$
C8	coarse ⁽¹⁾	1990	2630	0.8
C6	coarse ⁽¹⁾	1620	2630	0.6
F6	fine ⁽²⁾	1620	2630	0.6
F4	fine ⁽²⁾	1620	4100	0.4

For a given amount of sand grains in the bed, there are two constraints limiting the fluidization time. Firstly, the *voidage* decreases as precipitation proceeds until the voidage value of a fixed bed is reached ($\epsilon \sim 0.45$). Secondly, the *bed height* increases with time until it equals the height of the column. Therefore a maximum fluidization time exists which is either limited by the voidage or by the bed height.

Voidage - Figure 9a shows the simulated values of the voidage against time. The voidage in all simulations decreased slowly with time, so that a fixed bed ($\epsilon = 0.45$) only developed after times of 350 h or more. The maximum fluidization time was longer for a low shell-to-core density ratio as well as for fine sand.

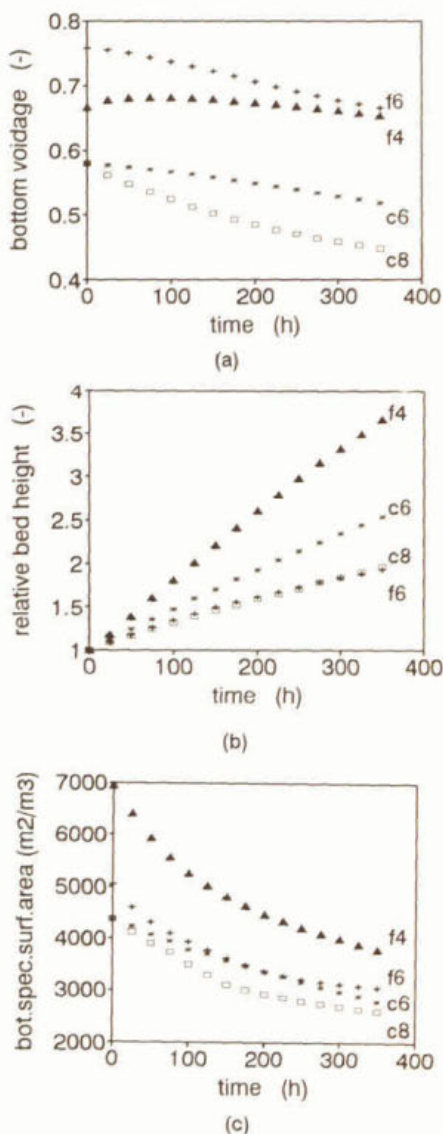


Figure 9. Simulated bottom voidage (a), relative bed height (b) and bottom specific surface area (c) as functions of the fluidization time. Codes are shown in Table IV.

Bed height - In order to be able to compare the different simulations, it was assumed that the maximum allowable bed height was twice the value just after start-up ($H/H_0 > 2$). The corresponding maximum fluidization times can be read from the plot of H/H_0 against time shown in Figure 9b. Maximum fluidization times between 100 h and 350 h were obtained, the highest values being for a high shell-to-core density ratio and for fine sand.

Therefore, the maximum fluidization time was always limited by the bed height, so that optimization of the phosphate content in the product may be achieved for high shell-to-core density ratios as well as for fine sand.

5.4.5.3 Specific surface area at the bottom layer

Phosphate removal in a fluidized bed relies on the deposition of a mineral phosphate salt upon the grains constituting the bed. Such deposition occurs by molecular growth or by aggregation of primary particles upon

the grains. Both processes only occur in the presence of supersaturation, in a small region at the bottom of the bed. If a large specific surface area ($\text{m}^2 \text{ particles} / \text{m}^3 \text{ suspension}$) is

provided for in this region, a high phosphate removal efficiency is favored. The model presented in this work allowed calculation of the specific surface area as a function of the fluidization conditions, but did not take into account the influence of the specific surface area on the phosphate removal efficiency, which was assumed to be constant.

The specific surface area is plotted against the fluidization time in Figure 9c. This figure shows that a high specific surface area was obtained when fine sand was used. A further increase in the specific surface area was obtained by using fine sand and a low density ratio.

Figure 9c also shows that the specific surface area for all simulations decreased with time. Therefore, in principle the specific surface area can also be a limiting factor for the fluidization time.

5.4.5.4 Presence of bare sand grains at the bottom of the fluidized bed

The suspension components in a fluidized bed are axially distributed according to their monocomponent bed densities, the component with the highest bed density occupying the lowest axial position. When fresh sand grains are added to a fluidized bed, they occupy the bed bottom if their bed density is higher than that of the other bed components. This situation is known to be detrimental to the precipitation process in a fluidized bed for phosphate removal: in Chapter 2 a low phosphate removal efficiency was found during start-up, where the fluidized bed was filled with bare sand grains.

Simulations (not shown) with a large number of core and shell sizes (100 to 2000 μm) and densities (1300 to 2400 $\text{kg}\cdot\text{m}^{-3}$) have indicated that, for all situations of practical interest, at least some fraction of the sand grains freshly added to the bed segregate to the bottom, as long as the shell-to-core density ratio is smaller than unity. Figure 10 shows, for the 4 simulation cases of Table III and Table IV, the mass fraction of the freshly added sand grains that segregates at the bottom as a function of the fluidization time. This fraction increased rapidly with time and then reached an almost constant value. This constant value was lower for high shell-to-core density ratios and for fine sand, the former factor being the most important one.

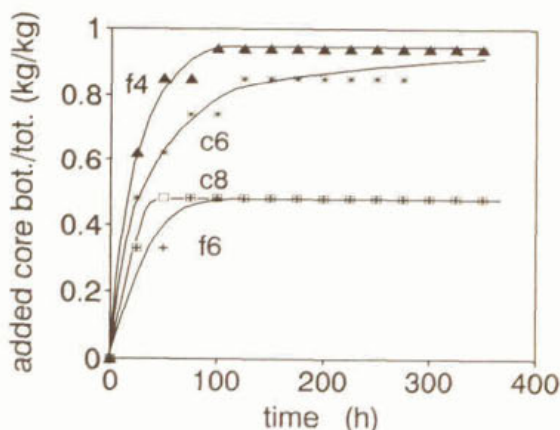


Figure 10. Fraction of sand that segregates at the bottom of the bed just after addition as a function of the fluidization time. Codes are indicated in Table IV.

The presence of bare sand at the bottom can therefore be reduced by increasing the frequency of sand grains addition (and correspondingly reducing the amount of sand added each time so that the total sand flow, and therefore the shell-to-core mass ratio, is not affected), by using fine sand as well as a high shell-to-core density ratio.

5.4.5.5 Optimum operating conditions

The operating conditions that optimize specific features of a fluidized bed for phosphate removal were described in the previous sections and are summarized in Table V. The use of fine sand is recommended since it leads to an optimization of all the features investigated. It is also recommended to keep the flow rate of sand (averaged over a large number of product removal/sand addition events) at a minimum to improve the phosphate content of the product. Frequent addition of small amounts of sand should be preferred to infrequent addition of large amounts in order to minimize the presence of bare sand at the bed bottom. Table V shows that there is no $\rho_{\text{shell}}/\rho_{\text{core}}$ which simultaneously optimize all the features studied. If the specific surface area of the grains is to be optimized, cores with a high density may be used (a low $\rho_{\text{shell}}/\rho_{\text{core}}$ results).

5.5 Conclusions

Predicted and experimentally determined voidage values for the fluidization of sand grains agreed with each other within 0.03 voidage unit, but for the fluidization of particles with a phosphate shell, the predicted porosities were 0.07 voidage unit too low.

Table V. Recommended process conditions in order to optimize specific features of the fluidized bed. ⁽¹⁾ $\rho_{\text{shell}}/\rho_{\text{core}}$ always < 1.

Feature to be optimized	Desired level	Recommended process conditions		
		core size	$\rho_{\text{shell}}/\rho_{\text{core}}$ ⁽¹⁾	other
P content in the product	high	fine	high	low core flow rate
grains spec. surface area	high	fine	low	
amount of bare sand at the bottom	low	fine	high	frequent core addition

Particle segregation always occurred in a fluidized bed for phosphate removal. It was more pronounced for sand grains with a larger spread in sizes (100-300 μm or 200-600 μm) than for sand grains with a narrow size distribution (350-420 μm). As growth of a phosphate shell developed upon the grains, partial mixing of the segregated bed layers proceeded and the bed density became independent of the axial position in the lower part of the bed.

A mathematical model was developed that describes well the experimentally determined axial particle distribution in the fluidized bed. The model takes into account the stability mechanism for segregation, but dispersion effects are neglected.

Simulations of the fluidized bed for phosphate removal have shown that cores with a small size should be used. Small grains favor a high specific surface area of the grains, enables the production of particles with a high phosphate content and minimize the amount of bare sand grains that segregate to the bottom of the bed right after their addition.

List of symbols

A	cross section of the fluidized bed, m^2
$c_{p,in}$	P concentration at the fluidized bed inlet, $kmol \cdot m^{-3}$
C_d	drag coefficient, -
d	particle diameter, m
g	gravity acceleration, $m \cdot s^{-2}$
G	linear growth rate, $m \cdot s^{-1}$
Ga	$d^3(\rho_p - \rho_f)\rho_f g / \mu^2$, Galileo number
H	bed height, m
M	solids mass, kg
mw	molecular weight, $kg \cdot kmol^{-1}$
Re	Reynolds number, -
v	settling velocity, $m \cdot s^{-1}$
v_{sup}	superficial velocity, $m \cdot s^{-1}$
v_t	terminal velocity, $m \cdot s^{-1}$

Greek letters

δ	number of P atoms in the chemical formula of the mineral phosphate
----------	---

ϵ	voidage, -
ϕ	volumetric flow rate, $m^3 \cdot s^{-1}$
μ	fluid viscosity, Pa.s
ρ	density, kg/m^3
η	P removal efficiency, -

Subscripts

bed	suspension (particle and fluid averaged)
core	particle core (sand)
f	fluid
i	suspension component
layer	mono- or multicomponent homogeneous section of a suspension in a fluid bed
p	particle (sand grain covered with shell)
shell	particle phosphate shell

References

1. Gibilaro, L.G. et al., A predictive model for the equilibrium composition and inversion of binary-solid liquid fluidized beds, *Chem. Eng. Sci.* **41**(2), p.379-387, 1986.
2. Khan, A.R. and Richardson, J.F., Fluid-particle interactions and flow characteristics of fluidized beds and settling of spherical particles, *Chem. Eng. Commun.* **78**, p.111-130, 1989.

3. Moritomi, H. et al., A comprehensive interpretation of solid layer inversion in liquid fluidised beds, *Chem. Eng. Sci.* **37**(12), p.1751-1757, 1982.
4. Patwardhan, V.S. and Tien, C., Distribution of solid particles in liquid fluidized beds, *Can. J. Chem. Eng.* **62**(1), p.46-54, 1984.
5. Patwardhan, V.S. and Tien, C., Effect of particle stratification on the performance of fluidized beds, *A.I.Ch.E. J.* **32**(2), p.321-4, 1986.
6. Richardson, J.F. and Zaki, W.N., Sedimentation and fluidization: Part I, *Trans. Instn. Chem. Eng.* **32**, p.35-53, 1954.
7. Syambal, M. and O'Brien, T.J., Simulation of granular layer inversion in liquid fluidized beds, *Int. J. Multiphase Flow* **14**(4), p.473-81, 1988.
8. van Dijk, J.C. and Wilms, D.A., Water treatment without waste material-fundamentals and state of the art of pellet softening, *J. Water S.R.T.-Aqua*, **49**(5), p.263-280, 1991.

CHAPTER 6

INFLUENCE OF HYDRODYNAMICS ON PRECIPITATION

Abstract

A method is proposed to describe the influence of hydrodynamic conditions on precipitation processes. It is based on spatially distributed moment equations, on relations for the kinetics of nucleation and growth of the precipitating compound and on the solution of the flow field as calculated by the commercially available software package 'Fluent'. Local quantities are calculated, such as liquid velocities, local supersaturation and local moments of the particle size distribution. The method was applied to simulate a double-jet continuous reactor for the precipitation of calcium phosphate. The influence of the location of feed points on the conversion, product average size and coefficient of variation of the product size distribution was shown. The conversion varied within the range of 0.57 to 0.83, the average size changed by a factor 1.9 and the coefficient of variation by a factor 1.5. It was shown that only a small fraction of the reactor volume is effectively used for nucleation and growth. The results were correlated to the fundamental processes governing the reactor behavior.

6.1 Introduction

Chemical reaction precipitation kinetics are determined by a combination of interrelated processes. Reactants are brought together by mixing. During the mixing process supersaturation is created, which is the driving force for nucleation, growth and aggregation. The produced aggregates can either break or further aggregate by action of shear stresses in the liquid phase. Crystals and aggregates collide with each other, with impellers and the reactor walls, so enhancing crystal breakage. Crystal dissolution occurs in regions of negative supersaturation.

When the timescale of mixing is of the same order of magnitude as the timescales of crystal growth, nucleation or aggregation, local characteristics of the system largely determine the overall system behavior.

In the last few years, with the development of more and more powerful computers and of better numerical methods, it became feasible to describe spatially distributed processes in chemical engineering. Homogeneous reaction systems in reactors of any arbitrary geometry can nowadays be described by using commercially available software. However, up to now no spatially distributed description of precipitation processes is available.

In this study a first attempt was made to develop a mathematical model for precipitation processes, which takes into account local system characteristics. Outputs of the model are the spatially distributed moments of the particle size distribution and local supersaturation. The model was applied to the precipitation of calcium phosphate in a continuous double jet reactor at varying location of the feed points. Calcium phosphate presents high conversion rates and is prone to aggregation, being therefore sensitive to local system characteristics. Calcium phosphate precipitation also has a practical significance, since it is used on an industrial scale to remove phosphate from waste waters [10].

The proposed model is a useful tool to improve the understanding of precipitation processes. The model can be applied in the design and optimization of crystallizers, since it can easily be adapted to different crystallizer geometries. Furthermore the formation of undesired crystal phases or morphologies due to too high local supersaturation levels can be predicted. In this first attempt the nucleation and growth kinetics, the solution chemistry as well as macromixing are considered. However, aggregation, breakage, micromixing, turbulent diffusion and particle dissolution in zones of undersaturation have been neglected.

6.2 Mathematical model

6.2.1 General model description

Calcium phosphate precipitation is accomplished by mixing an aqueous solution containing calcium chloride and phosphoric acid with an aqueous sodium hydroxide solution in a double jet reactor at steady state in the turbulent regime. The laws of conservation of mass, momentum and chemical species are applied to each infinitesimal volume element in the

reactor to describe the behavior of the liquid phase. In a similar way, laws of conservation of number, length, surface and volume (moment equations) are applied to characterize the solid phase. Liquid phase and solid phase information are connected through the kinetics of precipitation. Figure 1 shows a block diagram of the model structure. The commercially available software 'Fluent' was used to solve the resulting set of partial differential equations. 'Fluent' uses a finite volume procedure in the Eulerian frame of reference. Tensor notation [9] is used throughout the text.

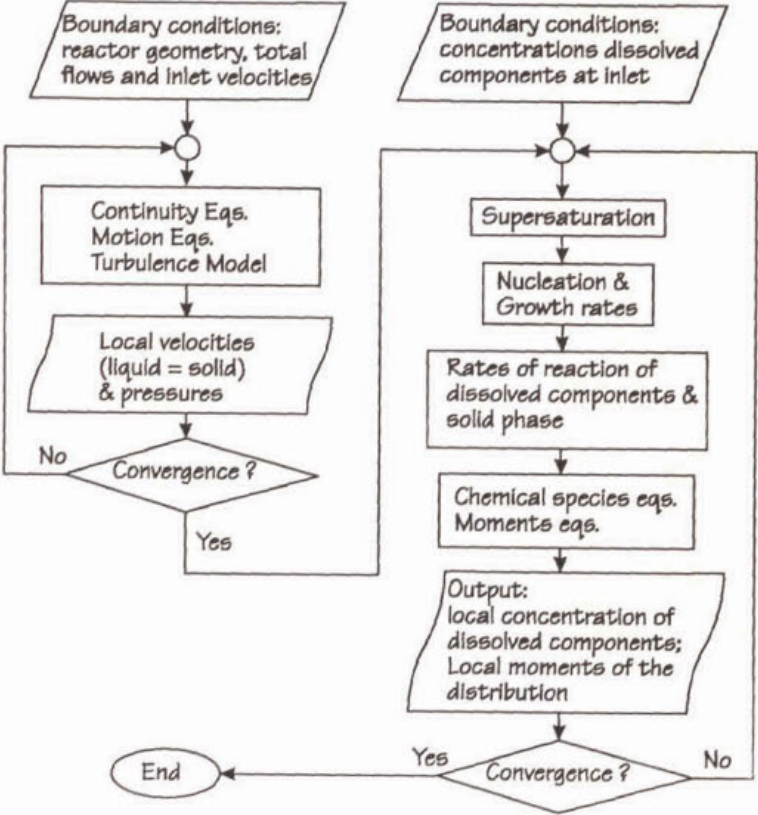


Figure 1. Block diagram of the mathematical model for precipitation processes.

6.2.2 Assumptions

It is assumed that the solids concentration is small, so the presence of solids does not affect the flow field. The particles have a small diameter, so they follow the streamlines of the flow

field. The residence time is not very large so sedimentation effects can be neglected.

The model was developed for turbulent flow at steady state conditions. The closure model adopted (k - ϵ model) requires isotropic turbulence. Application to laminar flows is also possible, since this type of flow can be considered as a special case of the turbulent flow.

The kinetics of precipitation include primary nucleation and surface integration controlled linear growth rate, the latter with a second order dependency on supersaturation. The linear growth rate is taken to be independent of particle size. Aggregation and breakage, as well as dissolution of the particles in zones of negative supersaturation are neglected. Micromixing times are assumed to be infinitesimally small, i.e., no local segregation of dissolved components is encountered.

It is also assumed that chemical reactions between ions and complexes in solution are very fast, so the liquid phase is in chemical equilibrium. Ion activity coefficients are assumed to be constant throughout the vessel.

6.2.3 Conservation of mass and momentum

The laws of conservation of mass and momentum, applied to the liquid phase in the reactor, determine the flow field, i.e. the local liquid phase velocities and pressures. These conservation laws are mathematically expressed in terms of the three-dimensional time-smoothed equations of continuity and motion [1,9],

$$\frac{\partial \bar{u}_i}{\partial x_i} = 0 \quad (1)$$

$$\frac{\partial \rho \bar{u}_i \bar{u}_j}{\partial x_i} - \frac{\partial}{\partial x_i} \left[\mu \left(\frac{\partial \bar{u}_i}{\partial x_j} + \frac{\partial \bar{u}_j}{\partial x_i} \right) \right] - \frac{\partial \bar{P}}{\partial x_j} + \rho g_j - \frac{\partial \rho \bar{u}_i' u_j'}{\partial x_i} \quad (2)$$

where the overline and the prime indicate respectively the time-averaged and the fluctuating

component of a variable. The last term in eq.(2) concerns the so-called 'Reynolds stresses', $-\overline{\rho u_i' u_j'}$, which in the program 'Fluent' are related to time-averaged flow quantities by means of the k- ϵ turbulence model [6,9].

6.2.4 Conservation of chemical species in solution

The law of conservation of mass is applied to the chemical species k in the liquid phase in order to describe local concentrations [1,9],

$$\frac{\partial \overline{\rho u_i X_k}}{\partial x_i} - \frac{\partial (-\overline{\rho u_i' X_k'})}{\partial x_i} + \frac{\partial}{\partial x_i} (\rho D_k \frac{\partial \overline{X_k}}{\partial x_i}) + \overline{R_k} + R_k' \quad (3)$$

The term $-\overline{\rho u_i' X_k'}$ in eq.(3) represents the turbulent transport of mass and has to be related to time-averaged chemical species concentrations or their gradients if eq.(3) is to be solved. A semi-empirical approach is adopted [1] based on an analogy with Fick's law of diffusion,

$$-\overline{\rho u_i' X_k'} = \frac{\mu_t}{Sc_{kt}} \frac{\partial \overline{X_k}}{\partial x_i} \quad (4)$$

$$Sc_{kt} = \frac{\mu_t}{D_{kt} \rho} \quad (5)$$

The turbulent viscosity (μ_t) is calculated from the k- ϵ turbulence model and the corresponding turbulent Schmidt number of the chemical species k (Sc_{kt}) is assumed to be 1000 for all the chemical species. The production term ($\overline{R_k}$) is connected to the precipitation kinetics and is given in section 2.6. As a first approximation the fluctuating component R_k' is neglected. The term in eq.(3) which represents the molecular or ion diffusivity is also neglected since this term is usually much smaller than the turbulent transport term. For the system studied here, the chemical species involved are calcium, phosphate, sodium and chloride.

6.2.5 Moments of the particle size distribution

The local particle size distribution is characterized by means of the moment equations [4,8],

$$\frac{\partial u_i m_0}{\partial x_i} - J = 0 \quad (6)$$

$$\frac{\partial u_i m_p}{\partial x_i} - p m_{p-1} G = 0, \quad p=1,2,\dots \quad (7)$$

where m_p is the p^{th} moment of the distribution ($p=0,1,2,\dots$) and $i=1,2,3$ are the directions in cartesian coordinates. The moments of the distribution are directly related to properties of the distribution, such as total number (N), length (L), area (A) and mass fraction of particles (X_{cryst}),

$$N = m_0; \quad L = m_1; \quad A = k_a m_2; \quad X_{\text{cryst}} = k_v \rho_{\text{cryst}} m_3 / \rho \quad (8)$$

Since the third moment and the solids mass fraction are directly related, the third moment equation (eq.(7) with $p=3$) expresses the conservation of mass of the solid phase. It is analogous to the chemical species conservation equation (eq.(3)), which was applied earlier for the liquid phase.

Also the mean size and the coefficient of variation of the particle size distribution (both number based) can be calculated from the moments of the distribution,

$$d_{\text{avg}} = m_1/m_0; \quad \text{c.v.} = (m_0 m_2 / m_1^2 - 1)^{1/2} \quad (9)$$

The derivatives with respect to x_i in eqs.(6) and (7) represent the convective transport of moments. The term J expresses the local changes in m_0 due to nucleation and the term $p m_{p-1} G$ expresses the local changes in m_p due to crystal growth. The boundary conditions for eqs.(6) and (7) are zero flux of moments through the reactor walls.

By splitting the moments and the linear growth rate in eqs.(6) and (7) into a mean and a

fluctuating component and by subsequent time-averaging, the following expressions are obtained,

$$\frac{\partial \overline{u_i m_0}}{\partial x_i} - \overline{J} - \overline{J'} - \frac{\partial(-\overline{u_i' m_0'})}{\partial x_i} = 0 \quad (10)$$

$$\frac{\partial \overline{u_i m_p}}{\partial x_i} - p \overline{m_{p-1} G} - \frac{\partial(-\overline{u_i' m_p'})}{\partial x_i} - p \overline{m_{p-1}' G'} = 0 \quad (11)$$

Averaging procedures related to turbulent flows can be found in the references [1] and [3]. The terms $\partial(-\overline{u_i' m_p'})/\partial x_i$ in eqs.(10) and (11) represent the convective transport of the p^{th} moment along the x_i axis due to fluctuations in the turbulent field. The terms $\overline{J'}$ and $p \overline{m_{p-1}' G'}$ represent the production of m_p due to turbulence. They have to be related to the time-averaged moments of the distribution or their gradients if eq.(10) and eq.(11) are to be solved. However, these terms are not known in general, so that a so-called closure problem results. In analogy with the approach used for the conservation of chemical species, it can be taken that

$$-\overline{u_i' m_p'} = \frac{\mu_t}{Sc_{pt}} \frac{\partial \overline{m_p}}{\partial x_i} \quad (12)$$

The particles are assumed to have the same local velocity as the liquid phase and to have a turbulent Schmidt number equal to that of the dissolved species ($Sc_{pt} = 1000$). As a first approximation the terms $\overline{J'}$ and $p \overline{m_{p-1}' G'}$ in eq.(10) and eq.(11) are simply neglected.

Equations (10) to (12) form a closed set in terms of the moments $\overline{m_p}$. They are of the same dimensionality as the mass and momentum transport equations and can be numerically solved in a similar way. The number of moment equations can be chosen according to the amount

and type of information required from the particle size distribution. Here it is considered that the number based average size and coefficient of variation give an adequate description of the PSD, so it is sufficient to use the first 4 moments of the distribution ($p=0..3$). The minimal number of moment equations is 3 ($p=0..2$) because the second moment is needed to calculate the rate of precipitation (section 6.2.6).

6.2.6 Precipitation kinetics

Chemical reaction precipitation from aqueous solutions can often be described with a chemical reaction as shown in eq.(13). The supersaturation (β) with respect to the solid phase formed, the primary nucleation rate (J) and the linear growth rate (G) can be expressed by eqs.(14) to (16).



$$\beta = \frac{1}{m+n} \ln \frac{(A^{n+})^m (B^{m-})^n}{K_s} \quad (14)$$

$$J = k_{J1} \exp\left(-\frac{k_{J2}}{\beta^2}\right) \quad (15)$$

$$G = \frac{dL}{dt} = k_{G1} \beta^{k_{G2}} \quad (16)$$

The expressions (A^{n+}) and (B^{m-}) in eq.(14) refer to the activities of the free ions in solution. The above equations are applied to the precipitation of calcium phosphate. The process conditions are such that the modification formed is an amorphous calcium phosphate phase with a chemical formula consistent with that of tricalcium phosphate ($\text{Ca}_3(\text{PO}_4)_2$). The solubility of calcium phosphate and the kinetic parameters in eqs.(13) to (16) were estimated from the experimental data in Chapter 4 and are given in Table I.

In order to calculate the supersaturation the activities of the free ions Ca^{2+} and PO_4^{3-} at every

position in the reactor are needed. A mathematical model of the solution chemistry was therefore developed based on mass balances, chemical equilibrium relations and electroneutrality in the liquid phase (Chapter 2). Chemical equilibrium in

Table I. Solubility and kinetic parameters for the precipitation of calcium phosphate. S.I. units.

A^{n+} :	Ca^{2+}	k_{J1} :	10^{35}
B^{m-} :	PO_4^{-3}	k_{J2} :	300
K_s :	10^{-28}	k_{G1} :	10^{-9}
k_{G2} :	2		

Note: the values above differ from those in Chapter 4. Although the data in Chapter 4 is more accurate, both sets of parameters agree with the experimental data. The different value for K_s is compensated by the rate parameters for nucleation and growth.

the liquid phase is assumed, inputs are the local analytical chemical species concentrations (X_{Ca} , X_{PO4} , X_{Na} and X_{Cl}) and outputs are the local activities of all ions and complexes in solution. The model consists of a set of non-linear equations that is solved by the multi-variable method of Newton-Raphson at each location in the reactor. The activity coefficients are calculated from the Davies equation [2] for an ionic strength of 0.0135 M, and are assumed to be constant throughout the reactor.

For undersaturated regions in the reactor ($\beta < 0$) the linear growth rate is set to zero, i.e., no particle dissolution occurs. For the configurations tested in this paper this turned out to be a reasonable assumption because the undersaturated regions either had a very low solids concentration or were so small that the residence time of the particles in these regions were negligible.

Simulations with the chemical equilibrium model show that high Na^+ and low Cl^- concentrations (i.e. high OH^-) favor large values for the activity of PO_4^{3-} ions in eq.(14). Therefore, although the ions Na^+ and Cl^- do not participate in the precipitation reaction, they affect the supersaturation indirectly, through their effect upon the concentration of the PO_4^{3-} ions.

The production rate of calcium phosphate particles (R_{cryst} , eq.(17)), is calculated from the local linear growth rate (eq.(16)) and from the local surface area available for growth (eq.(8) and eq.(11) with $p=2$). The production rate of the chemical species calcium and phosphate

in the liquid phase (R_{Ca} and R_{PO_4} , negative quantities in eq.(18) and eq. (19)) are related to R_{cryst} by the stoichiometry of the chemical reaction (eq.(13)). The reaction rate for the chemical species sodium and chloride is simply zero (eq.(20)) since they do not participate in the precipitation reaction.

$$R_{cryst} = 3 (k_v/k_a) \rho_{cryst} G A \quad (17)$$

$$R_{po_4} = - 2 (mw_{po_4}/mw_{cryst}) R_{cryst} \quad (18)$$

$$R_{ca} = - 3 (mw_{ca}/mw_{cryst}) R_{cryst} \quad (19)$$

$$R_{Na} = R_{Cl} = 0 \quad (20)$$

The kinetics of precipitation affect the local composition of both the liquid and solid phase: the rates of production of the chemical species calcium and phosphate (R_{Ca} and R_{PO_4}) are inserted into the chemical species conservation equation (eq.(3)), and the linear growth rate (G) is present in the equation for conservation of the p^{th} moment of the distribution (eq.(11)).

6.3 Simulation conditions

Calcium phosphate precipitation was achieved by adding two reactant streams via two separate inlets into the continuous reactors indicated in Figure 2. The reactants are two undersaturated aqueous solutions, one containing calcium chloride and phosphoric acid (introduced through the P inlet) and the other sodium hydroxide (introduced through the NaOH inlet). The reactor geometry was chosen so that a two-dimensional flow resulted, thus simplifying the analysis of the results. No mixing device was present.

Three reactor configurations were studied, where the positions of the Na and P inlets were varied as indicated in Figure 2a,b and c. In order to evaluate how these 3 reactor configurations differ in performance from ideal reactors, the extreme cases represented by a plug flow reactor (PFR) and a mixed suspension mixed product removal reactor (MSMPR) were also studied. The PFR and the MSMPR were assumed to be perfectly micromixed. A

mathematical model for the PFR was obtained by solving the above presented model for a one-dimensional reactor with premixed feed. A separate model for the MSMPR was built, based on the moment equations as described in ref. [8] coupled with the kinetics of precipitation of calcium phosphate. The physical properties and process conditions used in all simulations are shown in Table II and Table III respectively.

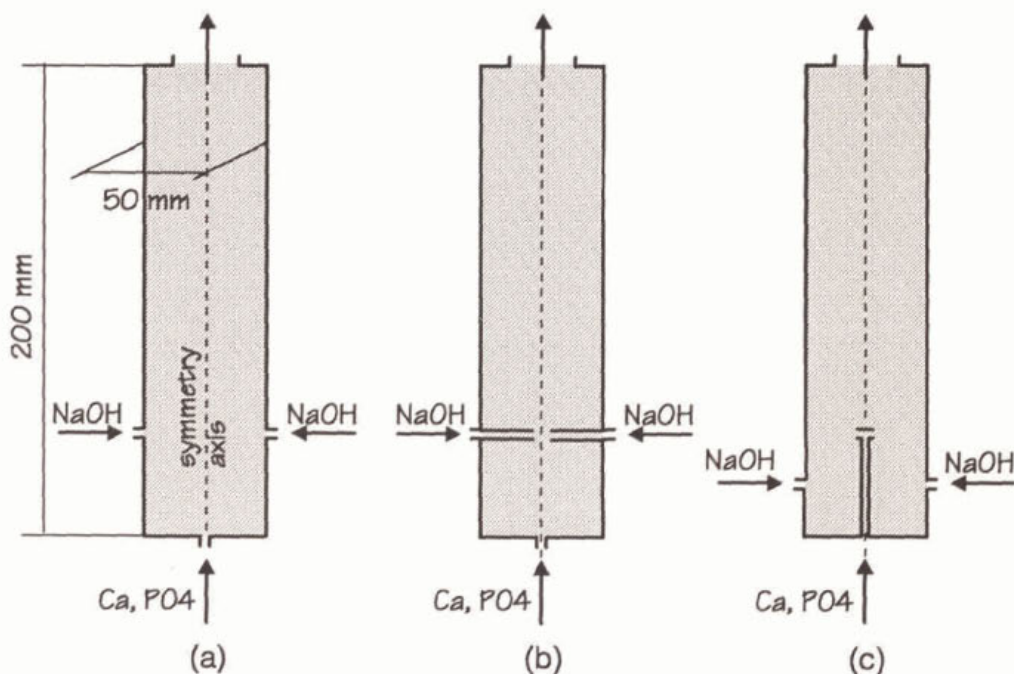


Figure 2 Reactor geometry: (a) Na inlet at the wall (configuration 1); (b) Na inlet at the center (configuration 2); (c) Na inlet at the wall and horizontal P inlet (configuration 3).

6.4 Simulation results and discussion

6.4.1 Introduction

Analysis of the simulation results is made in three steps. In section 6.4.2 the main features of each reactor configuration are presented by analyzing graphically the model outputs, i.e., local process variables such as supersaturation, solids concentrations, particle size, etc. In section 6.4.3 quantitative criteria for a comparison of reactor performances are established.

Table II- Physical properties.

suspension viscosity	μ	0.0009	$\text{kg}\cdot\text{m}^{-1}\cdot\text{s}^{-1}$
suspension density	ρ	1000	$\text{kg}\cdot\text{m}^{-3}$
crystal density	ρ_{cryst}	2400	$\text{kg}\cdot\text{m}^{-3}$
turbulent Schmidt nr.	Sc_t	1000	-
shape factor for area	k_a	3.1416	-
shape factor for volume	k_v	0.5236	-

Table III- Process conditions. ⁽¹⁾ configurations 1 and 2; ⁽²⁾ configuration 3. Total flow is the same for all simulation cases.

Variable unit		Configurations 1, 2, 3		MSMPR and PFR
		P inlet	Na inlet	single inlet
Xca	$\text{kg}\cdot\text{kg}^{-1}$	$1.93\cdot 10^{-4}$	0	$1.89\cdot 10^{-4}$
XPO4	$\text{kg}\cdot\text{kg}^{-1}$	$1.52\cdot 10^{-4}$	0	$1.49\cdot 10^{-4}$
XNa	$\text{kg}\cdot\text{kg}^{-1}$	0	$5.52\cdot 10^{-3}$	$1.14\cdot 10^{-4}$
XCl	$\text{kg}\cdot\text{kg}^{-1}$	$3.41\cdot 10^{-4}$	0	$3.34\cdot 10^{-4}$
inlet half-size	m	$1.67\cdot 10^{-3}$ ⁽¹⁾	$5.26\cdot 10^{-3}$	-
		$5.26\cdot 10^{-3}$ ⁽²⁾	-	-
inlet veloc.	$\text{m}\cdot\text{s}^{-1}$	0.3 ⁽¹⁾	0.02	-
		0.0952 ⁽²⁾	-	-
temperat.	K	298	298	298

The utilization of reactor space in relation to individual processes is expressed in terms of characteristic volume fractions. In section 6.4.4 the conversion, the product size and coefficient of variation are evaluated due to their practical relevance. The conversion reflects how efficiently the raw materials are used, while the average product size and the width of the product size distribution are important e.g. for downstream treatment. Besides, since measurement of local properties in the reactor is often very difficult, experimental validation of the model based on product characteristics and conversion is a simple alternative.

6.4.2 Local properties

Randolph and Larson [8] have shown that in general crystallization and precipitation processes exhibit a feed-back mechanism with the supersaturation acting as the controlling

variable. A second feed-back loop exists due to recirculation streams within the reactor. It is therefore difficult, if not impossible, to analyze the simulation results in terms of unambiguous cause-effect processes. Therefore, only a few features of the precipitation process will be presented in order to illustrate the interactions between individual processes.

The local values of selected variables obtained in the simulations of the reactor configurations 1 to 3 are shown in Figure 3 to Figure 5. The highest values of the variables in the reactor are also indicated in the figures. The left half of the reactor cross sections are given (the vertical lines at the right side are symmetry axes). The reactor dimensions are out of scale, the reactor width being enlarged by a factor 4 to facilitate visualization.

6.4.2.1 Configuration 1: Na inlet at the wall

The liquid phase velocity field in the reactor (Figure 3a) is strongly influenced by the jet stream coming from the P inlet (calcium phosphate solution). The flow coming from the Na inlet (sodium hydroxide solution) represents only a marginal contribution to the total flow, so it hardly affects the flow field. A recirculation stream occupies the lower part of the reactor. Fluid elements in this stream experience an increased residence time.

The concentration of the NaOH solution can be followed through the spatial distribution of sodium ions in the reactor. Since the sodium ions are not incorporated in the precipitate, their distribution in the reactor also allows visualization of the mixing patterns irrespective of the precipitation process, as indicated in Figure 3b. The sodium ions entering the reactor follow the streamlines of the recirculation stream and travel towards the symmetry axis via the reactor bottom. When they reach the region close to the P inlet they have already mixed with the surroundings to such an extent that the sodium ion concentration is already reduced to one tenth of its value at the inlet. The sodium and thus the hydroxide ions hardly mix with the center of the phosphate jet stream, so some phosphate is expected to leave the system unreacted due to a pure macromixing limitation.

Figure 3c shows the distribution of supersaturation throughout the reactor. Only 28% of the reactor volume has a non-negligible supersaturation (taken for convenience as $\beta > 0.3$). It is within these 28% that most of the nucleation and growth will occur (see also section 6.4.3).

This small volume however, includes sub-regions with very high supersaturations (up to $\beta = 3.0$).

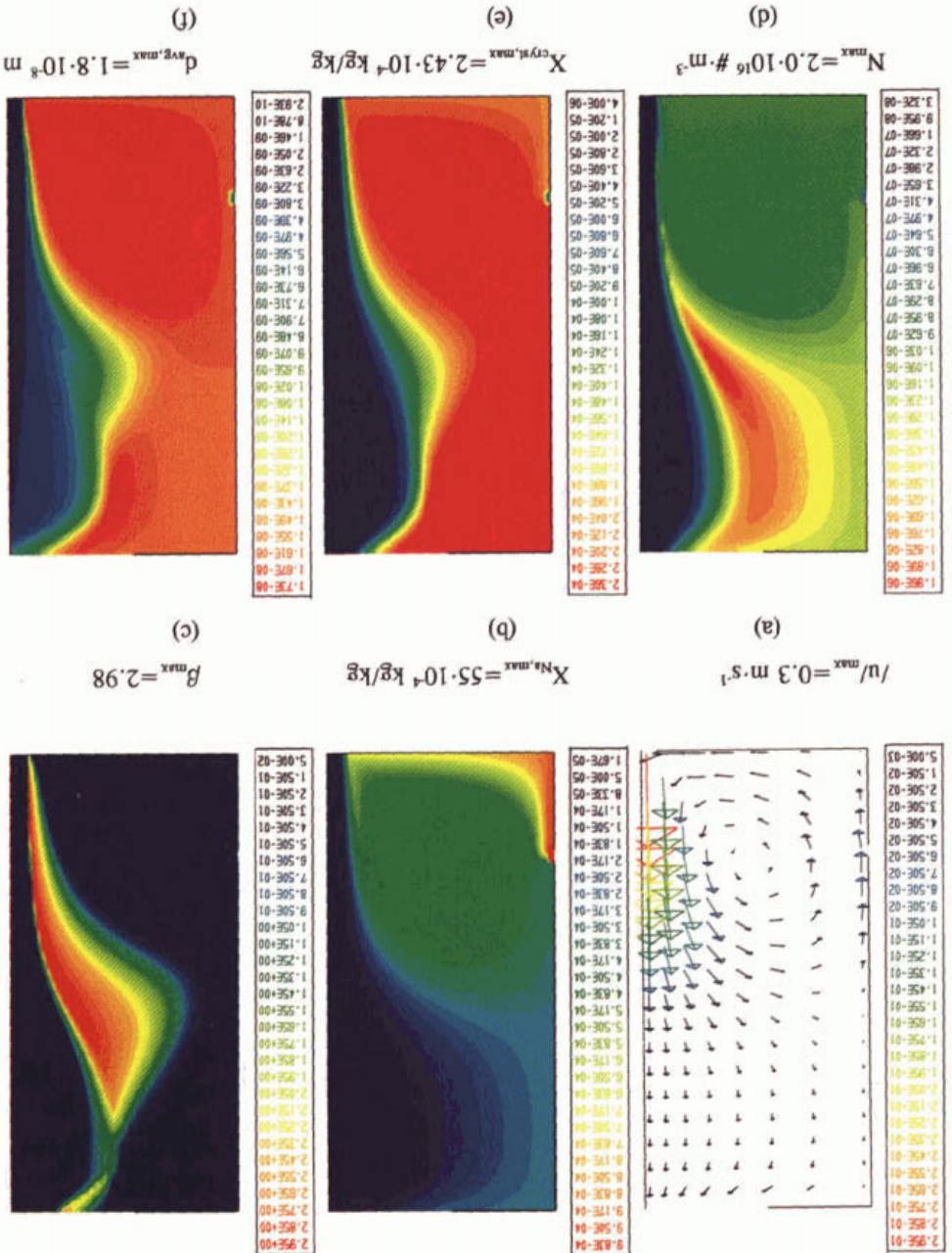
In various precipitating systems, the value of the supersaturation also determines the modification which is formed. By knowing the local supersaturation values, the formation of undesirable phases can be predicted from solubility data of the modifications that may potentially precipitate and from the Ostwald rule of stages [5]. This rule states that the first modification to be formed is the one having the highest solubility. For the precipitation of calcium phosphate from aqueous solutions at least 5 different modifications can be formed [7]. By applying Ostwald's rule to the reactor configuration 1 it is understandable that in regions of high supersaturations ($\beta > 2.9$) with respect to amorphous calcium phosphate, this phase will indeed be formed first. In principle, precipitation of other phases can occur in zones of negative supersaturation with respect to the amorphous modification, but the supersaturations with respect to the other modifications are small and their precipitation kinetics are relatively slow, so the formation of other modifications can be neglected.

The particle number concentration (N in eq.(8)) is the largest in the region of high nucleation rate and right above it (Figure 3d): the nuclei generated in the region of high supersaturation are subsequently transported by convection in the direction of the flow (upwards). Turbulent diffusion and the recirculating stream distribute the particles over the whole reactor. The particles grow while this happens so the upper part of the reactor and the recirculation zone contain the largest mass fraction of solids (Figure 3e) and the largest average particle sizes (Figure 3f).

6.4.2.2 Configuration 2: Na inlet at the center

The velocity field (Figure 4a) resembles that of configuration 1 (Figure 3a). In this case, however, the sodium hydroxide entering the reactor meets the jet from the P inlet straight away, so no pre-dilution occurs, as was the case in configuration 1. The mixing of the sodium and hydroxide ions with the phosphate jet is more efficient here, as can be seen from the sudden drop in sodium ions concentration right above its inlet (Figure 4b). Therefore, the loss of unreacted phosphate due to a macromixing limitation is expected to be less pronounced here.

Figure 3. Configuration 1: velocity vectors (a), sodium ions mass fraction (b), supersaturation (c), particle number concentration (d), solids mass fraction (e) and number averaged particle size (f).



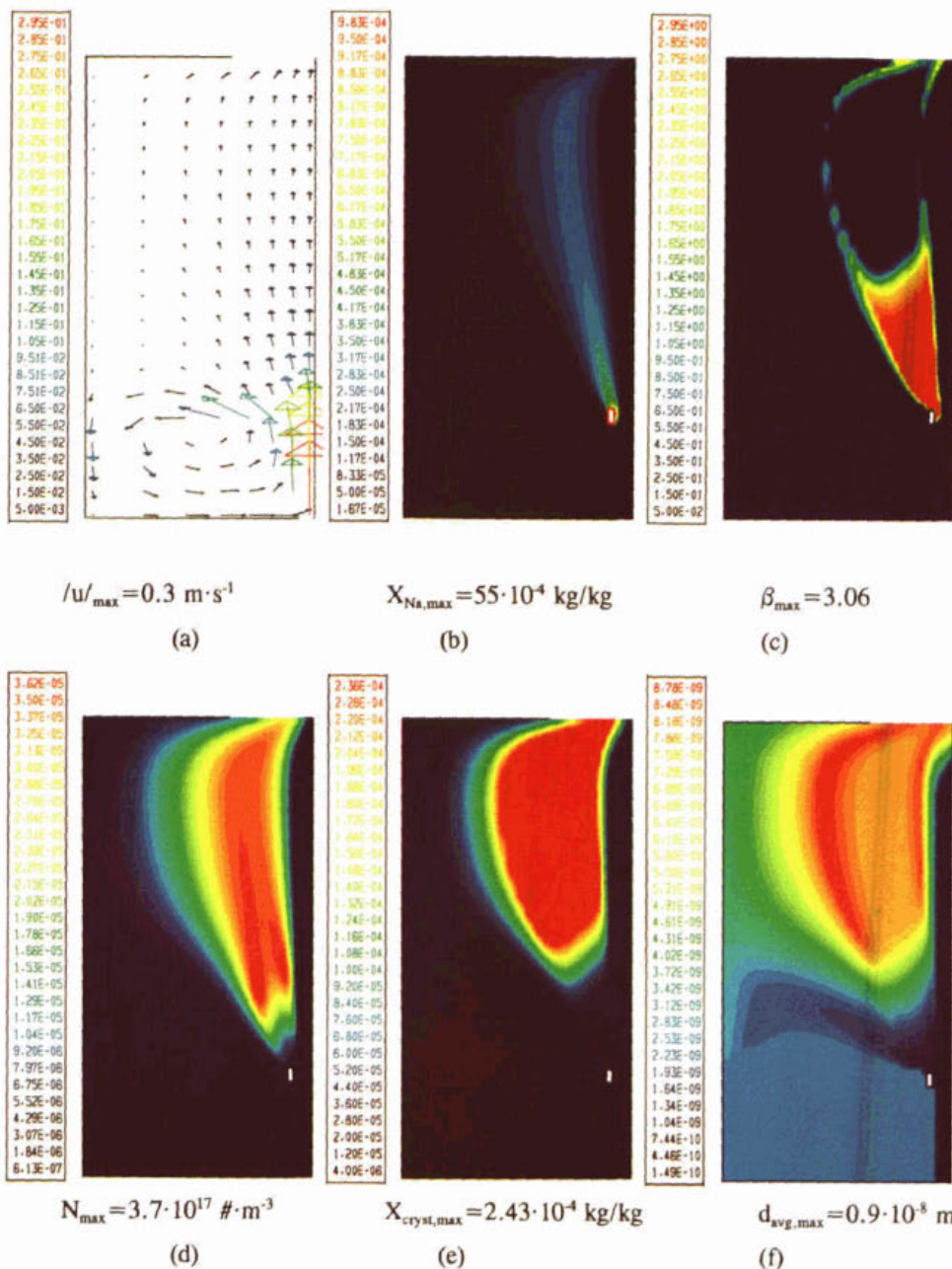
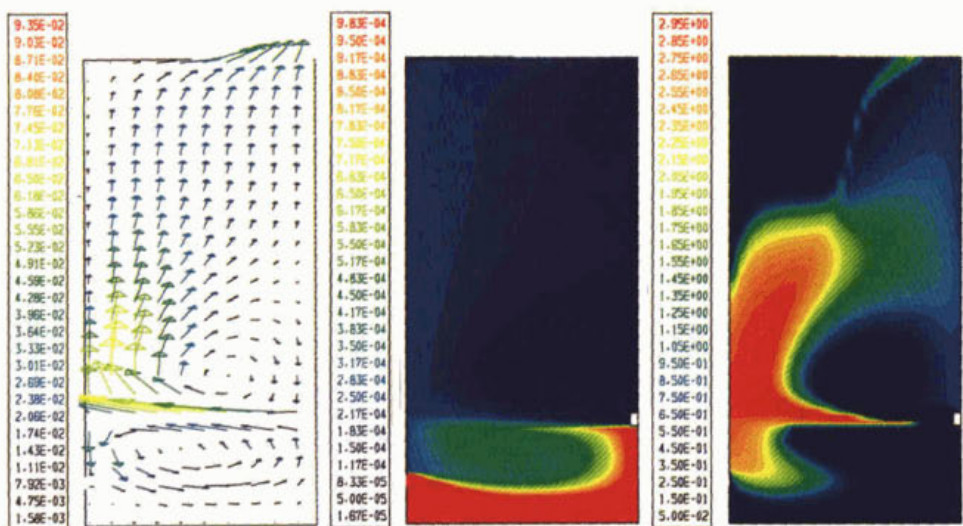


Figure 4. Configuration 2: velocity vectors (a), sodium ions mass fraction (b), supersaturation (c), particle number concentration (d), solids mass fraction (e) and number averaged particle size (f).



$$/u_{\max}=0.1 \text{ m}\cdot\text{s}^{-1}$$

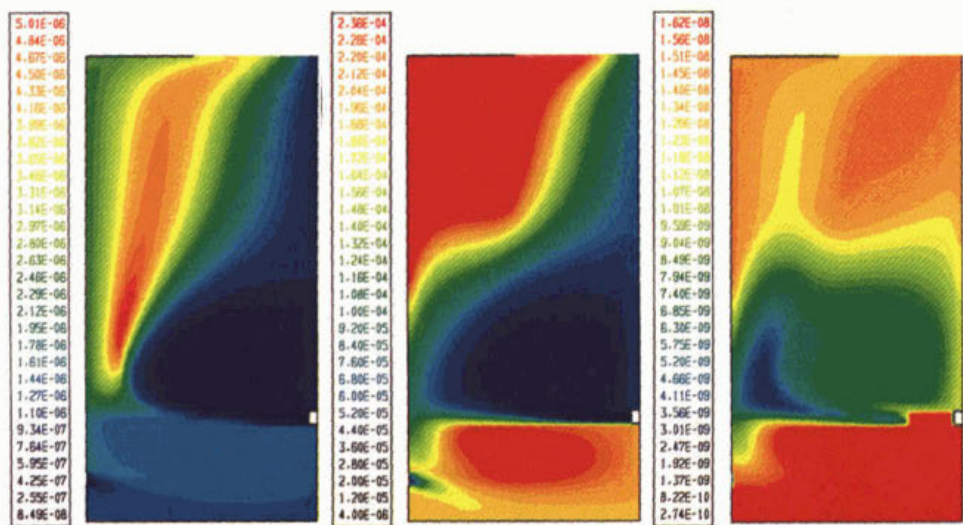
(a)

$$X_{Na,max}=55\cdot 10^{-4} \text{ kg/kg}$$

(b)

$$\beta_{\max}=3.00$$

(c)



$$N_{\max}=5.1\cdot 10^{16} \text{ \#}\cdot\text{m}^{-3}$$

(d)

$$X_{cryst,max}=2.43\cdot 10^{-4} \text{ kg/kg}$$

(e)

$$d_{avg,max}=1.6\cdot 10^{-8} \text{ m}$$

(f)

Figure 5. Configuration 3: velocity vectors (a), sodium ions mass fraction (b), supersaturation (c), particle number concentration (d), solids mass fraction (e) and number averaged particle size (f).

Due to the rapid mixing of sodium hydroxide, a high supersaturation results right above the Na inlet (Figure 4c). The conversion (a combined effect of nucleation rate, growth rate and surface available for growth) proceeds faster than in configuration 1, leading to a fast drop in the supersaturation. The volume fraction with a non-negligible supersaturation ($\beta > 0.3$) is then only 14%.

The particle number concentration N (Figure 4d) and the solids concentration X_{cryst} (Figure 4e) are the highest in the zone of high supersaturation and just above it, in analogy to configuration 1. Here however, almost no particles are entrapped in the recirculation stream (N and X_{cryst} attain low values), so this region can be regarded as a dead zone.

6.4.2.3 Configuration 3: horizontal P inlet positioned above Na inlet

The velocity field (Figure 5a) shows two recirculation zones, one above, the other below the phosphate jet (the P inlet). The sodium hydroxide stream entering the reactor is pre-diluted in the lower recirculation zone before it reaches the phosphate jet (Figure 5b), just as in configuration 1. Loss of unreacted phosphate because of short circuiting is likely to be small due to the horizontal orientation of the phosphate jet stream.

Pre-dilution of the sodium hydroxide combined with a low phosphate loss by short circuiting results in a distribution of the supersaturation over a large reactor volume. The zone with non-negligible supersaturation ($\beta > 0.3$) is much larger than in configurations 1 and 2 (60%).

The particles produced in the zone of non-negligible supersaturation ($\beta > 0.3$) are transported partly to the lower recirculation zone and partly to the outlet stream. The upper recirculation zone hardly contains any particles (Figure 5d) and can be regarded as a dead zone.

The largest particles are found in the lower recirculation zone, probably due to the large residence time at a non-negligible supersaturation ($\beta > 0.3$) in parts of this zone.

6.4.3 Utilization of the reactor space

The spatially distributed description of processes offers the possibility of identifying zones

within the reactor where specific processes occur. The location and size of these zones will be further elaborated here, taking as examples the processes of nucleation and growth.

The rate of production of a number of particles at a given elementary volume within the reactor (in #/s) is given by the product of the local nucleation rate J and the elementary volume. Zones of high nucleation rate (i.e. of high supersaturation , see eq. (14)) are therefore those which contribute most to the total generation of new particles in the reactor. In order to quantify the total size of these zones, a variable $V_{J,90}$ is defined as the volume of the zone responsible for the production of 90% of the total number of particles generated in the reactor as a whole.

Table IV shows that, for the 3 configurations studied, nucleation occurs in 1 to 3% of the total reactor volume. These zones correspond to the regions of $\beta > 2.9$ in Figure 3a to Figure 5a. By improving mixing conditions (e.g. by increasing turbulence), it should in principle be possible to increase $V_{J,90}$ from the present values, which are close to that of the PFR (4%), up to values around those of an MSMPR (90%).

Table IV - Utilization of reactor volume with respect to production of crystal number ($V_{J,90}$) and mass ($V_{R,90}$).

System Config.	Conf. 1	Conf. 2	Conf.3	MSMPR	PFR
$V_{J,90}$ (-)	0.013	0.022	0.032	0.900	0.047
$V_{R,90}$ (-)	0.17	0.06	0.24	0.900	0.103

The production of particle mass in any given reactor elementary volume can be analyzed similarly: zones with high R_{crist} contribute most to the total mass production rate in the reactor. The total volume of these zones are quantified by defining a variable $V_{R,90}$ as the volume of the sub-region where 90% of the total particle mass is produced.

Zones of high R_{crist} (see eq.(17)) result either from high growth rates (and therefore high supersaturation, eq.(16)), or from a high surface area of particles available for growth, or

from both. For the 3 configurations, the zones of non-negligible R_{cryst} (taken for convenience as those in which $R_{\text{cryst}} > 0.1 R_{\text{cryst,max}}$) coincide with the zones of non-negligible supersaturation ($\beta > 0.1 \beta_{\text{max}} = 0.3$), showing that β is the limiting factor. Table IV shows that only 6 to 24% of the reactor volume is utilized for production of particle mass in configurations 1 to 3. For the PFR a similar figure is found ($V_{R,90} = 10\%$). This is a consequence of the high supersaturation at the reactor inlet (premixed feed), which accelerates the nucleation and growth processes, thus causing the rate of production of particles to increase. The similarity between $V_{R,90}$ in the PFR and in configurations 1 to 3 indicate that the just described local mechanism is also present in configurations 1 to 3. In these cases, however, the location and size of the reactive zone varies with the location of the feed streams. If local effects are eliminated (e.g. by a higher local turbulence or by diluting the reagents), values of $V_{R,90}$ up to 90%, the MSMR value, can in principle be obtained.

6.4.4 Conversion, product size and coefficient of variation.

The conversion (ξ), the average product size (d_{prod}) and the coefficient of variation of the product size distribution ($(\text{c.v.})_{\text{prod}}$) for the 3 configurations, for the PFR and the MSMR are analyzed in this section. The simulation results are summarized in Table V.

6.4.4.1 Conversion

The conversion (ξ) is defined as the ratio between the phosphate flow which leaves the reactor as a precipitate and the total phosphate flow introduced in the reactor. The former is calculated from the local solids concentrations and the corresponding flow rates at the reactor outlet. The latter is obtained from the composition and the flow rate of the inlet phosphate stream. The following relation is thus obtained,

$$\xi = \frac{\int_S k_v \rho_{\text{cryst}} m_3 v_z dS}{\rho_1 d_1 v_1 X_{\text{PO}_4,1} (1/2) (mw_{\text{cryst}} / mw_{\text{PO}_4})} \quad (21)$$

where S is the surface of the two-dimensional reactor outlet and v_z is the fluid velocity in the

z-direction (normal to S). The index 1 refers to the reactor P inlet. The maximum theoretical conversion for the process conditions used in this study was 0.998, the remaining 0.002 represents the solution in equilibrium with the solids.

Table V - Averaged properties at the reactor outlet for the 3 reactor configurations, MSMPR and PFR. $d_{prod,PFR} = 7 \times 10^{-9}$ m.

Reactor Config.	Conf. 1	Conf. 2	Conf. 3	MSMPR	PFR
ϵ (-)	0.57	0.72	0.83	0.93	1.00
$d_{prod}/$ $d_{prod,PFR}(-)$	2.3	1.2	2.1	10.0	1.0
$(c.v.)_{prod}(-)$	2.4	1.6	1.7	1.0	1.5

The lowest conversion is found when the sodium hydroxide stream is added at the reactor wall ($\xi=0.57$, configuration 1). Due to the axial orientation of the P inlet, some phosphate leaves the reactor before mixing with the sodium hydroxide stream. When sodium hydroxide is added directly into the phosphate jet the conversion increases ($\xi=0.72$, configuration 2), since the mixing of the two inlet streams improves, but the residence time of the phosphate jet stream is still too short to provide a high conversion. When a horizontal orientation of the P inlet is applied, the conversion improves again ($\xi=0.83$, configuration 3), since the loss of unreacted phosphate is avoided. This conversion is however lower than that of an MSMPR ($\xi=0.93$). In the PFR, the highest conversion is achieved ($\xi=1.0$) as a result of the high supersaturation at the reactor inlet, which accelerates the conversion process at the earliest stages of the particles residence time. Actually, the conversion proceeds so fast that it is essentially completed in the first 10% of the PFR volume ($V_{R,90}=0.1$ in Table IV).

6.4.4.2 Average product size

The number-averaged diameter of the product (d_{prod}) is calculated from eq.(9). The moments of the product size distribution $m_{p,prod}$ are calculated by averaging the product of the p^{th} local moment and velocity in the z-direction ($m_p \cdot v_z$) over the two-dimensional reactor outlet S,

$$m_{p,prod} = \frac{\int_S m_p v_z dS}{\int_S v_z dS} \quad p=0,1,2,\dots \quad (22)$$

Varying the location of the feed streams caused the average product size to change by a factor 1.9. In configurations 1 and 3, where the sodium hydroxide is 'pre-diluted', the average product sizes are larger than in configuration 2, where no pre-dilution occurs. In configuration 2 the higher local supersaturations result in higher nucleation rates and consequently in smaller average sizes. The largest d_{prod} was found for the MSMPR, due to the absence of zones of high supersaturation, while the smallest size was found for the PFR due to the high supersaturation at the reactor inlet.

6.4.4.3 Coefficient of variation

The number-based coefficient of variation of the product size distribution, $(c.v.)_{prod}$, is calculated from eq.(9). The moments of the product size distribution $m_{p,prod}$ are calculated from the local moments at the reactor outlet (eq.(22)).

Varying the location of the feed streams caused the coefficient of variation of the distribution to change by a factor 1.5. The $(c.v.)_{prod}$ is the largest in configuration 1, probably as a result of the recirculation stream, which causes a wide residence time distribution of the solids. For configuration 2, where the recirculation stream is just a dead zone (hardly any particles are present), a smaller c.v. results. Similarly, in configuration 3 the lower recirculation stream occupies only a small reactor volume and a smaller c.v. results. The spread in the product size distribution in the ideal reactors was smaller than in the three other reactor configurations.

6.5 Conclusions

A mathematical model for a precipitation system with only nucleation and growth processes has been developed, which predicts for a given reactor configuration, among others, the local

supersaturation, local moments of the particle size distribution and product properties. This system has been illustrated for calcium phosphate, although it is known that in this case also aggregation has to be taken into account.

Although the model was only used to describe the precipitation of calcium phosphate, it can easily be adapted to simulate the precipitation of other salts from solution.

The model is a useful tool in improving the understanding of the role of individual processes such as nucleation, growth, and convection for the global reactor performance.

The formation of undesired modifications or morphologies due to too high local supersaturation levels can be predicted.

Simulations with a continuous double jet reactor at various positions of reactant inlets showed a considerable change in the conversion (0.57 to 0.83), the average product size (factor 1.9) and the number-based coefficient of variation of the product size distribution (factor 1.5). Nucleation and growth occur only in a small part of the total reactor volume.

List of symbols

[]	concentration, $\text{kmol} \cdot \text{m}^{-3}$ liq
()	activity, $\text{kmol} \cdot \text{m}^{-3}$ liq.
J	nucleation rate, $\# \cdot \text{m}^{-3} \text{ susp} \cdot \text{s}^{-1}$
c.v.	number-based coefficient of variation of the size distribution, -
d_{avg}	number-based average particle size, m
D	diffusivity, $\text{m}^2 \cdot \text{s}^{-1}$
g	gravity acceleration, $\text{m} \cdot \text{s}^{-2}$
G	linear growth rate, $\text{m} \cdot \text{s}^{-1}$
k_a, k_v	shape factors for area and volume, -
K_s	solubility product of calcium phosphate based on activities, $\text{kmol}^5 \cdot \text{m}^{-15}$
L	particle dimension, m
m_p	p^{th} moment of the distribution, $\text{m}^p \cdot \text{m}^{-3} \text{ susp}$
mw	molecular weight, $\text{kg} \cdot \text{kmol}^{-1}$
N, L, A	total number, length and area of the PSD, $\# \cdot \text{m}^{-3} \text{ susp.}$, $\text{m} \cdot \text{m}^{-3} \text{ susp.}$, $\text{m}^2 \cdot \text{m}^{-3} \text{ susp.}$
P	pressure, $\text{N} \cdot \text{m}^{-2}$
R	rate of appearance by chemical reaction, $\text{kg} \cdot \text{m}^{-3} \text{ susp} \cdot \text{s}^{-1}$
S	'cross section' of the 2D-reactor outlet, m
Sc	turbulent Schmidt number, -
u_i	velocity in the direction i, $\text{m} \cdot \text{s}^{-1}$
v_z	fluid velocity normal to S, $\text{m} \cdot \text{s}^{-1}$

w_{in}	inlet mass flow rate of phosphate solution, $\text{kg} \cdot \text{s}^{-1}$
x_i	vector coordinates $x_i \equiv \{x_1, x_2, x_3\}$
X	mass fraction, $\text{kg} \cdot \text{kg}^{-1} \text{ susp.}$

Greek letters

β	supersaturation, -
μ	viscosity, $\text{kg} \cdot \text{m}^{-1} \cdot \text{s}^{-1}$
ρ	density, $\text{kg} \cdot \text{m}^{-3}$
ξ	conversion, -

Subscripts

cryst	solid phase
liq	liquid phase
max	maximum value
out	reactor outlet
k	chemical species in solution, $k = \text{Ca}, \text{PO}_4, \text{Na}, \text{Cl}$
p	moment of the particle size distribution, $p = 0, 1, 2, \dots$
prod	product, i.e. particles at the reactor outlet
t	turbulent
i, j	directions in cartesian coordinates, $i, j = 1, 2, 3$

Superscripts

—	time averaged component of variable
'	fluctuating component of variable

References

1. Bird, R.B., Stewart, W.E. & Lightfoot, E.N., *Transport phenomena*, John Wiley, London, 1960.
2. Davies, C.W., *Ion Association*, Butterworths, London, 1962.
3. Hinze, J.O., *Turbulence, an introduction to its mechanisms and theory*, Mc. Graw Hill, N.Y., 1959.
4. Hulburt, H.M. and Katz, S., Some problems in particle technology. A statistical mechanical formulation, *Chem. Eng. Sci.* **19**, p.555-574, 1964.
5. Kemenade van, M.J.J.M. and de Bruyn, P.L., A kinetic study of precipitation from supersaturated calcium phosphate solutions, *J. Colloid Interface Sci.*, **118**(2), p.564-585, 1987.
6. Launder, B.E. and Spalding, D.B., *Mathematical models in turbulence*, Academic Press, London, 1972.
7. Nancollas, G.H. et al., Mineral phases of calcium phosphate, *Anat. Rec.* **224** (2), p.234-41, 1989.
8. Randolph, A.D. and Larson, M.A., *Theory of particulate processes. Analysis and techniques of continuous crystallization*, Academic Press, 2nd ed., 1988.
9. Rodi, W., *Turbulence models and their application in hydraulics: a state of the art review*, presented by the Int. Assoc. for Hydraulic Research - I.A.H.R. - Section of Fundamentals of Division II: Experimental and Mathematical Fluid Dynamics, 1984, Delft.
10. Seckler, M.M. et al., Phosphate removal from waste water by means of a full scale pellet reactor, *11th Symp. Industrial Crystallization*, Sept. 18-20, 1990, Garmisch-Partenkirchen, Fed. Rep. Germany.
11. Tennekes, H. and Lumley, J.L., *A first course in turbulence*, The MIT Press, London, 1972

CHAPTER 7

OPTIMIZATION OF THE PHOSPHATE REMOVAL EFFICIENCY DURING CALCIUM PHOSPHATE PRECIPITATION IN A FLUIDIZED BED

Abstract

The aggregation of fine primarily formed particles with sand grains in a fluidized bed for phosphate removal was experimentally studied by means of an experimental set-up which isolated aggregation from other processes during calcium phosphate precipitation, as well as through experiments under normal operation of the fluidized bed. The net aggregation process was described by means of a mathematical model which takes into account two competing mechanisms: orthokinetic aggregation and breakage. The net aggregation process was found to account for 60% of the phosphate removed by the fluidized bed. The orthokinetic aggregation can be improved by spreading the supersaturation more evenly throughout the reactor, and breakage can be diminished by a low energy dissipation rate in the bed. Optimization of the phosphate removal efficiency was achieved for sand grains of small sizes (0.1-0.3 mm), for a low superficial velocity ($7 \cdot 10^{-3}$ m/s) and by spreading the addition of the NaOH solution (reactant) over two dosage points. By selecting these conditions, the phosphate removal efficiency was $\sim 80\%$.

7.1 Introduction

Phosphate can be removed from wastewater by a process based on the precipitation of amorphous calcium phosphate upon sand grains in a fluidized bed. The main technological bottle-neck of the process is the low efficiency with respect to the phosphate removal. In Chapter 2 a black box parametric study of the process led to a phosphate removal efficiency of only 50%. It became clear that a further optimization of the phosphate removal efficiency would require a better knowledge of the fundamentals of the process.

The basic underlying processes occurring in the fluidized bed were therefore studied in Chapters 3 to 6. It was found that submicron particles ($\sim 0.05 \mu\text{m}$) of amorphous calcium phosphate are formed by primary nucleation and molecular growth at the bottom of the

reactor within a very short time (≤ 0.5 s) and subsequently form aggregates. As these aggregates, here called 'fines', become large enough ($\sim 10 \mu\text{m}$), they become prone to breakage and a more or less constant particle size distribution is reached within ~ 10 s. Part of the fines undergo *aggregation* with the sand grains, thus contributing to the phosphate removal by the bed. Separation of phosphate also proceeds by molecular transport of calcium and phosphate ions in solution towards the sand grains, i.e., by *molecular growth*. The phosphate which is not removed leaves the bed at the top, either as fines or as ions in solution. The picture of the process just presented indicates that an improvement in the phosphate removal efficiency may be achieved if process conditions are found which favor aggregation, molecular growth, or preferably both. In Chapter 3 it was already shown that the aggregation of the fines with the grains is most likely an important feature in the phosphate removal. Therefore in this chapter an optimization of the phosphate removal efficiency was attempted by focusing on the aggregation process.

Firstly, the aggregation of the fines with the grains in a fluidized bed was experimentally studied and mathematically modelled. In order to experimentally isolate the aggregation from other processes (nucleation and molecular growth), an experimental set-up was designed in which the reactants were pre-mixed in a small stirred reactor upstream the fluidized bed. The conversion of phosphate from the liquid to the solid phase at the stirred reactor outlet was almost complete and the suspension entering the fluidized bed was only slightly supersaturated, so mainly aggregation proceeded in the fluidized bed.

Secondly, with a better understanding of the process of aggregation, optimization of the phosphate removal efficiency under normal operation of a fluidized bed (i.e. without pre-mixing of reactants) was attempted. The energy dissipation rate and the supersaturation were selected to be varied experimentally. The values of these parameters which optimized the phosphate removal efficiency were determined.

7.2 Model description

A mathematical model was developed to describe the orthokinetic aggregation of the fines

with the grains in the fluidized bed. Saffman and Turner [4] proposed the following equations for the collision frequency (J_{ij}) between particles of sizes d_i and d_j for different size ranges r ($r=d/2$):

$$J_{ij} = 1.29 \left(\frac{E}{\nu} \right)^{0.5} (d_i + d_j)^3 N_i N_j \quad r < 6\lambda_k \quad (1)$$

$$J_{ij} = 2.36 \frac{E^{5/12}}{\nu^{1/4}} (d_i + d_j)^{8/3} N_i N_j \quad 6\lambda_k \leq r \leq 25\lambda_k \quad (2)$$

$$J_{ij} = 6.87 E^{0.33} (d_i + d_j)^{7/3} N_i N_j \quad 25\lambda_k \leq r \leq \lambda_{macro}/2 \quad (3)$$

$$J_{ij} = 7.09 (E\lambda_{macro})^{0.33} (d_i + d_j)^2 N_i N_j \quad \lambda_{macro}/2 \leq r \approx \lambda_{macro} \quad (4)$$

where E is the energy dissipation rate, ν the kinematic viscosity, and N the particle concentration. The subscripts i and j refer respectively to the fines and grains. λ_{macro} is a macro length scale that can be taken as the reactor radius. The Kolmogorov length scale λ_k is defined as

$$\lambda_k = (\nu^3 / E)^{0.25} \quad (5)$$

For the range of conditions in this work, $\lambda_k \approx 70 \mu\text{m}$ and $r < 400 \mu\text{m}$, so equation (1) was used. The decrease in the fines concentration by aggregation with the grains in a fluidized bed is derived from the particle number balance for the fines:

$$\frac{dN_i}{dt} = -B J_{ij} \beta \quad (6)$$

with the initial condition $N_i = N_{i,in}$ at $t=0$. In eq.(6) t is the reaction time, β the supersaturation and B the collision efficiency, which is defined as the part of the collisions actually resulting in aggregation between two particles. The reaction time follows from

$$t = \frac{\epsilon X}{V_{sup}} \quad (7)$$

where x is the axial position in the bed ($x=0$ for $t=0$ and $x=L$ for $t=t_{out}$), v_{sup} the superficial velocity and ϵ the bed porosity. The linear dependence of the aggregation process on the supersaturation used in eq. (6) was earlier proposed for the precipitation of calcium carbonate [3] and for the crystallization of adipic acid [1]. The supersaturation is thereby defined as

$$\beta = \frac{1}{5} \ln \frac{(Ca^{2+})^3(PO_4^{3-})^2}{K_s} \quad (8)$$

where the brackets indicate activities and K_s is the solubility product of amorphous calcium phosphate, with a value of $3 \cdot 10^{-27} \text{ M}^5$ (Chapter 2). The supersaturation as a function of time, $\beta(t)$, is a model input which can be experimentally determined.

The collision efficiency B in eq. (6) includes the process of breakage of fines from the grains. In Chapter 4 it was found that the breakage is influenced by the energy dissipation rate. Other authors [2,5] also came to the same conclusion. A simple function is proposed here to describe this influence:

$$B = B_0 (E/E_0)^\alpha \quad (9)$$

where E_0 is an arbitrary reference value for the energy dissipation rate. B_0 and α are characteristics of the precipitating system. B_0 and α are the only model parameters which have to be adjusted in order to obtain an agreement between the model outputs and the experimental data. All other parameters can be directly measured or calculated from measured quantities.

Equations (6) and (9) thus describe not only the aggregation between fines and grains in a fluidized bed, but also the breakage. Because aggregation and breakage can not be seen separately, hereafter the term aggregation refers to the net process. The phosphate removal efficiency (by aggregation only) can be calculated by integrating eq. (6) from $t=0$ to $t=t_{out}$ and by assuming that the particle size of the fines is constant in time:

$$\eta_{ag} = \frac{N_{i,in} - N_{i,out}}{N_{i,in}} \quad (10)$$

Only the energy dissipation rate E and the concentration of grains N_j are now needed to calculate the decrease in the concentration of fines by aggregation and therefore the phosphate removal efficiency by aggregation. The energy dissipation rate in a fluidized bed can be calculated from

$$E = \frac{\Delta p v_{sup}}{\rho_l L \epsilon} \quad (11)$$

where Δp is the pressure drop, which is derived from a force balance over the bed

$$\Delta p = (1 - \epsilon)(\rho_s - \rho_l)gL \quad (12)$$

The bed porosity ϵ is calculated with a modified Kozeny-Carman equation [6]

$$\frac{\epsilon^3}{(1 - \epsilon)^{0.8}} = 130 \left(\frac{v_{sup}^{1.2} v^{0.8}}{g d_j^{1.8}} \right) \left(\frac{\rho_l}{\rho_s - \rho_l} \right) \quad (13)$$

where d_j is the size of the grains. The bed height (L) is calculated from

$$L = \frac{M}{\frac{\pi D^2}{4} (1 - \epsilon) \rho_s} \quad (14)$$

When the grains particle size and the bed porosity are known, the concentration of the grains can be calculated from

$$N_j = \frac{1 - \epsilon}{\frac{\pi d_j^3}{6}} \quad (15)$$

For d_i and d_j the volumetric mean particle size can be taken. The complete model for aggregation in a fluidized bed consists of the eqs. (1) till (15). In Table I the in- and outputs of the model are summarized and the assumptions and parameters are listed.

The influence of the energy dissipation rate and of the supersaturation on the aggregation process were selected to be experimentally investigated. The former can be studied by varying the superficial velocity (and thus the total flow) and the diameter of the grains (eq.

Table I. Main characteristics of the mathematical model for aggregation in a fluidized bed.

ASSUMPTIONS

- orthokinetic aggregation.
- size independent, energy dissipation dependent breakage.
- fines and liquid velocity are the same.
- aggregation fines-fines is neglected (fines diameter constant).
- fines and grains diameters smaller than 6 times the Kolmogorov length scale.
- no axial dispersion of fines or liquid.
- grains in the bed are well mixed.

ADJUSTABLE PARAMETERS

- B_0 : collision efficiency at reference conditions.
- α : exponential dependency of the collision efficiency on the energy dissipation.

INPUT

- inlet flows and concentrations of dissolved components.
- grains diameter and total mass.
- fines diameter.
- supersaturation profile in the reactor.

OUTPUT

- phosphate removal efficiency as a function of the bed height.
-

(11),(12) and (13)). The latter can be studied by spreading the dosage of reactants over two addition points.

7.3 Experimental

Experiments with a fluidized bed preceded by a pre-mixing reactor were carried out in order to study the aggregation independent of other processes in the bed. Additionally, experiments were performed with a fluidized bed without pre-mixing. Both types of experiments are described in the following sections.

7.3.1 Fluidized bed preceded by a pre-mixing reactor

A pre-mixing reactor was placed upstream the fluidized bed, as shown in Figure 1. The pre-mixing reactor was a cylindrical perspex vessel with a volume of 0.03 l and provided with a propeller-type impeller at a rotation speed of 13 s⁻¹. The fluidized bed was a cylindrical perspex vessel with a diameter of 0.05 m and a total height of 2.1 m. The details of the inlet

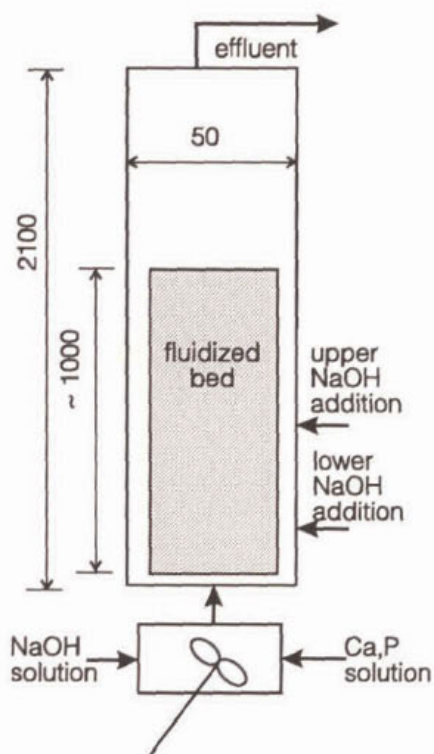


Figure 1. Experimental set-up. Measures in mm. Out of scale.

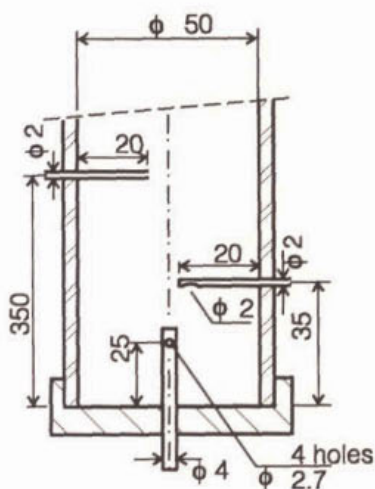


Figure 2. Detail of the bottom part of the fluidized bed. Measures in mm. Out of scale.

nozzles of the fluidized bed are shown in Figure 2. The central nozzle produced 4 radial streams at angles of 90° and velocities of 1 m/s. The fluidized bed was filled with 1 kg quartz sand. The reactants

were all chemical grade and the water was demineralized (conductivity $< 1 \mu\text{S}\cdot\text{cm}^{-1}$). Each experiment was started by filling the fluidized bed with bare sand, and by adding an undersaturated calcium phosphate solution through the central nozzle as well as a base stream (a NaOH solution) through the lower lateral nozzle of the fluidized bed, in order to deposit a phosphate layer upon the grains under 'normal' operating conditions (without pre-mixing) during a period of 24 h. This period of time was sufficient to develop a phosphate layer of at least $10 \mu\text{m}$. After this period the base addition to the fluidized bed was stopped and substituted by a base addition to the pre-mixing reactor. The fluidized bed was fed with the outlet stream of the pre-mixing reactor through the central nozzle.

Samples of the total and 'filtered' flows were taken for chemical analysis at the outlet stream of the pre-mixing reactor as well as at several heights in the fluidized bed, with the

procedure described in Chapter 3. The filtered samples were taken by suctioning with a syringe provided with a filter (0.45 μm). This procedure resulted in filtering times of 0.5 s or less.

The concentration of the elements Ca, P and Na in the unfiltered and filtered samples were determined by inductively coupled plasma - atomic emission spectroscopy (Spectro). All the samples were pre-treated with 2 N HCl in order to dissolve any suspended solids.

The total flow was varied within the range of 40-120 l/h and sand grains were used with size ranges of both 0.1-0.3 mm (fine sand) and 0.4-0.6 mm (coarse sand). The flow rates and concentrations used in all the experiments are shown in Table II.

Table II. Flow rates, concentrations and pH values used in all the experiments. n.m. = not measured. ⁽¹⁾ top outlet of the fluidized bed.

Stream nr.	flow $\text{m}^3 \cdot \text{s}^{-1}$ $\times 10^6$	P conc. $\text{kmol} \cdot \text{m}^{-3}$ $\times 10^3$	Na conc. $\text{kmol} \cdot \text{m}^{-3}$ $\times 10^3$	Ca conc. $\text{kmol} \cdot \text{m}^{-3}$ $\times 10^3$	pH -
Ca,P soln.	13.5-35.1	1.7	1.7	4.9	5
NaOH soln.	0.38-1.0	0	100	0	n.m.
<i>Total</i>	<i>13.9-36.1</i>	<i>1.6</i>	<i>4.4</i>	<i>4.8</i>	<i>8-9⁽¹⁾</i>

7.3.2 Fluidized bed with a spread in base dosage

The experimental set-up was the same as the one presented previously (Figure 1), except for the pre-mixing reactor, which was not used. The fluidized bed was provided with two nozzles for NaOH dosage placed at heights of 0.035 m and 0.35 m (Figure 2). The experimental procedure as well as the process conditions were the same as above.

In order to study the influence of the supersaturation on the phosphate removal, the base addition was spread between the two base addition nozzles. The total base dosage remained constant, only the distribution between the two locations was varied as follows: the base flow

rate ratio (ϕ_{low}/ϕ_{tot}), defined as the flow in the lower nozzle divided by the total base flow, assumed the values 1, 0.76, 0.6, 0.43, 0.31 and 0.20. For the two lowest flow rate ratios ($\phi_{low}/\phi_{tot}=0.31$ and 0.20), the base flow at the bottom was too small to create a supersaturated solution after the first base dosage. For simplicity these conditions are referred to as 'total flow added through the upper nozzle'. Therefore the limiting situations of total flow added through either the lower or the upper nozzle were explored.

7.4 Results and discussion

7.4.1 Definition of terms and preliminary calculations

The *supersaturation* along the fluidized bed was obtained from measurements of the liquid phase calcium and phosphate concentrations at several reaction times (axial positions). From these concentrations and from the equilibrium model presented in Chapter 2, the activities of the ions Ca^{2+} and PO_4^{3-} were calculated and used in eq.(8) to obtain the supersaturation $\beta(t)$. For the experiments without pre-mixing, the supersaturation at the inlet of the fluidized bed was estimated from the composition of the inlet streams by assuming that the reactants mix completely before significant precipitation takes place.

The *supersaturation values* at the fluidized bed inlet and outlet, averaged over all experiments with pre-mixing, were $\beta_{in}=0.7$ and $\beta_{out}=0.1$. For the experiments without pre-mixing, $\beta_{in}=2.6$ and $\beta_{out}=0.1$ were found. For the experiment without premixing at 80 l/h and with coarse sand, the supersaturation was found to decrease with time in an exponential way:

$$\beta(t) = (\beta_{in} - \beta_{out})e^{-\frac{t}{t_0}} + \beta_{out} \quad (16)$$

where $t_0=10$ s is a decay time for the supersaturation that was adjusted to the experimental data. Eq.(16) with $t_0=10$ s was assumed to be valid for the experiments with and without pre-mixing, for flow rates in the range 50 - 130 l/h and for both fine and coarse sand. The decay time for the supersaturation represents about 10% of the residence time of the liquid phase in the fluidized bed (~ 100 s).

The *phosphate removal efficiency and the conversion along the bed height* were calculated from measurements of the phosphate mass flows entering the fluidized bed and at several bed heights. The efficiency and conversion were defined as,

$$\eta = (w_{P,in} - w_{P,tot}) / w_{P,in} \quad (17)$$

$$X = (w_{P,in} - w_{P,sol}) / w_{P,in} \quad (18)$$

where $w_{P,in}$ represents the flow of phosphate at the fluidized bed inlet ($\text{kg} \cdot \text{s}^{-1}$), $w_{P,tot}$ gives the flow of phosphate in both dissolved form and as fines at a given axial position in the bed and $w_{P,sol}$ is the flow of dissolved phosphorus at the same axial position. The efficiency calculated from eq. (10) coincides with the definition above for situations where aggregation is the only mechanism responsible for the phosphate removal, such as with a fluidized bed preceded by a pre-mixing reactor.

The *reference conditions* for the calculation of the energy dissipation rate E_0 in equation (9) were arbitrarily chosen to be the fluidization of coarse sand with a total flow of 70 l/h. By applying eqs. (11), (12) and (13) for these conditions, the value $E_0 = 0.049 \text{ W} \cdot \text{kg}^{-1}$ was derived.

The mathematical model presented here takes into account the energy dissipation due to fluidization, but it neglects the *dissipation of the kinetic energy* of the main inlet stream ($E_{kinetic}$). This contribution can be estimated from a kinetic energy balance around the bed volume where the dissipation takes place:

$$E_{kinetic} = \frac{1}{2} \frac{v_{sup}}{\epsilon L} v_{nozzle}^2 \quad (19)$$

where v_{nozzle} is the fluid velocity in the central nozzle and L is the height of the fluidized bed where the kinetic energy is dissipated. For the fluidization of coarse sand at 80 l/h, $v_{nozzle} = 1 \text{ m} \cdot \text{s}^{-1}$ and $\epsilon = 0.6$. Assuming that $L = 0.1 \text{ m}$ (the corresponding residence time is 9 s), the dissipation of kinetic energy at the bottom of the bed is derived, $E_{kinetic} = 0.09 \text{ W} \cdot \text{kg}^{-1}$. This value is of the same order of magnitude as the dissipation due to fluidization.

7.4.2 Fluidized bed preceded by a pre-mixing reactor

The conversion at the outlet of the pre-mixing reactor was $94 \pm 4 \%$ for all experiments, the oscillations being due to small variations in the flow rates of reactants. This conversion was about 2% lower than the conversion at the outlet of the fluidized bed reactor (this value was averaged over a large number of experimental data). Both conversions were slightly lower than the equilibrium conversion so that a small supersaturation was left in the fluidized bed. The experimentally determined supersaturation profile along the fluidized bed, for all experiments with pre-mixing, was described by eq.(16) with $\beta_{in}=0.7$, $\beta_{out}=0.1$ and $t_0=10$ s (section 7.4.1). Owing to the low supersaturation, hardly any nucleation and growth occurred in the fluidized bed, so only aggregation continued (Chapter 4). Therefore, the phosphate removal in the fluidized bed in these experiments was assumed only to proceed by aggregation.

Figure 3 gives the phosphate removal efficiency as a function of the total flow for the two sizes of grains. The symbols represent the experimental data and the model outputs are shown as lines. The lowest flow rates for fine grains (50 l/h) and coarse grains (80 l/h) were the lowest possible values which still kept fluidization. The aggregation model was applied for these experiments with the

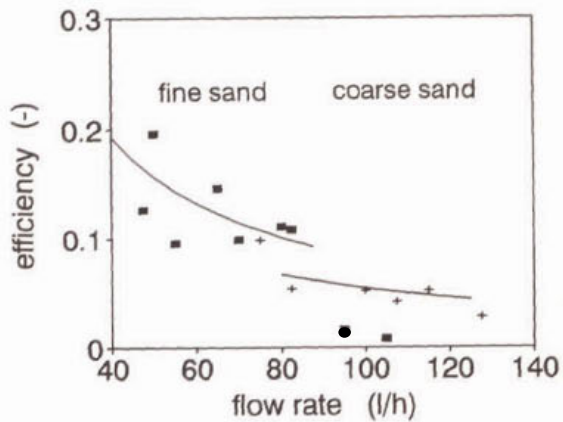


Figure 3. P removal efficiency in a fluidized bed with pre-mixing of reactants, fine (■) and coarse sand (+). Lines are model outputs with $B_0=4.1 \times 10^{-5}$, $\alpha=-1.3$.

following fit values for the parameters given in the collision efficiency equation (eq. (9)): $B_0=4.1 \cdot 10^{-5}$, $\alpha=-1.3$. Figure 3 shows that the model gives a good prediction of the measured efficiency for both types of grains and over the complete range of the total flow. It also shows that both a small diameter of the grains and a low throughput favor a high efficiency.

Simulations were also performed in which the collision efficiency was assumed to be independent of the energy dissipation rate ($\alpha=0$, not shown). The calculated phosphate removal efficiency became practically independent of the flow rate, contrary to the measured trend shown in Figure 3. This demonstrates that an increase in the energy dissipation rate indeed promotes breakage. The energy dissipation rate also stimulates the aggregation between fines and grains through the collision frequency, as shown in eq. (1). Substitution of eq. (1) and eq. (9) into eq. (6) shows that the net process aggregation minus breakage, given by dN/dt , is proportional to the energy dissipation rate to the power -0.8. Therefore, the net effect of an increase in the energy dissipation rate is a decrease in the phosphate removal efficiency.

7.4.3 Fluidized bed with base dosage at the bottom

Here experiments are described in which no pre-mixing reactor is used upstream the fluidized bed. The reactants were mixed at the bottom of the bed (Figure 2 with NaOH dosage via the lowest nozzle), producing a high local supersaturation. Therefore, all the elementary steps of the precipitation process (nucleation, molecular growth and aggregation) proceeded simultaneously within the fluidized bed. Phosphate removal may proceed by aggregation, molecular growth, or both.

The experimentally determined supersaturation profile along the fluidized bed, for all experiments with pre-mixing, was described by eq.(16) with $\beta_{in}=2.6$, $\beta_{out}=0.1$ and $t_0=10$ s (section 7.4.1).

The experimentally determined phosphate removal efficiency as a function of the bed height is shown in Figure 4 for an experiment with coarse sand and a flow rate of 80 l/h. The aggregation model was applied for this experiment with the same parameters used for the configuration with pre-mixing ($B_0=4.1 \cdot 10^{-5}$, $\alpha=-1.3$). The only difference in the model description was the supersaturation profile over the bed. The dotted lines in Figure 4 show that the predicted efficiencies are too low, indicating that processes other than aggregation, e.g. molecular growth, also play a role in the phosphate removal. As a first approximation the growth process may be incorporated in the model by adapting the fit parameters B_0 and

α . A good agreement between calculated and measured phosphate removal efficiencies was found by using the adjusted parameters $B_0=9.2\cdot 10^{-5}$ and $\alpha=-1.3$, as shown by the continuous line in Figure 4.

Figure 4 also shows that most of the phosphate removal occurred at the bottom of the bed (in agreement with the data in Chapter 3), due to the fact that the supersaturation decreased with the bed height and due to its effect on the aggregation. This sustains the important role of the supersaturation in the phosphate removal.

The phosphate removal efficiency as a function of the total flow for two sizes of grains is shown as data points in Figure 5. The lowest flow rates for fine grains (50 l/h) and coarse grains (80 l/h) were the lowest possible values for fluidization. Just as for the

configuration with pre-mixing, a small grain diameter and a low throughput favored a high phosphate removal efficiency. The model parameters for aggregation only ($B_0=4.1\cdot 10^{-5}$ and

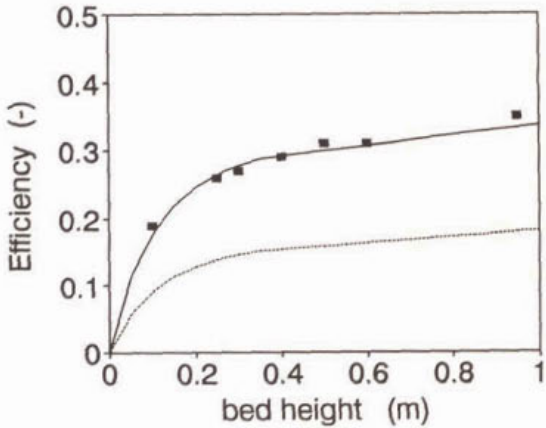


Figure 4. P removal efficiency in a fluidized bed without pre-mixing of reactants, coarse sand, 80 l/h. Model outputs with aggregation (dotted line, $B_0=4.1\cdot 10^{-5}$) and aggregation+growth (cont. line, $B_0=9.2\cdot 10^{-5}$). $\alpha=-1.3$.

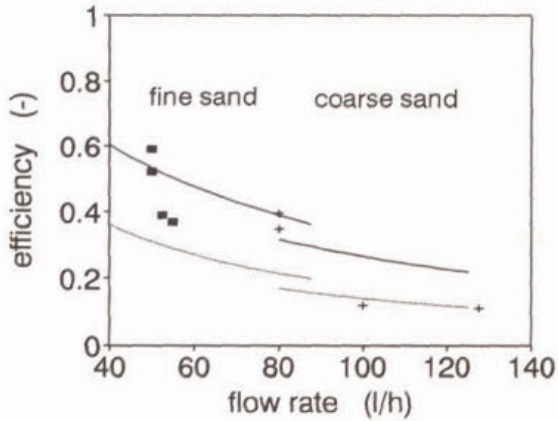


Figure 5. P removal efficiency in a fluidized bed without pre-mixing of reactants, fine (■) and coarse sand (+). Model outputs for aggregation (dotted lines, $B_0=4.1\cdot 10^{-5}$) and aggregation+growth (cont. lines, $B_0=9.2\cdot 10^{-5}$). $\alpha=-1.3$.

$\alpha=-1.3$) as well as for aggregation and molecular growth ($B_0=9.2 \cdot 10^{-5}$ and $\alpha=-1.3$) were applied to these experiments and are shown respectively as dotted lines and continuous lines in Figure 5. A reasonable agreement between the model and the experiments was found when aggregation and growth were taken into account. The phosphate removal efficiencies due to aggregation equaled about 60% of the experimentally found efficiencies. This fraction apparently represents the contribution of aggregation to the process of phosphate removal in a fluidized bed.

7.4.4 Fluidized bed with a spread in base dosage

In the previous sections it was shown that the experimentally determined supersaturation decreased exponentially with time, with a short decay time of 10 s. By spreading the base dosage between two or more addition points, a non-negligible supersaturation is sustained in the reactor for a longer period of time (i.e. in a larger part of the reactor), thus improving the phosphate removal efficiency by increasing both the net aggregation and the molecular growth of the grains. Having this picture of the process in mind, optimization of the phosphate removal was attempted by performing experiments where the base was added through two addition points and the base flow rate ratio (ϕ_{low}/ϕ_{tot}) was varied, while the total base flow (ϕ_{tot}) was kept constant. Two series of such experiments are presented here, with the following operating conditions: a total flow of 50 l/h with fine sand and of 80 l/h with coarse sand.

The experimentally determined phosphate removal efficiency as a function of the flow rate ratio (ϕ_{low}/ϕ_{tot}) for the two series of experiments is shown as data points in Figure 6a and 6b.

In the series of experiments with coarse sand and a total flow of 80 l/h (Figure 6a), the efficiency versus ϕ_{low}/ϕ_{tot} curve passed through a maximum, showing that it is advantageous to spread the base addition. The efficiency increased from 0.4 at $\phi_{low}/\phi_{tot}=1$ to 0.6 at $\phi_{low}/\phi_{tot}=0.5$. In the experiments with fine sand and a total flow of 50 l/h (Figure 6b), the efficiency increased from 0.5 at $\phi_{low}/\phi_{tot}=1$ to 0.8 at $\phi_{low}/\phi_{tot}=0.5$. The highest efficiency (0.8) was found at a low total flow and a small grain diameter. This trend had already been observed in the experiments with single base addition.

Figure 6a (coarse sand) shows that, if only one addition point is used, the upper nozzle should be chosen, since the phosphate removal efficiency for $\phi_{low}/\phi_{tot}=0.2$ was higher ($\eta=0.54$) than for $\phi_{low}/\phi_{tot}=1$ ($\eta=0.40$). This effect can be explained by the fact that at the bottom of the reactor the energy dissipation rate was higher due to the high fluid velocity in the central nozzle ($1\text{ m}\cdot\text{s}^{-1}$). This high energy dissipation rate at the bottom of the fluidized bed promoted the breakage process (eq. (9)) and thus led to a lower phosphate removal efficiency. Therefore, these experimental results suggest that the fluid velocity at the inlet nozzles should be lower than $1\text{ m}\cdot\text{s}^{-1}$.

The mathematical model for aggregation was applied to these experiments in the following way: (i) the supersaturation at each NaOH addition point has

the value obtained by complete mixing of reactants and before precipitation proceeds; (ii) the supersaturation after each NaOH addition point decreases exponentially with time with a decay time $t_0=10\text{ s}$; (iii) the adapted collision efficiency parameters (also used in section 7.4.3) $B_0=9.2\cdot 10^{-5}$ and $\alpha=-1.3$ hold. The model predictions are shown as lines in Figures

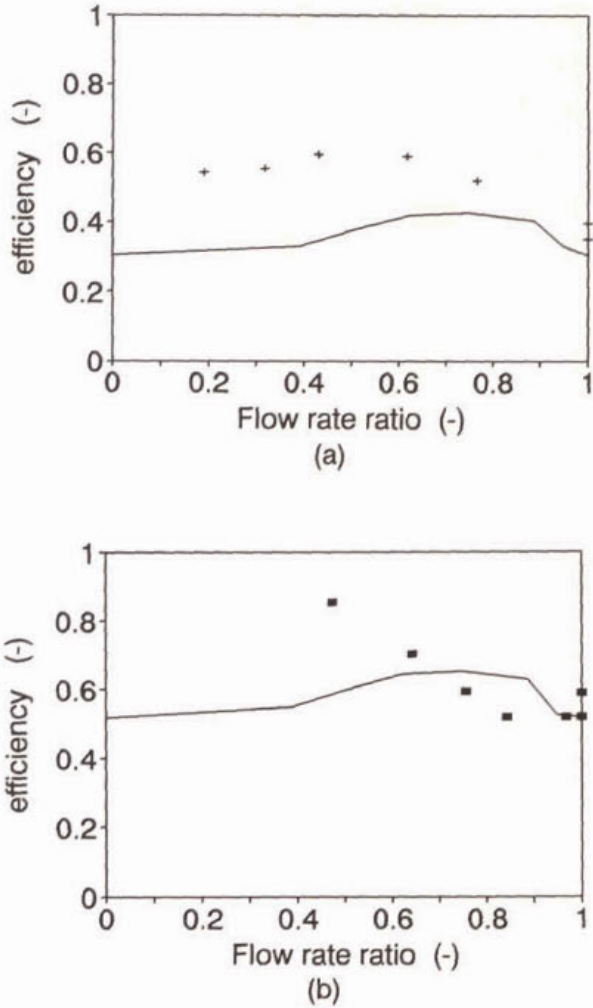


Figure 6. P removal efficiency versus the flow rate ratio ϕ_{low}/ϕ_{tot} for (a) coarse sand at 80 l/h and (b) fine sand at 50 l/h. Lines are model outputs for $B_0=9.2\cdot 10^{-5}$, $\alpha=-1.3$.

6a and 6b. The model agrees with the experiments in the sense that also by the model a maximum in phosphate removal efficiency is found by spreading the base dosage between two addition points. However, the predicted phosphate removal efficiency values are too low and the optimum configuration is predicted for a ϕ_{low}/ϕ_{tot} of 0.75 whereas the experimental optimum value was approximately 0.5. It is likely that these deviations are due to the contribution of the inlet stream kinetic energy to the total energy dissipation rate, which was not taken into account in the calculations. These deviations strengthen the idea that a high energy dissipation rate is detrimental to the phosphate removal.

The optimum phosphate removal efficiency was found for a base flow rate ratio ϕ_{low}/ϕ_{tot} of 0.5. The variable ϕ_{low}/ϕ_{tot} suffers from the limitation that a fraction of ϕ_{low} is consumed to saturate the feed. This fraction varies with the influent characteristics such as pH and buffer capacity. It seems thus more convenient to express the spread in base addition in terms of the *equilibrium conversion* after the lower addition point. In our experiments, $\phi_{low}/\phi_{tot}=0.5$ corresponded to $X_{low}=0.25$. This equilibrium conversion after the lower dosage point should therefore be used to optimize the phosphate removal.

The sustainment of a non-negligible supersaturation for a longer period of time can also be achieved by using a $\text{Ca}(\text{OH})_2$ suspension (instead of a NaOH solution). The OH^- ions become available slowly as the $\text{Ca}(\text{OH})_2$ particles dissolve slowly along the bed length. In Chapter 2, experiments with a $\text{Ca}(\text{OH})_2$ suspension were performed and indeed led to slightly higher phosphate removal efficiencies (0.5) than with NaOH (0.4).

7.5 Conclusions

The most important mechanism for the phosphate removal in a fluidized bed is the aggregation of primarily formed particles with the grains constituting the bed. It accounts for 60% of the total phosphate removed. The remaining 40% is removed by molecular growth.

The aggregation rate in a fluidized bed can be described by a mathematical model which takes into account two competing mechanisms: orthokinetic aggregation and breakage. It was

found, both theoretically and experimentally, that the orthokinetic aggregation can be increased by spreading the supersaturation more evenly throughout the reactor. Breakage can be diminished by choosing fluidization conditions where the energy dissipation rate in the bed is minimized.

Optimization of the phosphate removal efficiency can therefore be achieved by choosing process conditions with a low energy dissipation rate and a supersaturation evenly spread throughout the bed height. The highest phosphate removal efficiency (0.8) was found for sand grains of small sizes (0.1-0.3 mm), for a low superficial velocity ($7 \cdot 10^{-3}$ m/s) and by spreading the base addition over two locations, with an (equilibrium) conversion of 0.25 after the first base dosage. The experimental results suggest that the phosphate removal efficiency can be further improved by lowering the mixing intensity at the bottom of the reactor.

The supersaturation in the fluidized bed decays with a time constant of ~ 10 s, a short time compared to the residence time of the liquid phase, of ~ 100 s.

List of symbols

B	collision efficiency, -	ag	aggregation
B ₀	B at reference conditions, -	i	fines
d	particle diameter, m	in	inlet
D	fluidized bed diameter, m	j	grains
E	energy dissipation rate, m ² ·s ⁻³	l	liquid phase
E ₀	E at reference conditions, m ² ·s ⁻³	low	lower base addition point
g	gravity acceleration, m·s ⁻²	out	outlet
J _{ij}	collision frequency, m ³ ·s ⁻¹	s	solid phase
K _s	solubility product of ACP, kmol ⁵ ·m ⁻¹⁵	tot	solid and liquid phase
L	fluidized bed height, m		
M	total mass sand grains, kg		Greek letters
N	particle concentration, m ⁻³	α	exponential dependency
t	reaction time, s		collision efficiency on
t ₀	time constant for supersaturation decay, s		dissipation, -
v _{sup}	superficial velocity, m·s ⁻¹	β	supersaturation, -
w _p	phosphate flow, kg·s ⁻¹	Δp	pressure drop, N·m ⁻²
x	axial position, m	ε	bed porosity, -
X	conversion, -	λ _k	Kolmogorov length scale.
		η	P removal efficiency, -
		ν	kin. viscosity, m ² ·s ⁻¹
		ρ	density, kg·m ⁻³
<i>Subscripts</i>			
0	reference value		

Greek letters

α	exponential dependency of the collision efficiency on the energy dissipation, -
β	supersaturation, -
Δp	pressure drop, $N \cdot m^{-2}$
ϵ	bed porosity, -
λ_k	Kolmogorov length scale, m
η	P removal efficiency, -
ν	kin. viscosity, $m^2 \cdot s^{-1}$
ρ	density, $kg \cdot m^{-3}$

References

- 1 David, R., Marchal, P., Klein, J.P. and Villermaux, J., Crystallization and precipitation engineering - III. A discrete formulation of the agglomeration rate of crystals in a crystallization process, *Chem. Eng. Sci.* **46**(1), p.205-213, 1991.
- 2 Kusters, K.A., *The influence of turbulence on aggregation of small particles in agitated vessels*, Ph.D. Thesis, Eindhoven University of Technology, 1991.

3 Mersmann, A., unpublished results.

4 Saffman P.G. and Turner, J.S., On the collision of drops in turbulent clouds, *J. Fluid Mech.* **1**, p.16-30, 1956.

5 Thomas, D.G., Turbulent disruption of flocs in small particle size suspensions, *A.I.Ch.E. J.* **10**, p.517-523, 1964.

6 van Dijk, J.C. and Wilms, D.A., Water treatment without waste material-fundamentals and state of the art of pellet softening, *J. Water S.R.T.-Aqua*, **49**(5), p.263-280, 1991.

SUMMARY

Phosphate removal from wastewater is currently applied in order to reduce the phosphorus input to surface waters, thereby minimizing eutrophication. In recent years, attention has been focused on technological routes for phosphate removal which lead to the recovery of phosphate in a concentrated form, suitable to re-use. The precipitation of calcium phosphate upon sand grains in a fluidized bed is such a route and is the main topic of this thesis.

A parametric study of the precipitation of calcium phosphate in a fluidized bed was made. Magnesium and carbonate ions in the water were not detrimental to the phosphate removal at concentrations lower than $3.2 \cdot 10^{-3}$ and $1.8 \cdot 10^{-3} \text{ kmol} \cdot \text{m}^{-3}$, respectively, and a phosphate removal efficiency of 50% was achieved. The optimum pH decreased with an increase of the phosphate content in the water to be treated, and was generally within the range 7.5 and 9. For waters with a low calcium concentration ($< 1 \cdot 10^{-3} \text{ kmol} \cdot \text{m}^{-3}$), it was possible achieve the phosphate removal by means of the crystallization of magnesium phosphate.

In order to improve the efficiency, first the main processes occurring in the reactor were identified and studied independently: the *axial distribution of particles* in the fluidized bed, the *liquid phase mixing*, and the *precipitation of calcium phosphate*.

Phosphate removal in a fluidized bed relies on the deposition of a phosphate layer upon the grains constituting the bed. Therefore, the *axial distribution of particles* in the bed was studied experimentally and theoretically. Complete segregation occurred when the bed consisted of bare sand grains, but as a phosphate shell developed upon the grains, partial mixing of the bed layers proceeded. This behavior was described by a mathematical model based on a velocity-voidage relationship, on a stability mechanism for segregation according to which bed layers with higher bed density segregate to lower axial positions, and on a simplified description of the precipitation process. Simulations were performed in order to optimize the operation of the fluidized bed with respect to the specific surface area of the grains, which affects the phosphate removal, and the phosphate content of the grains, which is related to the commercial value of the product. Both the specific surface area and the phosphate content in the product increased by the use of sand grains with a small diameter.

Chemical reaction precipitation of calcium phosphate occurs through mixing of two or more reactants on a molecular scale. Since precipitation processes are fast, mixing and precipitation occur simultaneously so the kinetics of the *liquid phase mixing* play an important role in determining the characteristics of the product. The influence of hydrodynamic conditions on the precipitation of calcium phosphate was therefore investigated. A 'computational fluid dynamics' method was developed, based on spatially distributed moment equations, on relations for the kinetics of nucleation and growth of the precipitating compound and on the solution of the flow field. The method permits calculation of local quantities such as liquid velocities, local supersaturation and local moments of the particle size distribution. The method was applied on the precipitation of calcium phosphate in a continuous double-jet reactor. By changing the location of feed points, the conversion varied from 57 to 83%, the average particle size changed by a factor 1.9 and the coefficient of variation of the distribution by a factor 1.5. Only a very small fraction of the reactor volume was effectively used for the precipitation.

The *precipitation of calcium phosphate* in a fluidized bed was studied. The kinetics of homogenous nucleation as well as of aggregation were estimated. Substantial primary nucleation, growth and aggregation of an amorphous modification of calcium phosphate proceeded in a short time (~ 10 s) at the bottom of the fluidized bed. These primary particles and aggregates, here called fines, were respectively $\sim 0.05 \mu\text{m}$ and $\sim 100 \mu\text{m}$ in size. Part of these fines aggregated with the sand grains in the fluidized bed, thus contributing with 60% to the total removed phosphate. The remaining 40% was removed by molecular growth.

Optimization of the phosphate removal *efficiency* was achieved by improving the aggregation process. The aggregation was described by means of a mathematical model which took two competing mechanisms into account: orthokinetic aggregation and breakage. The orthokinetic aggregation was improved by spreading the supersaturation more evenly throughout the reactor, and breakage was diminished by low energy dissipation rates in the bed. The optimum phosphate removal efficiency increased from 50% for coarse sand (0.2 to 0.6 mm) and for a superficial velocity of $1.1 \cdot 10^{-2}$ m/s to 80% for fine sand (0.1 to 0.3 mm), for a low superficial velocity ($7 \cdot 10^{-3}$ m/s) and by spreading the base addition over two feed points at two heights in the bed.

SAMENVATTING

Teneinde het fosforgehalte in oppervlaktewater te verminderen om eutrofiëring tegen te gaan, worden technieken ontwikkeld om fosfaat te verwijderen uit afvalwater. De laatste tijd zijn de technologische fosfaatverwijderingsroutes vooral gericht op het afvangen van fosfaat in een geconcentreerde vorm, die geschikt is voor hergebruik.

In deze studie, die gericht is op fosfaatverwijdering door precipitatie van calciumfosfaat in een gefluïdiseerd bed, werden eerst de belangrijke procesparameters vastgesteld. Magnesium en carbonaat ionen in water bleken niet nadelig te werken op de fosfaatverwijdering indien deze ionenconcentraties van respectievelijk $3.2 \cdot 10^{-3}$ en $1.8 \cdot 10^{-3} \text{ kmol} \cdot \text{m}^{-3}$ niet overschreden. In het algemeen werd een fosfaatverwijderingsrendement van 50% bereikt. De optimale pH daalde bij een toenemend fosfaatgehalte in het te behandelen water, en lag in het algemeen tussen de 7.5 en de 9. Voor water met een lage calcium concentratie ($< 1 \cdot 10^{-3} \text{ kmol} \cdot \text{m}^{-3}$) kon fosfaat worden verwijderd door middel van magnesium fosfaat kristallisatie.

Teneinde het rendement van het proces te verbeteren, werden eerst de belangrijkste processen, die in de gefluïdiseerde bed reactor optreden, geïdentificeerd en onafhankelijk van elkaar bestudeerd. Deze processen zijn: de axiale distributie van deeltjes in een gefluïdiseerd bed, de menging in de vloeistoffase, en de precipitatie van calcium fosfaat.

Fosfaatverwijdering in een gefluïdiseerd bed berust op de vorming van een fosfaatlaag op de korrels in het bed. De axiale distributie van korrels in het bed werd om die reden experimenteel vastgesteld en met een theoretisch model beschreven. Volledige segregatie treedt op wanneer het bed bestaat uit uitsluitend kale zandkorrels. Zodra echter een fosfaatlaag gevormd wordt op de zandkorrels vindt menging plaats van de lagen waaruit het bed opgebouwd kan worden gedacht. Dit gedrag kan worden beschreven met een mathematisch model, dat gebaseerd is op een relatie tussen de superficiële vloeistofsnelheid en de porositeit van het bed, op een stabiliteitscriterium voor segregatie volgens welke bedlagen met een hogere beddichtheid segregeren naar lagere axiale posities, en op een vereenvoudigde beschrijving van het precipitatieproces. Simulaties werden uitgevoerd teneinde de werking van het bed te optimaliseren wat betreft het specifiek oppervlak van de

toegevoerde korrels, aangezien dit oppervlak van invloed is op de fosfaatverwijdering, en wat betreft het fosfaatgehalte van de korrels in verband met de commerciële waarde van het produkt. Zowel het specifiek oppervlak van de zandkorrels als het fosfaatgehalte van het produkt nemen toe bij gebruik van fijnkorrelig zand.

De precipitatie van calciumfosfaat geschiedt door menging van twee of meer reactanten op moleculaire schaal. Aangezien precipitatie een snel proces is, vinden menging en precipitatie gelijktijdig plaats, zodat de kinetiek van het mengen van de beide reactanten een belangrijke rol speelt in de uiteindelijke produktkarakteristieken. De invloed van de hydrodynamische omstandigheden op het precipitatieproces van calciumfosfaat werd daarom apart bestudeerd. Een "computational fluid dynamics" methode werd ontwikkeld, gebaseerd op ruimtelijk verdeelde vergelijkingen voor de momenten van de grootteverdeling van de geprecipiteerde deeltjes, op relaties voor de kinetiek van kiemvorming en groei van de precipiterende fase en op de berekening van de heersende vloeistofsnelheden. Deze methode maakt berekening mogelijk van lokale grootheden zoals de lokale oververzadigingen en de lokale momenten van de deeltjesgrootteverdeling. De methode werd toegepast op de precipitatie van calciumfosfaat in een continue double-jet reactor. Door de inlaatpunten voor de voedingsstromen te wijzigen varieerde de omzetting tussen 57 en 83 %, terwijl de gemiddelde deeltjesgrootte veranderde met een factor 1.9 en de spreiding in de deeltjesgrootteverdeling met een factor 1.5. Alleen een kleine fractie van het reactorvolume bleek effectief te worden gebruikt voor de precipitatie.

Vervolgens werd de precipitatie van calciumfosfaat in een gefluidiseerd bed nader bestudeerd. De kinetiek van homogene nucleatie en van de aggregatie van kleine primaire deeltjes werden bij benadering vastgesteld. Aanzienlijke primaire nucleatie, groei en aggregatie van een amorfe modificatie van calciumfosfaat trad op in een kort tijdsbestek van ongeveer 10 seconden in het bodemgedeelte van het gefluidiseerde bed. De primaire deeltjes en de aggregaten, hier aangeduid met de term fines hadden een afmeting van respectievelijk $\sim 0.05 \mu\text{m}$ en $\sim 100 \mu\text{m}$. Een deel van deze fines aggregeerde met de korrels in het bed en droegen als zodanig voor 60% bij aan de totaal verwijderde hoeveelheid fosfaat. De resterende 40% werd afgevangen door het bed via moleculaire groei.

Optimalisering van het fosfaatverwijderingsrendement werd bereikt door stimulering van het aggregatieproces. De aggregatie werd beschreven met een mathematisch model, waarin twee met elkaar concurrerende mechanismen zaten verwerkt (verdisconteerd): orthokinetische aggregatie en breuk. De orthokinetische aggregatie kon worden gestimuleerd door een meer egale dosering van de oververzadiging over de gehele (lengte van de) reactor, en breuk kon worden verminderd door het nastreven van een lage energiedissipatie in het bed. Het optimale fosfaatverwijderingsrendement kon zo worden verhoogd van 50% voor grofe zandkorrels (0.2-0.6 mm diameter) en voor een superficiële snelheid van $1.1 \cdot 10^{-2}$ m/s tot 80% voor fijne zandkorrels (0.1-0.3 mm diameter), een lage superficiële vloeistofsnelheid ($7 \cdot 10^{-3}$ m/s) en door spreiding van de toevoeging van de base over twee voedingspunten, die op twee bedhoogten waren geplaatst.

ACKNOWLEDGEMENTS

This thesis would not have been accomplished without the work and help of many people, whom I would like to thank here. First I would like to mention prof. dr. ir. G.M. van Rosmalen and dr. ing. O.S.L. Bruinsma, for supporting and guiding me at all times and particularly at the most difficult ones, as well as dr. M. Giulietti for the support and valuable advice.

I am grateful to the Foundation for Applied Wastewater Research (STOWA), to the Ministry of Housing, Physical Planning and Environment as well as to the Ministry of Public Transport of the Netherlands for their financial support. I am also grateful to the Institute of Technological Research of the State of São Paulo, Brazil. The following institutions are acknowledged for the fruitful cooperation: DHV Water, Hoechst Holland, Hoogheemraadschap van Rijnland, Hoogheemraadschap van de Uitwaterende Sluizen in Kennemerland en Westfriesland, NOVEM, Riolering en Waterhuishouding Amsterdam, RIZA, and Zuiveringsschap Drenthe.

The supporting personnel of the Laboratory for Process Equipment is acknowledged for their help. In particular I would like to thank Bart Makkus, André van den Bosch and Leo Kuipers for building the experimental set up; ing. Johan Broekens and ing. Carel van Dissel for their support and useful advice; Anton van Zoeren for the help with bibliographic references. Also thanks to ing. Paul Durville for the SEM views; to Edith Uijlen and Mieke Tetteroo for their patience and support.

Relevant contribution was received from ir. M.G. van Aken, ir. L.M.F. Smeets, ir. G.A. Steeman, ir. M. Kuperus, ir. S.J. Nijssen, ir. A. Kismanto and ir. M.L.J. van Leeuwen, ir. E.F.P.M. Koch, M. Staas and F. Flores through their experimental and theoretical work, stimulating discussions, and pleasant company during their graduation period.

CURRICULUM VITAE

Marcelo Martins Seckler was born on July 11th, 1961, in Rio de Janeiro, Brazil. After finishing secondary school in 1979, he began his graduation studies at the Faculty of Chemical Engineering of the University of São Paulo, which was interrupted in 1980 for military service. In 1984 he obtained his degree in Chemical Engineering.

From 1985 to 1986 he worked for a private engineering company in São Paulo, Paulo Abib S.A. Since 1986 he is a researcher at the Technological Research Institute of São Paulo and has been mainly involved in topics related to the fertilizer industry. In 1988 he joined the group of Prof. van Rosmalen in the TU Delft to work on crystallization of calcium sulphate for a period of 3 months, sponsored by the Brazilian government (CNPq). In 1989 he obtained the degree of Master of Sciences in Chemical Engineering at the State University of São Carlos with the thesis "Mathematical modelling of a batch reactor for the production of phosphoric acid". In the same year he obtained a 4 year license from his Brazilian employer to follow his Ph.D. studies in the Faculty of Mechanical Engineering, Laboratory for Process Equipment of the TU Delft. He studied the phosphate removal from wastewater by a precipitation process, in a project sponsored by the Dutch government. This book is the result of this study. Marcelo returns to São Paulo in February, 1994, where he continues to work on crystallization at his former research institute.

Marcelo is married to Thaís Mauad and is going to have a child in April 1994.

